Doctor of Philosophy

The Effect of Interface Layers and Doping on the Multiferroic Properties of Bismuth Titanate Oxide Thin Films on Silicon

David James Coathup

2017

Aston University

The Effect of Interface Layers and Doping on the Multiferroic Properties of Bismuth Titanate Oxide Thin Films on Silicon

David James Coathup

Doctor of Philosophy

31st of March, 2017

Declaration

The work in this thesis is the result of research carried out in the Nanoscience Group at the School of Engineering and Applied Science, Aston University, Birmingham, United Kingdom. I declare it to be my own work unless referenced to the contrary in the text.

Acknowledgements

First and foremost I would like to thank my supervisor, Dr. Haitao Ye, (Reader in Nanotechnology Science) and my associate supervisor Professor David Webb (Professor in Photonics), who's support and guidance have been invaluable through my work. I would also like to extend my thanks to fellow students at Aston University, Vojtěch Kundrát, Shi Su, Jiangling Li and Ruoying Zhang, and also Zheng Li and Xiaojing Zhu of Queens Mary University London who as well as providing guidance, taught me the proper etiquette and attitude needed as an independent researcher.

I would also like to extend my thanks to the collaborator, Dr Haixue Yan (Senior Lecturer, QMUL) for his technical support and guidance through this work. Moreover, I would also like to thank Mr Andrew Abbot(Technical Team Leader), Dr. Thomas Allsop (Senior Research Fellow), Dr. Meiyong Liao (Principal Researcher, NIMS, Japan), Professor John Sullivan (Emeritus Professor) , Dr Sayah Saied (Research Fellow) and Baogui Shi(Research Associate), who again have provided me with a guidance and support throughout this experience.

On a more personal level, I like to thank the many friends who I have met and made throughout this endeavour. I would like to give special thanks to my best friends, Charlie Large and Tien Tang, who have provide me with much joy and strength throughout the many challenges I have faced, and lastly I would like to thank my Parents, Sian and Phillip Coathup, who have been a constant source of support throughout this entire endeavour.

Abstract

For the development of magnetoelectric memory devices, the development of artificial magnetoelectric materials is necessary. Previous work in the field had focused on the multiferroic properties of this material in bulk form, however, for a practical device, a thin film investigation is needed. This thesis details the author's investigation into the multiferroic properties of bismuth titanate oxide, $Bi_4Ti_3O_{12}$, (BTO) thin films doped with lanthanum, niobium, iron and cobalt, to form the novel material $Bi_{3.25}La_{0.75}LTi_{2.5}Nb_{0.25}Fe_{0.125}Co_{0.125}O_{12}$ (BTFC), and how different interface layers influence their structural and electronic properties when they are deposited on silicon substrates. The aim of this research is to achieve a multiferroic BTO thin film with strong ferroelectric and ferromagnetic properties by utilising a novel combination of dopants.

Chapter 1 is the introduction, providing insight into the layout and structure of the thesis making it easier for the reader to follow. Chapter 2 is the background literature review, which discusses the real life industrial demands of this work, and is followed by a discussion of the physics and material science principles behind this investigation. Chapter 3 is the experimental literature review, in which the material synthesis, device fabrication and characterisation techniques utilised in this work are discussed.

The experimental chapters begins with Chapter 4, in which the effect of a zinc oxide (ZnO) interface layer on crystalline properties of BTFC on silicon is investigated. Chapter 5 follows this investigation up by investigating ferroelectric propertied of BTFC thin films on silicon with ZnO interface layers. Finally chapter 6 looks at BTFC thin films on silicon substrates with platinum interface layers, and both simultaneous ferroelectric and ferromagnetic properties were present, confirming multiferroic behaviour.

Initial investigations into the deposition onto silicon were unsuccessful, but were overcome by utilising ZnO interface layers. The ZnO interface layer eliminated some critical difficulties; however high resolution transmission electron microscopy (HRTEM) analysis showed zinc atoms from inside the interface layer diffusing into the BTFC thin film. The investigation into the ferroelectric properties of thin films using the triangular voltage waveform method confirmed ferroelectric domain switching, but were inhibited by the need for a vacuum annealing environment to prevent the oxidation of the silicon substrate. This resulted in the generation of oxygen vacancies within the BTFC thin film, which limited driving voltage during the measurement, presenting ferroelectric saturation.

The final investigation was focused on BTFC deposited on platinised-silicon substrates. Platinum is proved to be the superior interface layer, due to its chemical and thermal stability. The investigation

found high quality crystalline BTFC , with a high dielectric constant and leakage current, which can be attributed to the doping effect. The ferroelectric measurements demonstrated a fully saturated ferroelectric loop, and a remnant polarisation and coercivity of 2Pr = 11.03μC/cm^2, and 2Ec = 196.5kV/cm on the optimised thin films. Ferromagnetic measurements of the sample were challenging, due to the small total magnetisation of the thin film resulting from its low volume and mass. Using a Superconducting Quantum User Interface Device (SQUID) vibrating sample microscopy (VSM), Ferromagnetisum was presented in the bulk and thin film form, however, the remnant magnetisation of the thin film could not be determined, due to its noise level value. This discovery proves the existence of simultaneous ferroelectric and ferromagnetic phases in BTFC thin film, confirming multiferroic behaviour of the deposited thin films had been achieved with the chosen dopants.

Key Words: Bismuth Titanate Oxide, Ferroelectric, Ferromagnetic, RF-Magnetron Sputtering, Triangular Voltage Waveform, SQUID magnetometer.

Relevant publications

- David Coathup, Zheng Li, Xiaojing Zhu, Haitao Ye, The growth of non-c-axis-oriented ferroelectric BLT thin films on silicon using ZnO buffer layer. Material letters, 206, 117-120 (2017)

- David Coathup, Zheng Li, Martin Lee, Haixue Yan and Haitao Ye. The multiferroic behaviours in La, Nb Fe and Co doped Bi4Ti3O12 thin films. (Submitted for publication)

- Meiyong Liao, Jiangwei Liu, Liwen Sang, David Coathup, Jiangling Li, Masataka Imura, Yasuo Koide and Haitao Ye. Impedance analysis of Al2O3/H-terminated diamond metal-oxide-semiconductor structures. Applied Physics Letters 106, 083506 (2015)

- Jing Zhao, Jiangwei Liu, Liwen Sang, Meiyong Liao, David Coathup, Masataka Imura, Baogui Shi1, Changzhi Gu, Yasuo Koide and Haitao Ye. Assembly of a high-dielectric constant thin TiOx layer directly on H-terminated semiconductor diamond. Applied Physics Letters 108, 012105 (2016)

- Hui Xu, Haitao Ye, David Coathup, Ivona Mitrovic, Ayendra and Weerakkody. An insight of p-type to n-type conductivity conversion in oxygen ion-implanted ultrananocrystalline diamond films by impedance spectroscopy. Applied Physics Letters 1110, 033102 (2017)

Contents

Chapter 1 : Introduction 10
Chapter 2 : Literature Review 14
2.1 Introduction 15
2.2 Characteristics of Non-volatile Memory 15
2.2.1 The History, Properties and Future Demands of Non-Volatile Memory. 15
2.3 Ferroelectricity, Ferromagnetism and the Magnetoelectric Effect. 19
2.3.1 Ferroelectricity 19
2.3.2 Ferromagnetism 23
2.3.3 Multiferroics and Magnetoelectrics 27
2.4 Multiferroic Materials 28
2.4.1 Perovskite and Aurivillius Phase Structures 29
2.4.2 The Electrical and Magnetic Properties $Bi_4Ti_3O_{12}$ 31
2.4.3 Site Engineering and Atomics Substitution. 31
2.5 Research Goals and Aims 37
Chapter 3 : The Growth and Characterization of BTFC Thin Films 39
3.1 Introduction 40
3.2 Fabrication Equipment 40
3.2.1 Spark Plasma Sintering 40
3.2.2 Radio Frequency Magnetron Sputtering 43
3.2.3 Thin Film Annealing 47
3.2.4 Thermal Evaporation 51
3.3 Characterisation and Analysis Apparatus 53
3.3.1 X-Ray Powder Diffraction 53
3.3.2 Scanning Electron Microscopy 56
3.3.3 Energy Dispersive Spectroscopy 57
3.3.4 Transmission Electron Microscopy 58
3.3.5 Magnetometer - Super Conducting Quantum User Interface Device 60
3.3.6 X-Ray Photoelectron Spectroscopy 62
3.3.7 Ferroelectric Tester 63
3.4 Summary 66
Chapter 4 : The Integration of BTFC Thin Films on Silicon Substrates Using ZnO Interface Layers 67
4.1 Introduction 68

4.2 Experimental 69
4.3 Results and Discussion 71
4.4 Conclusions 92
Chapter 5 : The Investigation into the Electric and Ferroelectric Properties of BTFC Thin Film Devices 94
5.1 Introduction 95
5.2 Experimental 95
5.3 Results and Discussion 96
5.4 Conclusion 102
Chapter 6 : The Multiferroic Properties of BTFC Thin Films on Platinised Silicon Substrates 103
6.1 Introduction 104
6.2 Experimental 105
6.3 Results and Discussion 105
6.4 Conclusions 120
Chapter 7 : General Discussions for Future Work 121
Chapter 8 : Conclusions 124
References 127

Abbreviations

1T1C = one transistor, one capacitor

BTO= Bismuth Titanate Oxide,($Bi_4Ti_3O_{12}$)

BTFC = Abbreviation of crystalline material ($Bi_{3.25}La_{0.75}Ti_{2.5}Nb_{0.125}Fe_{0.125}Co_{0.125})0_{12}$

DC = Direct Current

DRAM = Dynamic Random Access Memory

E = Electric Field

E_b = Electron Binding Energy

EPROM = Erasable Programmable Read-Only Memory

EEPROM = Electrically Erasable Programmable Read-Only Memory

E_{kin} = kinetic energy of emitted electrons

FeRAM = Ferroelectric Random Access Memory

H_C = Magnetic Coercive Field

HP = Hot Press (Sintering)

HRTEM = High Resolution Transmission Electron Microscopy

H_V = energy of the incident X-Ray

M = Magnetisation

MC = magentocapaitance

MFS = Metal Ferroelectric Semiconductor

M_S = Magnetic saturation.

ME = Magnetoelectric

MEMs = Micro Electro Mechanical Systems

MeRAM = Magnetoelectric random access memory

MRAM = Magneto resistive random-access memory

MvH = Magnetisation Vs Magnetic Field

NEMs = Nano Electro Mechanical Systems

P-Si = P-type silicon

PVD = Physical Vapour deposition

RAM = Random Access Memory

RMS = Root Mean Squared

ROM = Read Only Memories

RF = Radio Frequency

SAED = Select Area electron Diffraction

SEM = Scanning Electron Microscopy

SPS = Spark Plasma Sintering

SRAM = Static Random Access Memory

SQUID = Super Conducting Quantum User Interface Device

SSD = Solid state Disk

SRAM = Static Random Access Memory

VSM = Vibrating Sample Magnetometer

WC = Tungsten Carbide

W_F = the work function of the spectrometer

XPS = X-ray Photo spectroscopy

XRD = X-Ray diffraction

ZnO = Zinc Oxide

List of Symbols

D = Electrical displacement

ε = Strain

ε_r = relative permittivity

Emu = Electromagnetic Units

E = Electric Field

E_C = Coercive field (Ferroelectric)

H = Magnetic Field

H_c = Coercive Field (Ferromagnetic)

I = Current

M = Magnetisation

MHz = Mega-Hertz

M_s = Magnetic saturisation

M_r = Remnant magnetisation

P = Polarisation

P_{down} = Downwards polarisation

P_r = Remnant Polarisation

P_s = Spontaneous polarisation

P_{up} = Upwards polarisation

T = Tesla

V = Voltage

List of Figures

Figure 2-1 A plot of how the transistor density and minimum feature size have followed Moore's Law between 1971 and 2011. Triangles, Squares and Diamonds indicate transistor size for leading manufacturers, and circles indicate minimum feature size(10). 16
Figure 2-2 A demonstration of how digital device miniaturisation (More Moore) and device diversification (Moore than Moore) combine together to make higher value systems(11). 17
Figure 2-3 The MRAM cell structure. Two Ferromagnetic layers are separated by a thin tunnelling barrier. One ferromagnetic layer is fixed by a pinning layer, whilst another is free to switch orientation when an external magnetic field is applied(17) 18
Figure 2-4 Polarisation vs Electric field hysteresis loop of a ferroelectric material(25). 20
Figure 2-5 Ferroelectric switching in Perovskite structures(27). 21
Figure 2-6 Ferroelectric phase transition temperature between ferroelectric tetragonal phase and non-ferroelectric Para electric cubic phase(28) 22
Figure 2-7 The magnetic moment generated by an electron, (a) orbital path of an electron around a nucleus, (b) rotation of electron on its own axis(32). 23
Figure 2-8 Atomic magnetic dipole moments of diamagnetic and paramagnetic materials with and without applied magnetic field (H). (a)(left) A diamagnetic material without the presence of a magnetic field, no dipoles are present (right)A diamagnetic material in the presence of a magnetic field, the dipoles oppose the external magnetic field. (b)(left) Paramagnetic material without an external magnetic field. The magnetic dipoles are randomly orientated, resulting in no magnetisation, (b)(right)paramagnetic material, magnetic dipoles align with an external magnetic field, producing a net magnetisation. 24
Figure 2-9 Magnetic domains in a ferromagnetic material. When B = 0, domains are equivalent size resulting in no flux. With the application of a magnetic field, domains aligned with the field grow whilst those opposed shrink, leading to polarisation across the material(34). 25
Figure 2-10 The process of ferromagnetic hysteresis, (domain walls changing to match an external magnetic field(35). 26
Figure 2-11 Examples of multiferroic coupling in the ferroelectric, ferromagnetic and ferroelastic orders. Applied electric fields (E), results in changes to the magnetisation (M) and strain(ε). Applied magnetic fields (H) results in changes to the electric polarisation(P) and strain(ε), and applied stress(σ) results in changes to the electric polarisation(P) and magnetisation(M)(37). 27
Figure 2-12 The structure of Perovskite mineral, SrTiO3. Here the formula, ABX3 is A = Sr, B=Ti and O = 3 (45). 29
Figure 2-13 Aurivillius phase structure of (Bi_2O_2)-$Bi(Ti,Nb)_2O_7$ (45). 30
Figure 2-14 Polarisation – electric Field (P-E) loops for BLT thin films, with the initial P-E loop in closed circles, and P-E loops after $3x10^{10}$ read/write cycles in open circles(48). 32
Figure 2-15 X-ray diffraction pattern of Bi3.25La0.75Ti3-xNbxO12 for X= 0.0, 0.04, 0.05 and x = 0.1(61). 33
Figure 2-16 the effect of niobium doping on the electronic properties of Bi3.25La0.75Ti3-xNbxO12, (left) remnant polarisation (2Pr) and coercive field (Ec), (right) leakage current(61). 33
Figure 2-17 The M-H curve of Bi5FeTi3O15 (BFTO) and $Bi_5Fe_{0.5}Co_{0.5}Ti_3O_{15}$ (68) 34
Figure 2-18 Ferroelectric loop PvE (left) Ferromagnetic Loop MvH (middle) magnetocapacitance effect fvε (right) Cole-cole plot (right, insert) for $(Bi_{3.15}Nb_{0.85})(Ti_2Fe_{0.5}Co_{0.5})O_{12}$ (4). 35

Figure 2-19 (left) Co-parallel spin structure, (right) Canted spin structure. 36
Figure 3-1 Diagram of covnentional hot pressing sintering(82) 41
Figure 3-2 SPS, The current flow of a pulsed DC signal through grains in SPS. Thermal energy is concentrated at the grain boundaries between particles(84). 42
Figure 3-3 Diagram of DC sputtering. Ionised plasma (Ar+) is accelerated towards the cathode target by an electric field. Bombardment of target by argon atoms results in the ejection of target atoms, which land on the substrate(85). 43
Figure 3-4 Schematic of rf magnetron sputtering. The radio frequency electric field accelerates charged electrons towards the target whilst in one voltage direction, and discharges the target during the opposing alignment. The magnetic field generated by the magnetron contain electrons near the target, increasing plasma generation rate(86). 44
Figure 3-5 Front view of Aston Universities sputtering chamber, key parts have been labelled. 46
Figure 3-6 X-ray diffraction patterns of $Bi_4Ti_3O_{12}$ thin films deposited on Si(100) silicon substrates after annealing at various temperature using rf magnetron sputtering (58). 48
Figure 3-7 Astons Carbolite, CWF 11/23, Furnace. 49
Figure 3-8 Aston Universities' Siomm SGL-1700 Vacuum furnace. 50
Figure 3-9 A picture of the outside of Aston University's Moorfield thermal evaporator 51
Figure 3-10 A picture of the inside the bell jar of Aston University's Moorfield thermal evaporator 52
Figure 3-11 Braggs Law, X-rays of wavelength λ, experience maximum constructive interference when the condition, $n\lambda=2d\sin\theta$, is met, where d is the separation of crystal planes and θ is the angle of incident(92). 54
Figure 3-12 Schematic of the SEM apparatus(94). 56
Figure 3-13 The process of electron emission in EDS for a silicon atom. The incident electron removes an electron from the inner K ring, resulting in the emission of the two electrons and the generation of an electron hole. An electron in the L orbital drops then into the electron hole, emitting x-ray radiation characteristic of silicon in the process(97). 58
Figure 3-14 (A) schematic of TEM apparatus, (B) diagram of electrons diffracted by specimen being focused onto imaging plane (101). 59
Figure 3-15 diagram of SQUID magnetometer. The sample is oscillated within magnetic field H, which induces a change in the magnetic flux inside the chamber depending on the samples magnetic moment. This in turn leads to a change in current of the through the superconducting wires(102). 61
Figure 3-16 The process of electron emission in XPS (107). 62
Figure 3-17 Schematic of the ferroelectric testing apparatus 64
Figure 3-18 A picture of the apparatus used in the ferroelectric measurements performed in this investigation 65
Figure 3-19 The ferroelectric analysis of NKN performed measured at 1Hz and 25°C, Electric Field and Current Vs Time, Current Vs Electric field for a single voltage cycle, Electrical Displacement Vs Electrical Field Loop (108) 65
Figure 4-1 XRD pattern 100nm of BTFC thin films deposited directly onto P-Si (111) and annealed post deposition at 650°C in ambient atmosphere. 72
Figure 4-2 XRD patterns of 300nm BTFC thin films on annealed ZnO interface layers, (A) Annealed ZnO interface layer on P-Si(111), (B) BTFC thin film on ZnO interface layer without annealing, (C) BTFC annealed at 550°C, (D) BTFC annealed at 650°C, (E) BTFC annealed at 700°C, (F) BTFC annealed at 750°C. Pyrochlore phase peaks labelled 'P'. ZnO peaks labelled 'ZnO' 73

Figure 4-3 XRD patterns of 300nm BFCT thin films on as deposited ZnO interface layers, (A) As-deposited ZnO interface layer on Si(111), (B) BTFC thin film on ZnO interface layers without annealing; (C) BTFC annealed at 550°C, (D) BTFC annealed at 650°C, (E) BTFC annealed at 700°C, (F) BTFC annealed at 750°C. Pyrochlore phase peak labelled 'P'. ZnO peak is labelled 'ZnO'. 74
Figure 4-4 The grain size of BTFC annealed at different temperatures on P-Si(111) with annealed ZnO (black) and As-deposited ZnO (red) interface layers, as calculated by the Scherer equation..... 76
Figure 4-5 SEM images of 100nm BTFC deposited directly onto P-Si (111) substrates and annealed at 650°C for 1 hour in ambient atmosphere..... 78
Figure 4-6 SEM images of BTFC thin films on p-Si(111) with annealed ZnO interface layers, A) The annealed ZnO interface layer, B) As-deposited BTFC, C) BTFC annealed at 550°C, D) BTFC annealed at 650°C, E) BTFC annealed at 700°C, F) BTFC annealed at 750°C. 79
Figure 4-7 SEM images of BTFC thin films on P- Si(111) with annealed ZnO interface layers, (A) ZnO interface layers, (B) As-deposited BTFC (C), BTFC annealed at 550°C, (D) BTFC annealed at 650°C, (E) BTFC annealed at 700°C, (F) BTFC annealed at 750°C..... 80
Figure 4-8 Cross-sectional TEM of 300nm BTFC on 50nm ZnO interface layers..... 82
Figure 4-9. HRTEM image of 300nm BTFC on 50nm ZnO interface on P-Si(111) substrates..... 83
Figure 4-10 HRTEM image of ZnO/BTFC interface layer- Left ZnO interface layer, right BTFC thin film. 84
Figure 4-11 Selected Area Electron Diffraction of BTFC thin films. 85
Figure 4-12 Elemental mapping of 300nm BTFC on P-Si (111) using a ZnO interface layer. (A) Image of the sample for dimension reference, (B) Bismuth elemental mapping, (C) Oxygen elemental mapping, (D) Titanium elemental mapping, (E) Zinc elemental mapping, (F) Silicon elemental mapping. 86
Figure 4-13.Wide spectrum XPS for BTFC thin films annealed at 700°C on P- Si (111) with As-deposited ZnO interface layers. 88
Figure 4-14 High-resolution XPS core-level spectra of Sample 14: (A) Bi4f, (B) La3d, (C) Ti2p, (D) Ni3d, (E) Fe2P, (F) Co2p, (G)O1s. 89
Figure 4-15. EDS spectrum for BTFC thin films annealed at 700°C on P- Si(111) with as-deposited ZnO interface layers. 91
Figure 5.5-1 Device configuration of BTFC thin films on P-Si using ZnO interface layers. 50nm ZnO is deposited directly onto P-Si, followed by 600nm BTFC. After sample annealing in vacuum atmosphere, Ti contacts are deposited onto the silicon and BTFC to form electronic contacts, followed by a tungsten carbide (WC) protection layers. 96
Figure 5-2 XRD pattern of device 1, which consists of 600nm BTFC thin films on P-Si substrates with 50nm ZnO interface layers. Samples annealed in vacuum for 1 hour at 700°C. 97
Figure 5-3 Current density (J) – Electric Field (E) for BTFC thin films on silicon with ZnO interfaces layers. 98
Figure 5-4 Capacitance (C) – Electric Field (E) plot for the BTFC thin films on p-type silicon with ZnO interfaces layers. 99
Figure 5-5 Ferroelectric characterisation of BTFC thin films measured at 172kV/cm, 20Hz. (A) Electric field (black) and current (red) versus time (E-t, I-t), (B) Current verses electric field (I-E) hysteresis loop, (C) Electric displacement vs electric field (D-E) hysteresis loop. 100
Figure 5-6 Ferroelectric characterisation of BTFC thin films measured at 362kV/cm, 20Hz. (A) (Electric field (black) and current (red) versus time (E-t and I-t), (B) Current verses electric field (I-E) hysteresis loop, (C) Electric displacement vs electric field (D-E) hysteresis loop. 101

Figure 6-1 XRD of BTFC thin films deposited on platinum and annealed at different temperatures. Thin films annealed at (A) 550°C, (B) 600°C, (C) 650°C, (D) 700°C, (E) 750°C. 106
Figure 6-2 The crystallite size of the (117) plane for BTFC thin films deposited on platinised substrates and annealed at different temperatures. 107
Figure 6-3 Cross sectional area of BTFC thin films deposited for (A) 240 minutes, (B) 196 minutes, (C) 120 minutes, (D) 60 minutes. All samples annealed for 1 hour in ambient atmosphere at 650°C.... 109
Figure 6-4 Plot of deposition time (minutes) vs Thin Film thickness (nm) for BTFC on Pt/Si Substrates 110
Figure 6-5 X-ray diffraction pattern of BTFC deposited for (A) 60 minutes, (B), 120 Minutes, (C) 196 Minutes and (D) 240 minutes. 111
Figure 6-6 Leakage Current behaviour of BTFC thin films on platinised silicon. 112
Figure 6-7 Capacitance – Voltage behaviour of BTFC thin films on platinised silicon. 113
Figure 6-8 Ferroelectric characterisation of BTFC thin films measured at 35Vpeak to peak, 100Hz. (A) (E-t) Electric field versus time (black) and current versus time (red) versus time (C)(I-E) current verses electric field hysteresis loop, (C) (D-E) electric displacement vs electric field hysteresis loop. 114
Figure 6-9 The magnetisation (M) versus magnetic field (H) response for the bulk BTFC target. 116
Figure 6-10 The magnetisation (M) versus magnetic field (H) response for the bulk BTFC target, zoomed in between H = -4K and 4KOe. 116
Figure 6-11 The magnetisation (M) versus magnetic field (H) response for the platinised silicon substrate. 117
Figure 6-12 The magnetisation (M) versus magnetic field (H) response for the BTFC coated platinised silicon (Red circles) and the BTFC coated platinised silicon with the substrate subtracted (black squares)..... 118
Figure 6-13 The magnetisation (M) versus magnetic field (H) response for the BTFC coated platinised silicon with the substrate subtracted , zoomed in between -4K and +4KOe. 119

Chapter 1 : Introduction

This thesis provides insight into the integration of doped bismuth titanate oxide thin films on silicon substrates with zinc oxide interface layers for affordable memory devices. It also provides insight to how Fe and Co doping induce ferromagnetism into bismuth titanate oxide thin films, contributing to the field of magnetoelectric memory devices.

The first floating gate memory device dates back to Bell Laboratories in 1976. Since then, memory devices have formed a ubiquitous part of the electronic devices that are playing an increasingly larger part of people's lives. The development of more compact and higher powered devices has been fuelled by the demand for higher quality devices at lower costs. One such route for higher quality devices is by further minimisation. Miniaturisation is the reduction in feature size, that comes with the further development of material and fabrication processes, and allows for more powerful devices, by increasing the density of computing elements. The limitations of miniaturisation are however being approached, with a leading memory device manufacture, Reports have claimed to be achieving feature sizes down to just 15nm(1). Below this size new design limitations begin to occur, such as the minimal current channel width, and the limited amount of charge that can be stored on the gate electrode.

Due to the limitations of minimisation, other methods of adding device value to keep up with future market demands are being investigated, these include the adding of value through device diversification, increased functionality and new memory types. An emerging memory type with increased functionality is the magnetoelectric memory device, in which the functionalities of ferroelectric and ferromagnetic memory are combined, resulting in a device that possess the advantages of both, whilst possessing the key disadvantages of neither.

The development of magnetoelectric devices, however, is limited by the lack of single-phase, room temperature multiferroic materials. Currently, investigations are focused on both heterolayers magnetoelectric devices (2) and single phase magnetoelectric materials. Heterojunctions have been reported to possess higher levels of magnetoelectric coupling than single phase materials, however, demand still exists for single phase materials. This is due to the coupling of heterojunctions being limited by interface mediated coupling between the ferroelectric and ferromagnetic layer. This limits the complete switching of the ferroelectric polarisation by a magnetic field, and the complete switching of the magnetisation by an electric field(3). Additionally, single phases are desirable for the high throughput and simplicity.

Recent research has shown that bismuth titanate oxide (BTO) doped with Fe and Co in the bulk form possess strong ferromagnetic properties, and simultaneous coupling between the ferroelectric and

ferromagnetic states, indicating magnetoelectric behaviour(4). This thesis aims to build upon the investigation of BTO doped with Fe and Co, by investigating this material in the thin film form. As well as BTO doped with iron and cobalt, this thesis looks at the effect of lanthanum and niobium doping as well, in order to improve the fatigue, leakage and dielectric properties. This forms a thin film with a unique combination of dopants, to form $Bi_{3.25}La_{0.75}Ti_{2.5}La_{0.25}Fe_{0.0125}Co_{0.125}O_{12}$, referred to as BTFC throughout this thesis.

When investigating materials in the thin film form, the substrate has a significant effect on the crystallinity and electrical properties of the deposited film. It is desirable that BTFC thin films are deposited onto silicon substrates for integration with existing devices, however this is limited by the diffusion of atoms between the two layers, which is a common occurrence when oxide layers are deposited onto silicon. To compensate for this, interface layers can be inserted between substrate and ferroelectric layer, to prevent atom diffusion, and to improve the crystallinity. Both platinum and ZnO interfaces were investigated, with the integration of ZnO with bismuth layered ferroelectrics being a largely undocumented field, requiring further investigation(5).

The main body of this thesis is broken into five chapters, the first of these is Chapter 2, which introduces the literature background of this thesis. This chapter starts with an introduction to the field of memory devices. The chapter discusses the history and current state of the memory market, as well the upcoming challenges, and how these difficulties can be overcome by the emerging field of magnetoelectric memory. This is followed by a discussion into the phenomena of ferroelectricity, ferromagnetism, and magnetoelectricity. The background physics is discussed, and is used to explain how they are utilized in functional memory devices. Finally, the field of bismuth layered ceramics and the properties of BTO are introduced. An explanation of how ferroelectricity and ferromagnetism occur in these materials on an atomic level is provided, and how the properties can be tailored using dopants.

Chapter 3 discusses the experimental techniques used in this work. This chapter starts by explaining the fabrication procedures used through this investigation, which includes spark plasma sintering (SPS), radio frequency (RF) magnetron sputtering, furnace annealing and thermal evaporation. These fabrication techniques are explained in such that the reader should fully understand the details of the process, and understand how they are utilised in device and thin film fabrication throughout this investigation. The second half of this chapter discusses the characterisation techniques involved in the same way, the discussion includes X-ray Diffraction (XRD), Scanning electron Microscopy (SEM), Energy-dispersive X-ray spectroscopy (EDS), Transmission electron Microscopy (TEM), X-Ray Photo spectroscopy (XPS), the triangular voltage waveform method and (Superconducting Quantum User

Interface Devices) SQUID magnetometers. After reading, the reader should fully comprehend how these techniques work, and how they are utilised in providing relevant information about the sample.

Chapter 4 is the first experimental chapter, and demonstrates the investigation of BTFC deposition on silicon, with and without a ZnO interface layer. The goal of this investigation is to determine if the crystallinity of the BTFC thin films can be improved on silicon substrates by using a ZnO-interface layer. The effect of the ZnO interface layers pre-treatment on the crystallinity of BTFC thin films is also investigated. This is followed by an investigation into the chemical stability of the interfaces by elemental mapping, followed a chemical analysis of the BTFC thin film by XPS and EDS, to determine if all doping elements have successfully been inserted into the crystal structure.

Chapter 5 builds upon the findings of chapter 4 by investigating the electronic properties of BTFC on silicon with ZnO interface layers. The capacitance and resistivity of the thin films are examined by semiconductor analyser, and the ferroelectric properties are examined using the triangular waveform voltage method.

Chapter 6 aims to improve upon the work of chapters 4 and 5, by investigating the ferroelectric and ferromagnetic properties of BTFC thin film integrated on silicon substrates with platinum coating. Firstly, the effect of deposition time and post deposition annealing temperature are investigated to optimise the thin film quality. Next, the ferroelectric, leakage and dielectric properties of the optimal thin film are investigated. Lastly, this chapter investigates the ferromagnetic properties of BTFC, using a SQUID magnetometer, and discusses in detail the challenges faced in the emerging field of magnetic thin film characterisation.

Finally, the last two chapters, chapters 7 and 8, are the conclusion and the discussion for future work, where the findings are summarised, and the next steps in the investigations are established.

Chapter 2 : Literature Review

2.1 Introduction

This literature review chapter has two aims. The first is to establish the demands of the computer memory market that justify the need for this investigation and, the second is to explain the electronic and material principles that form the core of this investigation. This chapter is broken into several subchapters that discuss these subjects in a logical flow. The first subchapter details the aforementioned demands of the memory market, the challenges it faces as miniaturisation reaches its limits are discussed, followed by an introduction to our solution to this challenge in the form of magnetoelectric memory devices.

The second subchapter explains in detail the physics phenomena of magnetoelectric coupling. It starts by first introducing the physics of magnetoelectricity and the underlying ferroelectric and ferromagnetic principles. The chapter ends by discussing how the unique properties of magnetoelectric materials are utilised in a functional memory device and how they meet the previously stated demands of the memory market.

The third subchapter introduces our candidate material for magnetoelectric coupling, $Bi_4Ti_3O_{12}$ (BTO). The chapter discusses from an atomic and material's perspective how magnetoelectric coupling can be induced by the insertion of iron and cobalt dopants, as well as how other desirable properties can be optimised lanthanum and niobium doping. The chapter ends by discussing the challenges of BTO thin film integration onto silicon substrates, and the solution zin oxide (ZnO) interface layers is introduced.

Lastly, a short subchapter will summarise the exact aims of this work, so that the reader understands its goals and novelty.

2.2 Characteristics of Non-volatile Memory

2.2.1 History, Properties and Future Demands of Non-Volatile Memory.

The first floating gate used to obtain a non-volatile memory device was proposed in 1976 by Dr. Kahng of Bell laboratories(6). This proposed sample, however, would suffer from low charge storage due to zirconium being used as the floating gate and the side wall portions of the floating gate being exposed to air(7). Later, in 1984, Dr. Masuoka of Toshiba Japan(8) proposed the first flash EEPROM (Electrically Erasable Programmable Read-Only Memory) which became a component of solid-state disks (SSDs), which since then have become a dominant part of modern electronics.

Today, the modern memory market is constantly being pushed to build upon these origins to produce more powerful, compact and cheaper memory devices. The market has replied to this demand by increasing device miniaturisation, following the trend known as Moores Law for the last 50 years. Gordon Moore, in his famous 1960's paper (9), predicted that the average transistor density on a chip would double every eighteen months using just empirical data from over the past six years. Figure 2.1 demonstrates how over the last 40 years, the transistor density has doubled almost every one and a half to two years, whilst the minimum feature size has also steadily decreased.

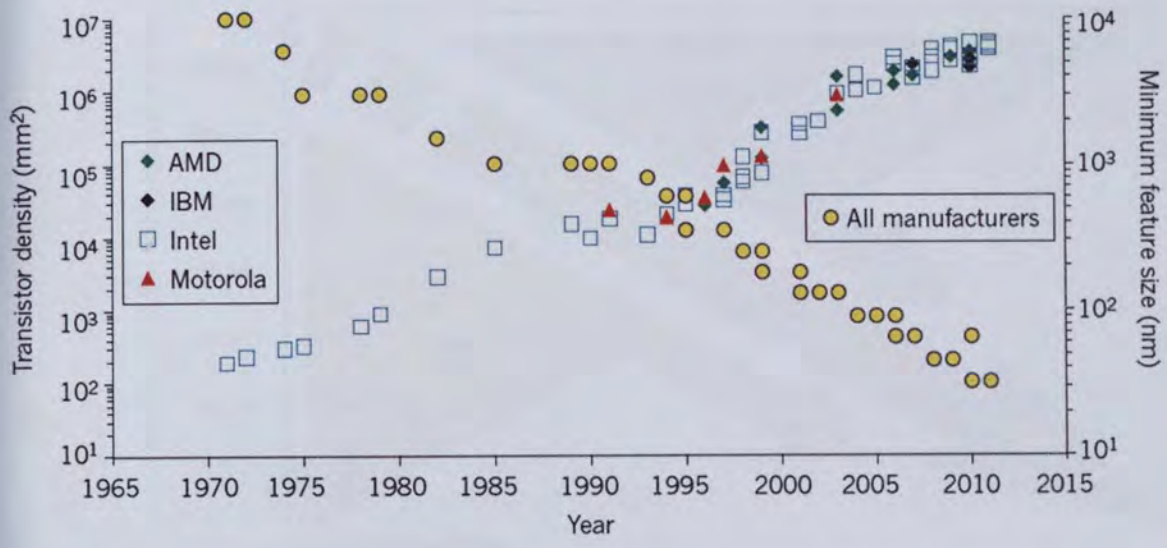

Figure 2-1 A plot of how the transistor density and minimum feature size have followed Moore's Law between 1971 and 2011. Triangles, Squares and Diamonds indicate transistor size for leading manufacturers, and circles indicate minimum feature size(10).

The phenomena of Moore's Law can be attributed to a virtuous cycle: by improvements in transistor miniaturisation, improved cost-to-performance ratios in memory and semiconductor devices are achieved, which assist in growing the semiconductor market. This in turn results in more investment, leading to the development of further miniaturisation(11).

The improvement of electronic devices by further miniaturisation is known as "More Moore". Whilst the improvement of devices by "More Moore" is practical for memory devices and microprocessors, it has its limitations with devices that interface with the physical real world(12). Many semiconductor and memory devices require direct integration with analogue systems that interact with the surrounding environment and real world, including transducers such as radio frequency devices and actuators, including MEMs and Transmitters. The diversifying of memory and semiconductor devices in a way to incorporate these systems is known as "More than Moore". By incorporating both "More Moore" device miniaturisation and "More than Moore" device diversification, greater device value

can be achieved. The process of increasing device value by incorporating "More Moore" and "More than Moore" is presented in figure 2.2.

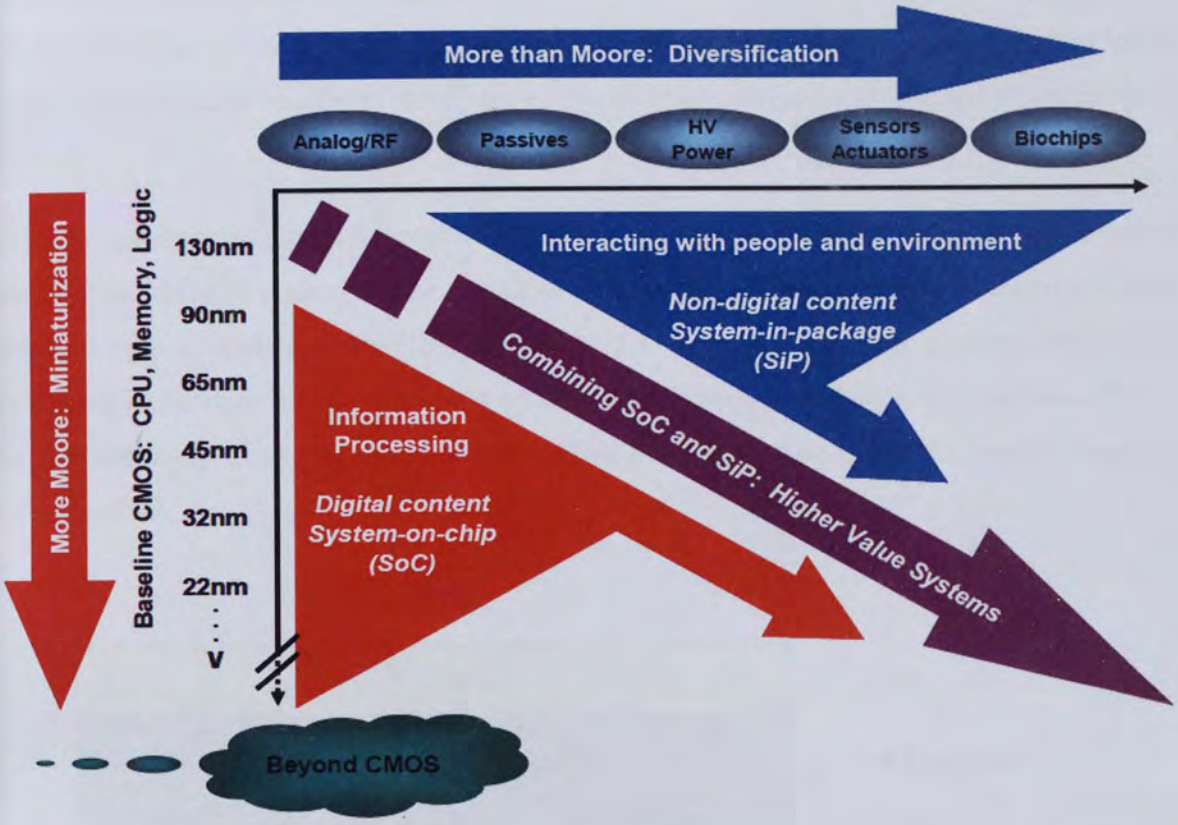

Figure 2-2 A demonstration of how digital device miniaturisation (More Moore) and device diversification (Moore than Moore) combine together to make higher value systems(11).

A key challenge faced by the memory device industry is developing high-speed, embedded, volatile and non-volatile memory technologies that can replace SRAM (Static Random Access memory) and Flash type memory devices. Both of these memory types hold large portions of the memory market, however, they are expected to reach scaling limitations within the next few years as we approach the practical size limitations for transistor and MOS structures, driving the need for new memory technologies to replace them(13).

One type of memory device proposed for replacing SRAM and Flash is the emerging magnetoelectric memory device(MeRAM)(14). The magnetoelectric memory device is based on the concept of combining the functionality of ferroelectric memory devices, and ferromagnetic memory devices, producing a device that possesses the advantages of both, and the key disadvantages of neither.

One of the type of memory device forming the basis of magnetoelectric memory is the Ferroelectric Random Access Memory (FeRAM) device(15). The FeRAM device uses an electric field to control the remnant polarisation state of a ferroelectric material, forming the basis of the memory effect. FeRAM is renowned for its frequent applications in mobile applications due to its small cell size, fast read/write speed, low power/voltage demand, and small cell size. The key disadvantage of FeRAM is that when the state of the device is read, some of the stored charge is lost. This can result in loss and corruption of data after multiple read cycles, or the constant refreshing of the device, limiting power efficiency.

The other key memory type is Magnetic Random Access Memory (MRAM). In an MRAM device, the state is determined by measuring the resistance of a junction made of two ferromagnetic materials separated by a tunnelling barrier(16), as presented in figure 2.3(17). The resistance through the junctions is dependent on the alignment of the two ferromagnetic layers, and by alternating the magnetic alignment of one layer with an external magnetic field, the state of the memory device can be changed(18).

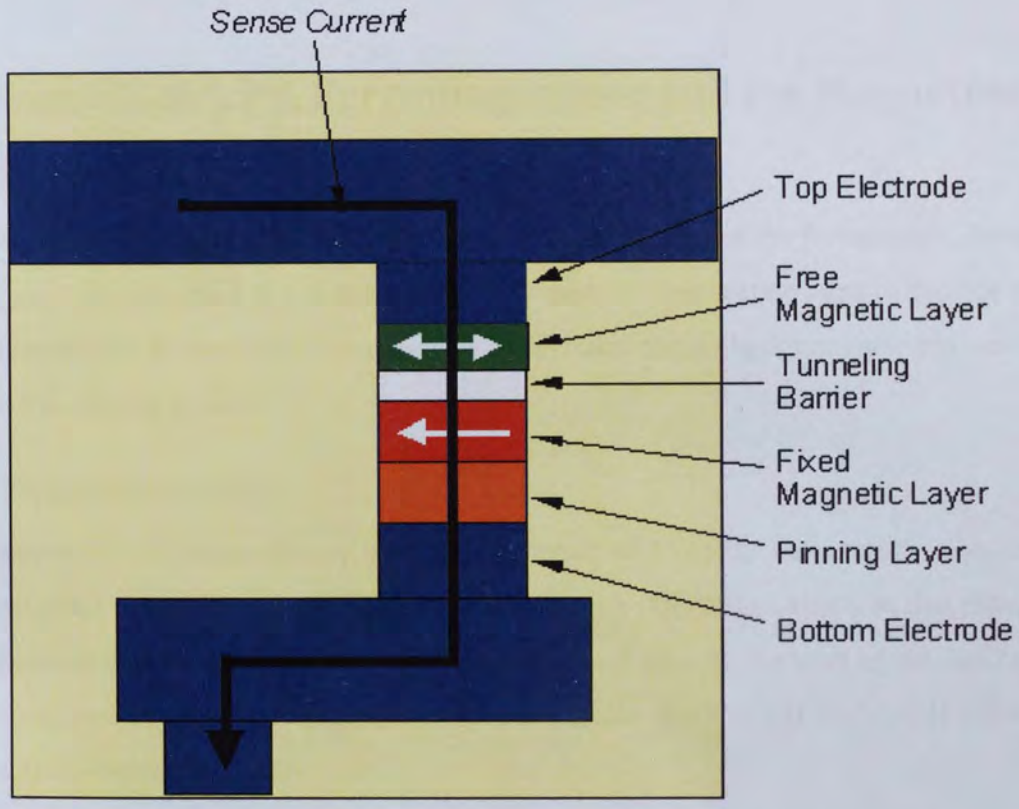

Figure 2-3 The MRAM cell structure. Two Ferromagnetic layers are separated by a thin tunnelling barrier. One ferromagnetic layer is fixed by a pinning layer, whilst another is free to switch orientation when an external magnetic field is applied(17).

Unlike FeRAM, the MRAM device can be read multiple times, without data loss. However, the key disadvantage of MRAM lies in the high current needed to produce the magnetic field required to switch the magnetic state of the device. The high current demand reduces the power efficiency of the device and lengthens the writing cycle of the device.

FeRAM and MRAM have their advantages and disadvantages. However, by combining elements of both memory types to form a magnetoelectric deceive, it is possible to produce a memory device that possesses the strengths of both, and the neither of the key disadvantages. This emerging type of memory device is the Magnetoelectric Random Access Memory (MeRAM) Device (14). The MeRAM device utilises materials with the magnetoelectric effect. In a magnetoelectric material, a change in the ferroelectric polarisation results in a change in ferromagnetic magnetisation and vice versa. This allows for a memory device in which the ferroelectric state is controlled with a magnetic field, and the magnetic state is controlled by an electric field (19, 20). This opens the possibility of a memory device in which the state is written fast and energy efficiently in the ferroelectric domain, but read non-destructively in the magnetic domain (21, 22), utilising features of both FeRAM and MRAM.

2.3 Ferroelectricity, Ferromagnetism and the Magnetoelectric Effect.

The previous section introduced the importance and applications of the ferroelectric, ferromagnetic and magnetoelectric effect in the field of memory devices. This section aims to provide the reader with the necessary background information to understand these physics phenomena, and how they relate to the upcoming work.

2.3.1 Ferroelectricity

The phenomena of ferroelectricity was first reported in 1920 by Valasek(23), who observed a hysteresis effect in sodium potassium tartrate tetra hydrate ($KNaC_4H_4O_6.4H_2O$). At that time, however, it was dismissed as just an artefact. It was not until much later at the start of the 1950's, with the discovery of the ferroelectric phenomena in Barium titanate ($BaTiO_3$) and KH_2PO_4(24) that the field of ferroelectricity emerged.

Ferroelectric materials are characterised by their unique non-zero spontaneous polarisation. What this entails, is that by applying an electric field, the material will become polarised like a dielectric. However, upon removal of the electric field, some polarisation will remain. This polarisation however can still be removed, or even reversed by applying an electric field in the opposing direction. The

Polarisation(P) Vs Electric Field(E) hysteresis loop for a typical ferroelectric sample can be seen in figure 2.4.

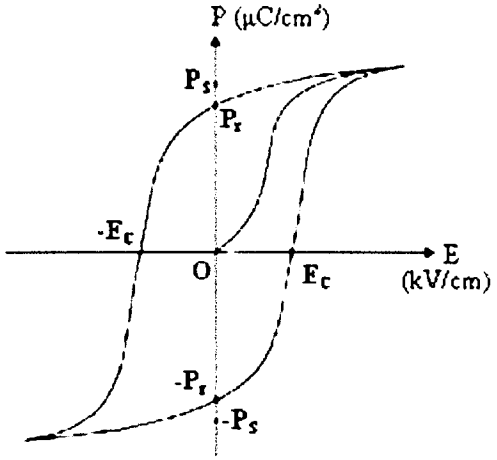

Figure 2-4 Polarisation vs Electric field hysteresis loop of a ferroelectric material(25).

When an electric field is applied to the ferroelectric material from an initial zero polarisation, the polarisation increases as dielectric and ferroelectric dipoles in the material orientate themselves to face the applied field. As the electric field is reduced, the measured polarisation drops as the dielectric dipoles lose their orientation. However, when the electric field reaches zero, a non-zero polarisation remains due to the ferroelectric dipoles remaining aligned in the direction of the previously applied field. This results in the non-zero spontaneous remnant polarisation, P_r. By further applying an electric field in the opposite direction, some polarisation is lost as ferroelectric dipoles orientate themselves to face the opposing field. The electric field required to produce a zero polarisation is called the coercive field (Ec). By applying a further negative electric field, a negative saturation polarisation can be achieved, and again if the negative electric field is removed, a negative, non-zero polarisation remains.

The remnant polarisation forms the basis of the ferroelectric memory effect. A ferroelectric memory device can be obtained from a single ferroelectric capacitor, which is capable of storing one bit of data, depending on the polarisation state. The stored data can be read by applying an electric field greater than the coercive field. If the switching voltage is in the same direction as the polarisation state, then no change in capacitor charge occurs. If the switching field is in the opposite direction, then the polarisation is forced to zero and the capacitor current discharge is detected, which determines the state of the device*(26)*. It is desirable that for high-quality devices that the coercive field is as small as possible, allowing for more energy efficient and faster read/write cycle, whilst the remnant polarisation is as large as possible for easily sensed discharges.

The phenomena of Ferroelectricity can be attributed to the dipoles in the ferroelectric material possessing an overlocking central position. Figure 2.5 demonstrates the ferroelectric phenomena in the Perovskite crystal structure(27). The formula for a Perovskite is ABO_3, with A being a cation with valance 1+ to 3+ and B is a cation with valance +3 to +6(28). The crystal structure itself is tetragonal, meaning two lengths are equal, but the third length is different. This results in the central 'B' cation having no cento-symmetric position, indicating that it must exist as one of two states, upwards or downwards. This resulting in spontaneous polarisation P_{up} and P_{down} within the cell respectively. As it requires a minimum degree energy to switch between the P_{up} and P_{down} states, the cation will remain in its current state unless a sufficiently strong electrical field is applied in the opposite direction.

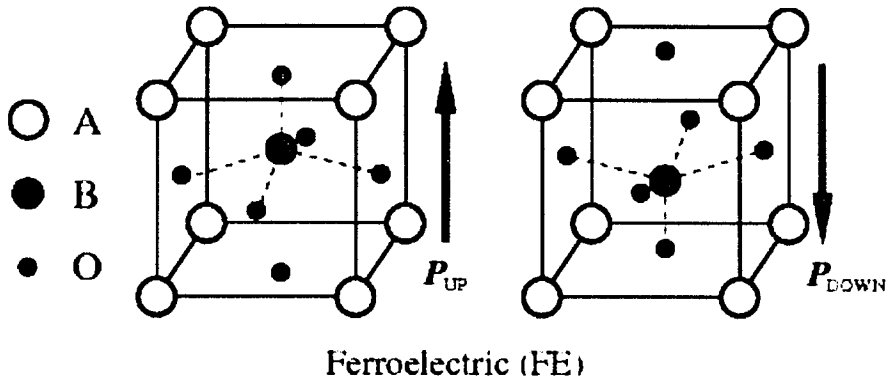

Figure 2-5 Ferroelectric switching in Perovskite structures(27).

The ferroelectric response of a material is temperature dependent, with a transition point known as the ferroelectric-Curie temperature(29). The ferroelectric-Curie temperature exists due to phase transitions between Low temperature ferroelectric non-centrosymmetric phases, and the high temperature non-ferroelectric centrosymmetric phases, as seen in figure 2.6(28).

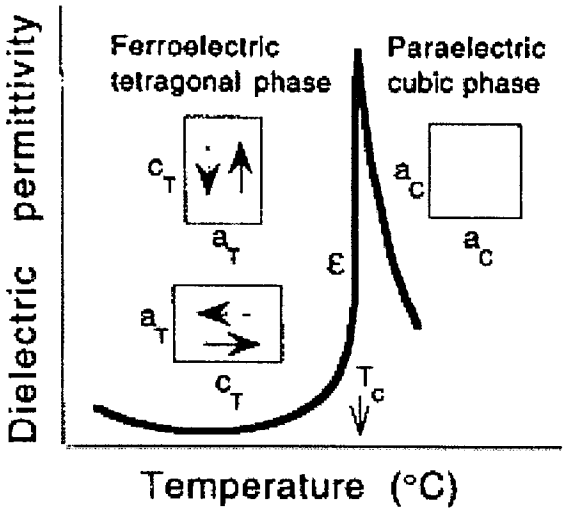

Figure 2-6 Ferroelectric phase transition temperature between ferroelectric tetragonal phase and non-ferroelectric Para electric cubic phase(28).

As discussed previously, the ferroelectric properties of a Perovskite cubic cell stems from its asymmetry. When the material is heated above its ferroelectric-curie temperature, the non-centrosymmetric tetragonal cells become centrosymmetric cubic cells. This results in the ferroelectric dipoles losing their overlocking position, and behaving as dielectric dipoles instead. For some materials like Barium Titanate ($BaTiO_3$), the material goes through several phase transitions into multiple ferroelectric phases as the temperature drops below the ferroelectric-Curie point, in this case, the first transition between a dielectric and a ferroelectric phase is marked as ferroelectric Curie point. Due to the loss of ferroelectricity, the ferroelectric-Curie point indicates the maximum operating temperature for many devices. For most materials, this is significantly above room temperature, such as 115^{o}C for BaTiO3(30), making them suitable for most personal and portable electronics, but achieving reliable high ferroelectric-Curie temperature materials is a challenge for automotive, industrial and aeronautical industries(31).

2.3.2 Ferromagnetism

The origin of the individual magnetic moments of materials originates from two sources, the orbit of electrons around atoms, and the spin of electrons themselves. As seen in figure 2.7(32), an electron orbiting at nucleus is in effect an electronic charge following a small current loop. Like a solenoid, this current loop generates a magnetic field whose direction is dependent on the direction and polarity of the current flow. In addition to the electron's orbit, the electron itself spins around its own axis, generating magnetic moment. This rotation may only spin 'up' or antiparallel 'down'.

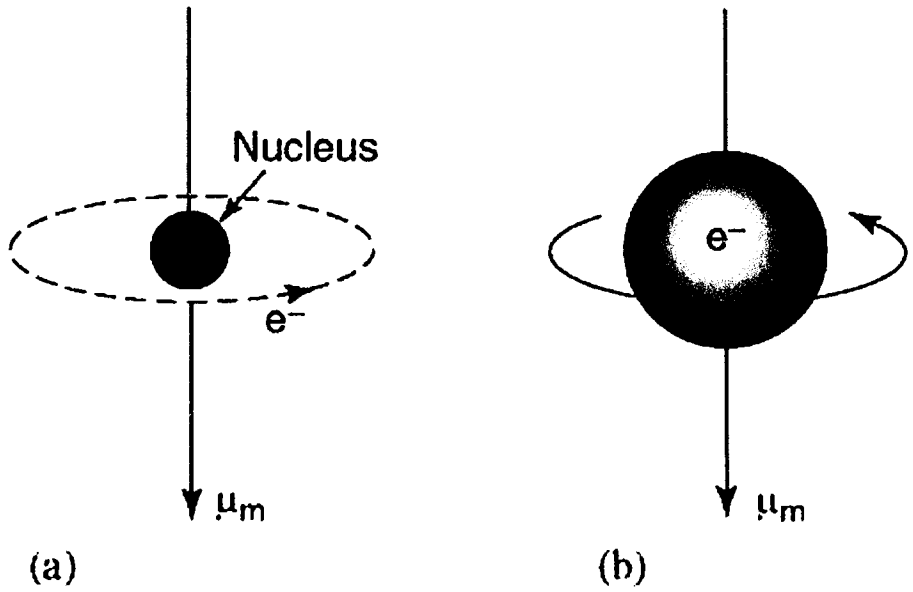

Figure 2-7 The magnetic moment generated by an electron, (a) orbital path of an electron around a nucleus, (b) rotation of electron on its own axis(32).

Though each electron in an atom produces its own magnetic field, the electrons around an atom are paired up into 'Up' and 'Down' rotations, resulting in their magnetic fields cancelling out. An atom that has completely filled shells will have all of its orbital and rotational spins cancelled out, preventing the material from becoming permanently magnetised.

Magnetism comes in the primary forms of ferromagnetism, paramagnetism and diamagnetism. Diamagnetism and paramagnetism are non-permanent forms of magnetism and are demonstrated in figure 2.8.

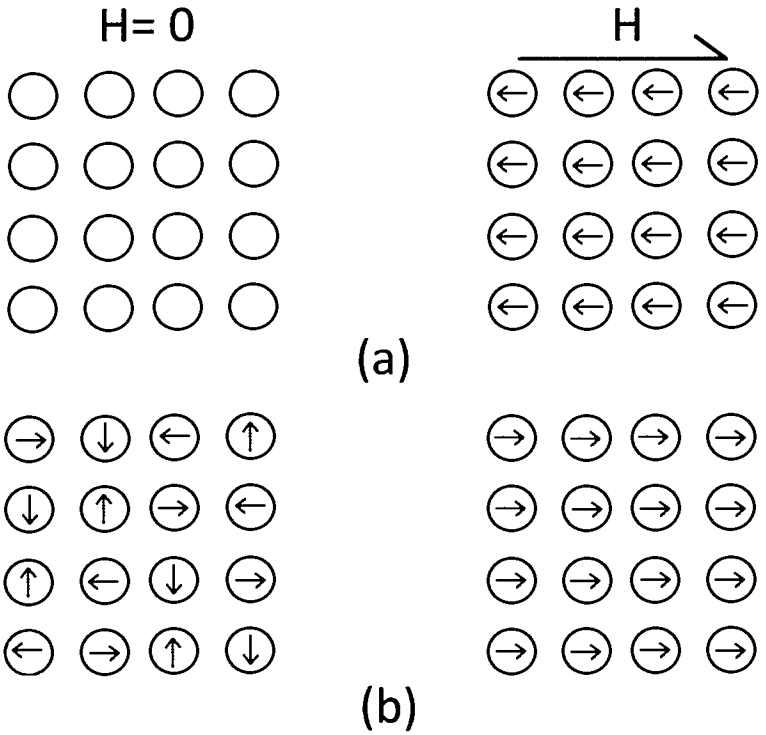

Figure 2-8 Atomic magnetic dipole moments of diamagnetic and paramagnetic materials with and without applied magnetic field (H). (a)(left) A diamagnetic material without the presence of a magnetic field, no dipoles are present (right)A diamagnetic material in the presence of a magnetic field, the dipoles oppose the external magnetic field. (b)(left) Paramagnetic material without an external magnetic field. The magnetic dipoles are randomly orientated, resulting in no magnetisation, (b)(right)paramagnetic material, magnetic dipoles align with an external magnetic field, producing a net magnetisation.

Diamagnetism is a very weak form of magnetism, and exists only whilst an external magnetic field (H) is applied. It occurs when the orbital motion of electrons reacts to the magnetic field(33). The orbits rotate to oppose the applied magnetic field, producing a very small magnetisation (M) that opposing the applied dielectric field. Diamagnetism is an extremely weak form of magnetism found in all materials, however, it is so small that it is only observable when all other forms of magnetism are absent.

Paramagnetism occurs in materials that possess incomplete electron shells, leading to the incomplete cancellation of electron spins and orbits. This results in each atom possessing a permanent magnetic moment. Outside an magnetic field, these permanent magnetic moments possess a random orientation, resulting in no net magnetisation across the material. As they are free to rotate when a magnetic field is applied, they will rotate to align with an external magnetic field, generating an internal field across the material. If the external field is removed, the atomic dipoles will rotate back into random orientation. As neither diamagnetic nor paramagnetic materials are capable of magnetism outside of an external magnetic field, neither are considered magnetic.

A ferromagnetic material is one that can preserve a very large magnetic magnetisation outside of a magnetic field, unlike diamagnetism and paramagnetism. The permanent magnetic moments of

ferroelectrics arise from non-cancelled electron spins due to incomplete electron shells like in a paramagnetic material, however, coupling also occurs between adjacent atoms causing them to align with one another, even without the presence of a magnetic field. These aligned electrons from large regions called domains.

The magnetic dipoles in a domain all face the same direction. The regions between domains are called domain walls and consist of regions where dipoles gradually change their orientation between each domain. Figure 2.9 demonstrates how zero-net magnetic moment occurs across the material without the presence of a magnetic field, as the randomly orientated domains cancel each other out. However, when an external magnetic field is applied, domain walls will move. Resulting in domains that are aligned with the field growing, and those that opposed shrinking. This change in domain boarders results in a net magnetisation across the material, as the domains that are aligned with the magnetic field, are now significantly larger than those opposed to it. Domains are typically microscopic in size, so macroscopic grains in a polycrystalline form will possess multiple domains.

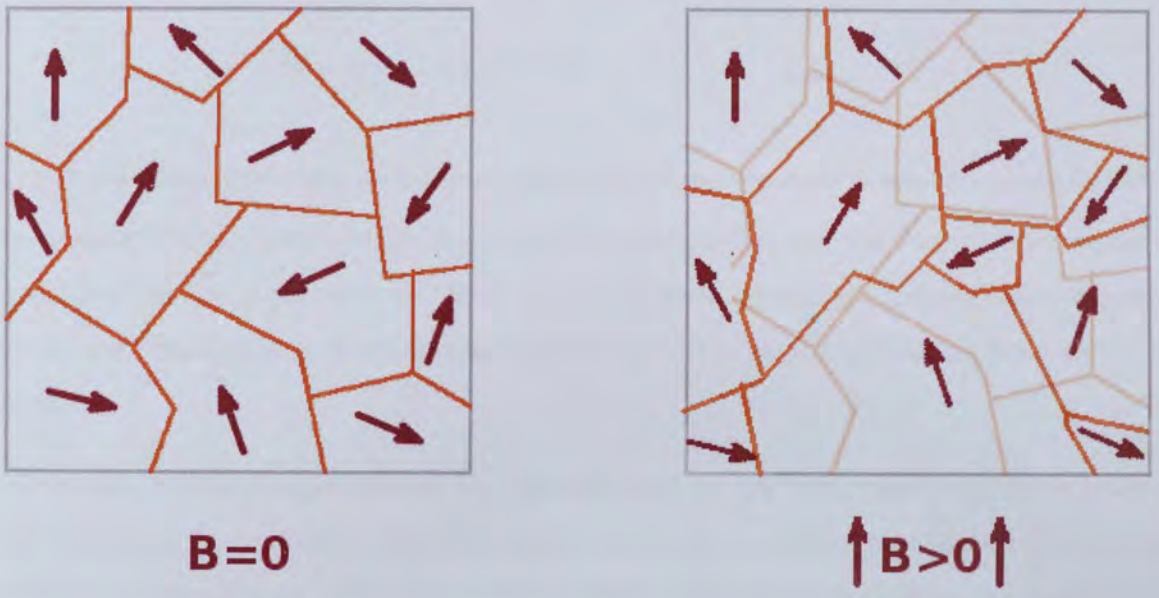

Figure 2-9 Magnetic domains in a ferromagnetic material. When B = 0, domains are equivalent size resulting in no flux. With the application of a magnetic field, domains aligned with the field grow whilst those opposed shrink, leading to polarisation across the material(34).

Figure 2.10 demonstrates how the movement of domains walls results in a magnetic hysteresis effect in ferromagnetic materials(34). Initially, when no magnetic field is applied (H=O), zero magnetisation (M=0) occurs across the material as the randomly orientated domains cancel out. As a magnetic field is applied, domains aligned with the field begin to grow and those opposed shrink, resulting in magnetisation increasing across the material in parallel with the direction of the applied field. The growth of domains continues until every single domain is aligned with the magnetic field remains.

When these domains fully align themselves with the magnetic field, the material is said to have reached magnetic saturation (M_S).

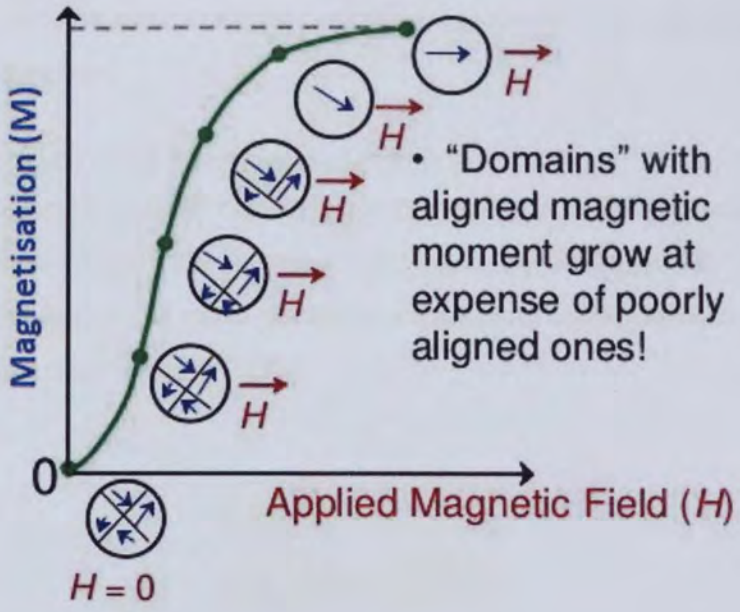

Figure 2-10 The process of ferromagnetic hysteresis, (domain walls changing to match an external magnetic field(35).

As the magnetic field is lowered from the point of magnetic saturation, the magnetisation across the material begins to drop but does not follow its original path. Instead, the magnetisation drops at a reduced rate, resulting in a remnant magnetisation once the magnetic field has been completely removed.

This non-zero remnant magnetisation can be explained by the movement of domain walls. As described previously, randomly orientated domains form a single domain aligned with the field when magnetic saturation occurs. When the applied magnetic field begins to reverse, the single domain breaks down into smaller, unaligned domains. The generation of new domains, however results in the creation of new domain walls, which face resistance whilst creating domains opposing the direction of the current magnetic field. When the magnetic field is fully removed, this resistance results in a net magnetisation remaining in the direction of the original field. To obtain a non-magnetised material, a magnetic field in the opposite direction must be applied. The required magnetic field is called the magnetic coercive field, (H_C). By increasing the magnetic field in the opposite direction, an equal and opposite saturation magnetisation can be obtained, forming a magnetic hysteresis loop.

Ferromagnetism occurs due to the ordering of ferromagnetic dipoles with ferromagnetic domains, this ordering of domains however disappears at what's known as the ferromagnetic Curie temperature. When a material passes the ferromagnetic-Curie temperature thermal vibrations overwhelm the spin coupling that makes up ferromagnetic domains. This results in ferromagnetic domains breaking down, and the material becoming paramagnetic. Like the ferroelectric-Curie temperature, the ferromagnetic-Curie temperature represents the operating limit range for ferromagnetic based devices.

2.3.3 Multiferroics and Magnetoelectrics

Multiferroic materials are a group of materials that possess multiple ferroic orders in a single phase. These may include ferroelectricity, ferromagnetism and ferroelasticity(36). Coupling can occur between the ferroic orders, resulting in a change in one ferroic order producing a spontaneous change in another, as demonstrated in figure 2.11.

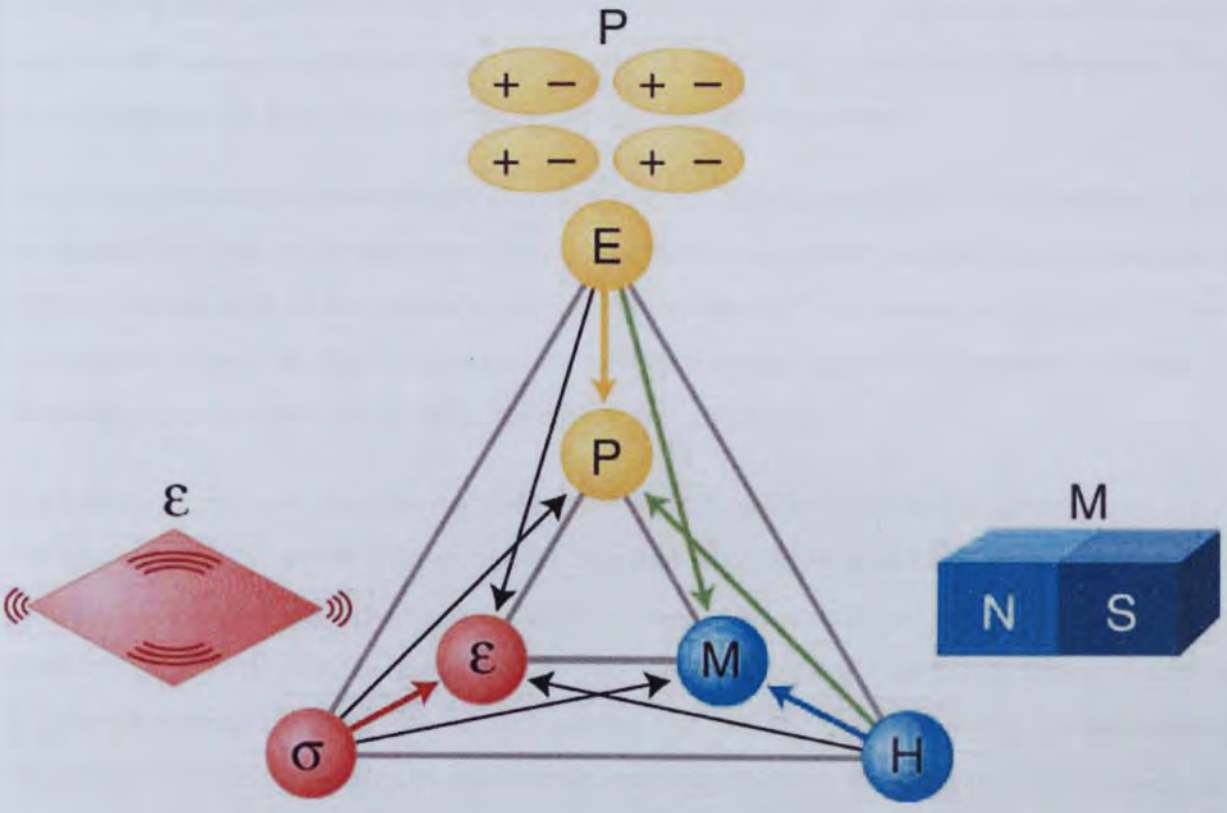

Figure 2-11 Examples of multiferroic coupling in the ferroelectric, ferromagnetic and ferroelastic orders. Applied electric fields (E), results in changes to the magnetisation (M) and strain(ε). Applied magnetic fields (H) results in changes to the electric polarisation(P) and strain(ε), and applied stress(σ) results in changes to the electric polarisation(P) and magnetisation(M)(37).

The branch of multiferroics that possess coupling between the ferroelectric domain and ferromagnetic domain are called magnetoelectrics. In these materials, a change in the ferroelectric domains influences the ferromagnetic magnetisation and vice versa. This means that it is possible to control

the magnetisation with an external electric field, and the electric polarisation using an external magnetic field. This effect was first discovered in the 1960's, however, it was not until the start of the 21st century that the switching of an electric polarisation using a magnetic field was first demonstrated using $TbMnO_3$(38) and $TbMN_2O_5$(39).

As previously discussed, as the industry approaches the practical limits of Moore's Law, there is a demand to increase the quality of devices through increased diversification, known as 'More than Moore'. This challenge has been tackled by the integration of new functionalities into devices utilising the magnetoelectric effect. Recently, a range of new prototype devices have been developed using this effect. These include magnetic field sensors to help overcome the slow response time and operating temperature of semiconductor devices(40), energy harvesting devices for mobile and isolated electronics(41), and wide range frequency phase shifters(42). In this thesis, the specific field of application of interest is that of magnetoelectric memory applications. The progress into the development of magnetoelectronics has been hampered by the lack of single-phase magnetoelectric materials with strong coupling and room temperature behaviours. Alternatives to single phases have been explored in the form of ferroelectric/ferromagnetic heterojunctions.

Heterojunctions consist of ferroelectric and ferromagnetic layers deposited upon one another. When the polarisation state of the ferroelectric layer changes due an applied electric field, it undergoes a change in strain due to the piezoelectric effect, this results in a change in strain of a joined ferromagnetic layer. As the ferromagnetic layer experiences strain, it undergoes a change in ferromagnetic polarisation due to the magnetostriction effect (32).

Single phase magnetoelectric materials are still desirable, in order to achieve a magnetoelectric effect that's tuneable on the atomic level (4), and for their simplicity, allowing for high throughput. For these materials to become a reality, a material with strong magnetoelectric properties at room temperature is required. One of the leading research paths into achieving this is the elemental doping of existing multiferroic materials to induce or enhance existing magnetoelectric coupling(43). The next section presents an in-depth consider the multiferroic material, $Bi_4Ti_3O_{12}$, which forms the basis of this investigation.

2.4 Multiferroic thin films

As explained previously, multiferroic materials with strong magnetoelectric coupling offer the opportunity for high-quality memory devices with increasingly diverse functions. The main challenge of multiferroic materials so far has been the search for a single-phase material with strong

ferromagnetic and magnetoelectric coupling properties at room temperature. To this end, extensive materials research into elemental doping and substitution of existing materials is being performed, in order produce a material with ideal multiferroic properties. Additionally, there is interest in the use interface layers, which can control the crystalline properties and orientation of the thin films, to tune the properties of thin films. This subchapter looks in at one of the leading magnetoelectric materials, $Bi_4Ti_3O_{12}$, and discusses how elemental doping and interface layers can be used to improve its electrical properties, and concludes with this thesis aim and contribute to the field.

2.4.1 Perovskite and Aurivillius Phase Structures

A large quantity of ferroelectric materials being investigated consist of Perovskite and Aurivillius crystalline structures. The Perovskites are a large family of materials that were first discovered by the Geologist Gusta Rose in the 1830's, who named them after the famous Russian Mineralogist, Count Lev Aleksevich Von Perovski(44). The general formula for Perovskite is ABX3, where A and B metallic cations of different size, and X are non-metallic ions, most commonly oxygen. The structure of perovskite $SrTiO_3$ is demonstrated in figure 2.12(45).

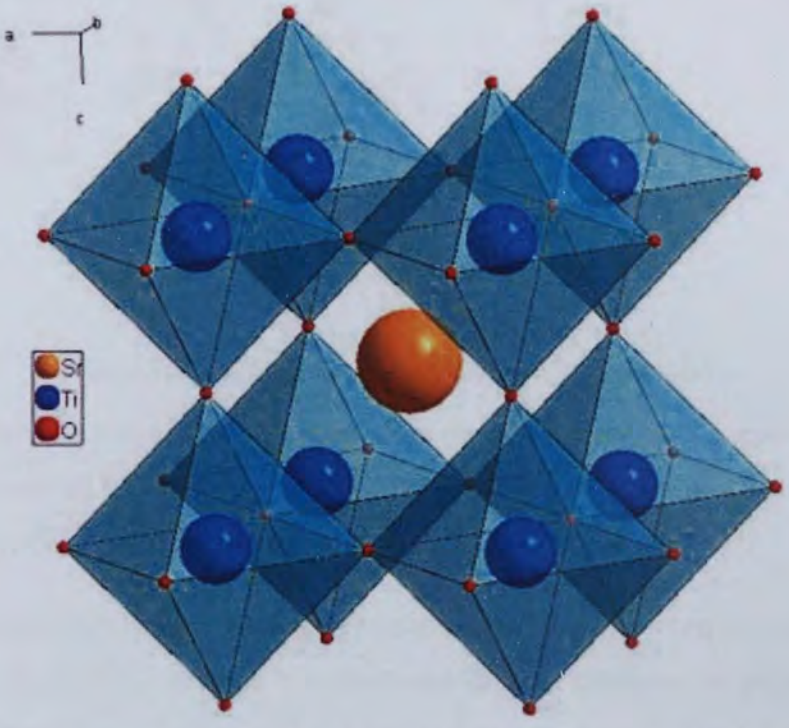

Figure 2-12 The structure of Perovskite mineral, SrTiO3. Here the formula, ABX3 is A = Sr, B=Ti and O = 3 (45).

B cation forms B-X-B bonds with the X cation, forming a cubic structure in which the A cation, which is typically larger than the B cation, and is located in the centre. A wide range of different elements can fill A and B cation slots, opening up a huge range of elemental combinations, and highly tuneable

electrical properties. Certain elemental combinations, such as barium titanate ($BaTiO_3$), lead to distortion of the cubic lattice due to the large barium cation size. This asymmetry leads to the ferroelectric properties found in some Perovskite, as described earlier. Another similar class of material is the Aurivillius structure, presented in figure 2.13.

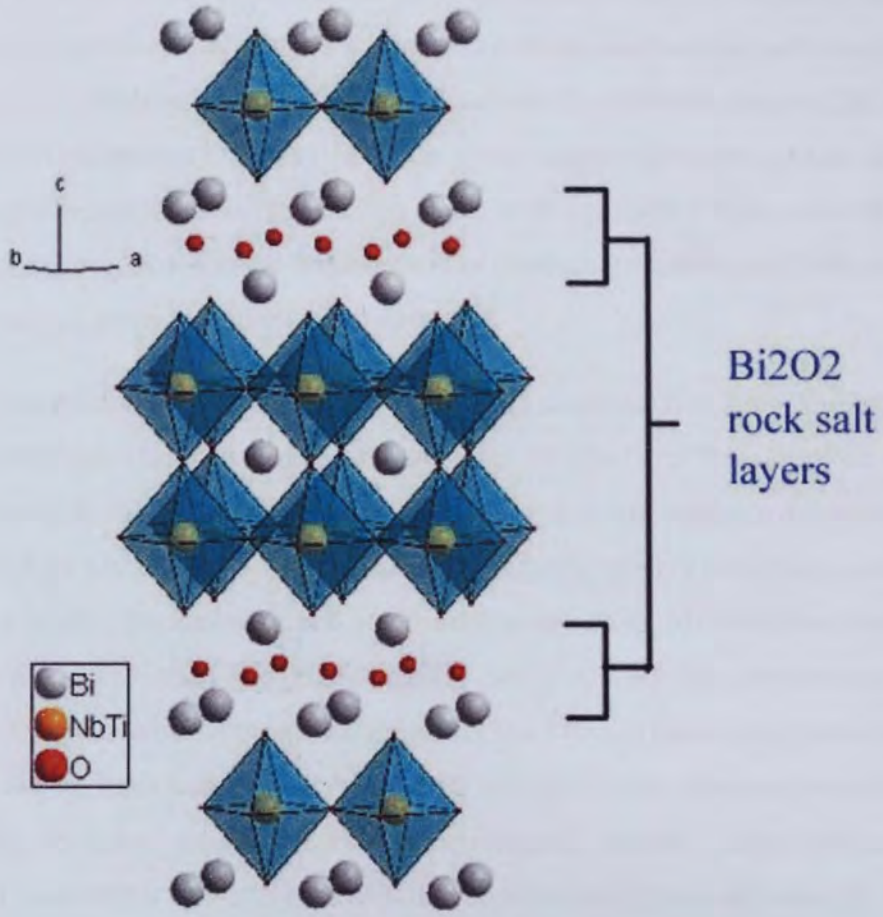

Figure 2-13 Aurivillius phase structure of (Bi_2O_2)-$Bi(Ti,Nb)_2O_7$ (45).

The Aurivillius phase structure consists of a number of Perovskite cubic layers separated by Bi_2O_2 rock salt layer. These materials have the general formula $(Bi_2O_2)(A_{n-1}B_nX_{3n+1})$ where, A and B are cations, X is a non-metallic cation and n is the number of rock salt layers.

The utilisation of Aurivillius phase materials represented an important step in minimising fatigue in Perovskite based devices(46). Fatigue is a challenge faced by Perovskite materials, and is the occurrence of a reduction in polarisation with repetitive switching cycles. One of the key reasons for fatigue is the build-up of space charge near the electrode/ferroelectric interface, which works to compensate for the applied electric field. The Bi_2O_2 layers work to counteract this by having their own net charge, which prevents the build-up of charge at the electrode interface, significantly reducing fatigue rates (47, 48). Another key benefit of the rock salt layer is its highly resistive nature. When

current flow through the material is perpendicular to the rock salt layer, it faces increased resistivity, compared to parallel flow. This makes perpendicularly orientated Aurivillius materials preferable for low leakage, high resistance devices(49).

2.4.2 Electrical and Magnetic Properties $Bi_4Ti_3O_{12}$

$Bi_4Ti_3O_{12}$ is an Aurivillius phase structure that forms the focus of this research. Its structure consists of bismuth rock salt layers separating three bismuth titanate Perovskite layers with the general formula $(Bi_2O_2)^{+2}(Bi_2Ti_4O_{10})^{-2}$. It's lattice constants are, a = 0.545nm, b = 0.541nm and c = 3.282nm (50). Below its ferroelectric curie point of 657^{O}C(51), BTO has a ferroelectric tetragonal phase, which becomes a non-ferroelectric monoclinic symmetric when above it. The transition from a non-ferroelectric to a ferroelectric phase occurs due to the displacement of the bismuth cations, which results in bending of the TiO_6 octahedron and a reduction in symmetry(52).

BTO has a strong electronic isotropy, with a documented polarisation of $2pr = 95\mu C/cm^2$ and coercive field of 2E c= 90 kV/cm along the a and b-axis, and $2pr = 7\mu C/cm^{-2}$ and 2Ec = 20 kV/cm along the c-axis in the bulk phase(53). The large difference in polarisation is due to the large difference in the atomic displacement of the bismuth atoms. It possesses a larger displacement and a larger polarisation in the A-B axis, and a smaller displacement and polarisation in the c axis. BTO thin films are typically C-axis orientated on platinum (54-56) and [100] silicon (57, 58) substrates. The preference for C-axis growth is due to the mismatch between the crystal lattices of the BTO and substrates. As the lattice constants between the two surfaces layers are different, BTO will grow in the direction that minimises surface energy leading to C-axis growth on most substrates(56). Whilst it does possess the smallest polarisation, C-axis BTO is one of the candidates for ferroelectric memory devices, due to its's low leakage current and small coercive field, with low electric coercivity necessary for fast switching devices.

2.4.3 Site Engineering and Atomics Substitution.

As discussed previously, the electronic properties of Perovskite and Aurivillius structures can be improved and tailored by the substitution of rare earth elements into A and B cation sites. The aims of various substitutions have included improving the fatigue properties, reducing leakage current, increasing the remnant polarisation and reducing the coercive field. Additionally, there are recent investigations into enhancing the ferromagnetic properties of BTO by iron and cobalt doping. This subchapter details the elements doped into the BTO thin films in this investigation, in order to improve its ferroelectric and ferromagnetic properties, with the aim of making it an ideal candidate material for magnetoelectric memory devices.

2.4.3.1 A-site - Lanthanum

As lanthanum and bismuth have similar atomic radiuses, lanthanum is easily substituted into bismuth ions sites without distorting the Perovskite structure. As previously discussed, the (Bi_2O_2) layers in Aurivillius materials assist in reducing fatigue in $Bi_4Ti_3O_{12}$ bulk materials, however BTO thin films still present fatigue properties. Back in 1999, Park et al (48) demonstrated how the substitution of lanthanum atoms into bismuth positions, forming $Bi_{3.25}La_{0.75}Ti_3O_{12}$(BLT), produced fatigue resistant thin films. Figure 2.14 demonstrates how the insertion of lanthanum improved the fatigue properties of BTO thin films(48).

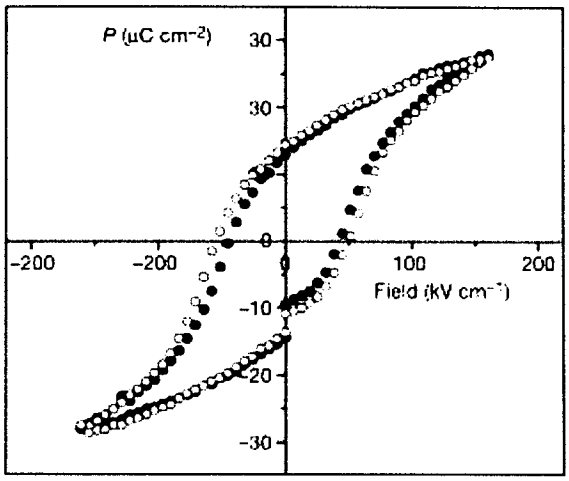

Figure 2-14 Polarisation – electric Field (P-E) loops for BLT thin films, with the initial P-E loop in closed circles, and P-E loops after $3x10^{10}$ read/write cycles in open circles(48).

By comparing the P-E properties of BLT thin films before (closed circles) and after (open circles) 3 x 10^{10} read/write cycles at 1 MHz. It is demonstrated how after repeated readings, no serious change in the symmetry of the remnant polarisation and coercive field can be seen. Even today, there are still several models for explaining the fatigue free behaviour of lanthanum substituted BTO. The prominent theory being that lanthanum can increase the chemical stabilities of oxygen vacancies in the Perovskite layers after lanthanum substitution which assist in preventing domain wall pinning(59) (60). In this investigation, the same amount of lanthanum substitution is utilised in the BTO thin films here as in the aforementioned Parks experiment, as fatigue free ferroelectric behaviour is highly desirable in magnetoelectric memory.

2.4.3.2 B-site - Niobium

In 2006, Singh et al(61) performed a systematic investigation into the effect of niobium doping concentration in B-sites in $Bi_{3.25}La_{0.75}Ti_{3-x}Nb_xO_{12}$ (x =0-0.1) on platinised silicon substrates via chemical deposition solution. The experiments were based on other reports demonstrating improved remnant

polarisation with niobium doping via the chemical solution route(62) and pulsed laser deposition(63). The changes were attributed to the distortion of the TiO_6 octahedron due to the increased ionic radius of the Nb^{5+} ion, which increases ferroelectric ionic displacement. Figure 2.15 shows the XRD patterns for $Bi_{3.25}La_{0.75}Ti_{3-x}Nb_xO_{12}$, for X= 0.0, 0.04, 0.05 and x = 0.1(61).

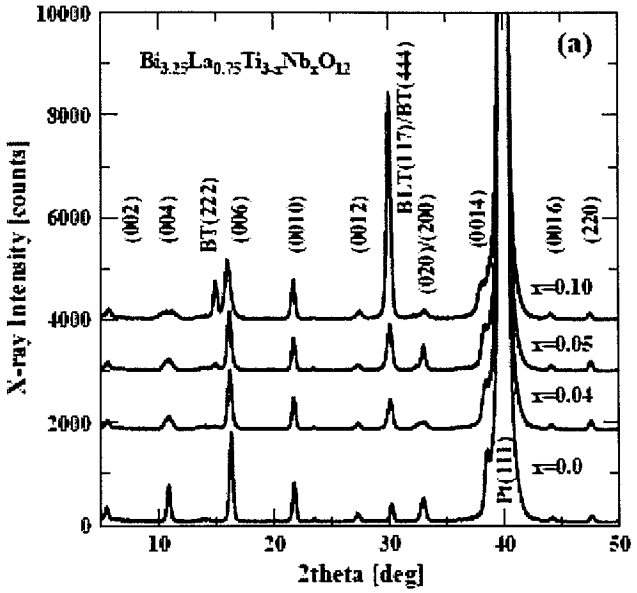

Figure 2-15 X-ray diffraction pattern of Bi3.25La0.75Ti3-xNbxO12 for X= 0.0, 0.04, 0.05 and x = 0.1(61).

Between niobium concentrations of X = 0.0 and 0.04, no major change in structure can be seen. However, for concentrations above x=0.04, major secondary phase $Bi_2Ti_2O_7$ appears. It can be observed that the BTO peaks shift to a lower angle with increasing niobium doping, and is most evident in the (006) phase, which the author attributed to the TiO_6 octahedron d-spacing increasing due to the larger ionic radius of the niobium dopants. Figure 2.16 demonstrates the effect of niobium doping on the remnant polarisation, coercive field and leakage current of BTO thin films(64).

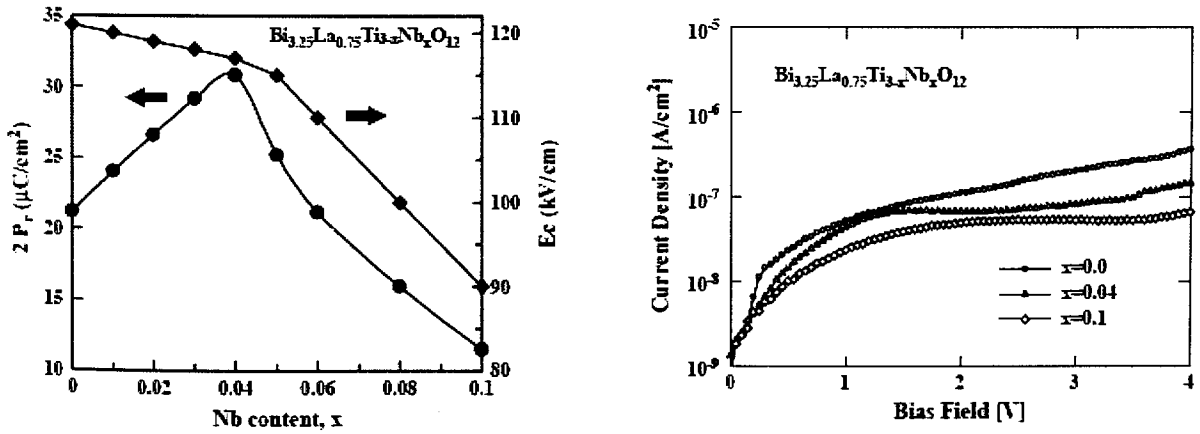

Figure 2-16 the effect of niobium doping on the electronic properties of Bi3.25La0.75Ti3-xNbxO12, (left) remnant polarisation (2Pr) and coercive field (Ec), (right) leakage current(61).

As niobium content rises from 0 to 0.04, remnant polarisation increases due to increased TiO_6 octahedron bending(61). As the niobium concentration was increased further, the polarisation began to drop, which they credited to the appearance of the non-ferroelectric $Bi_2Ti_2O_7$ phase. The effect of niobium on the leakage current was also investigated. The investigation found that leakage current decreased with increasing niobium concentration. The increasing resistivity between X = 0.04 and X = 0.1 was attributed to the appearance of the highly insulative pyrochlore phase(65).

In addition to improving the ferroelectric properties, niobium substitution has been proven to influence the dielectric properties as well. The insertion of niobium into BTO as previously discussed increases the d-spacing of the TiO_6 octahedron, increasing the dielectric constant of BTO (66). In this investigation, the niobium dopants are inserted into B-site site location, in order to increase the remnant polarisation of the thin film.

2.4.3.3 B-site - Iron and Cobalt

In recent years, BTO doped with iron and cobalt shown to produce magnetic properties in the bulk form. In 2008, Mao et al examined the magnetic properties of $Bi_4Ti_3O_{12}$ doped with multiferroic $BiFeO_3$ to form $Bi_5FeTi_3O_{15}$ bulk pellets(67). Their investigation found it induced very weak paramagnetism, with a small remnant magnetisation which they attributed to a small degree of ferromagnetism. Later in 2012(68), Mao did a comparative study of the same material with half iron dopants substituted to for cobalt. Figure 2.17 shows the M-H response of $Bi_5FeTi_3O_{15}$ and $Bi_5Fe_{0.5}Co_{0.5}Ti_3O_{15}$ from their investigation.

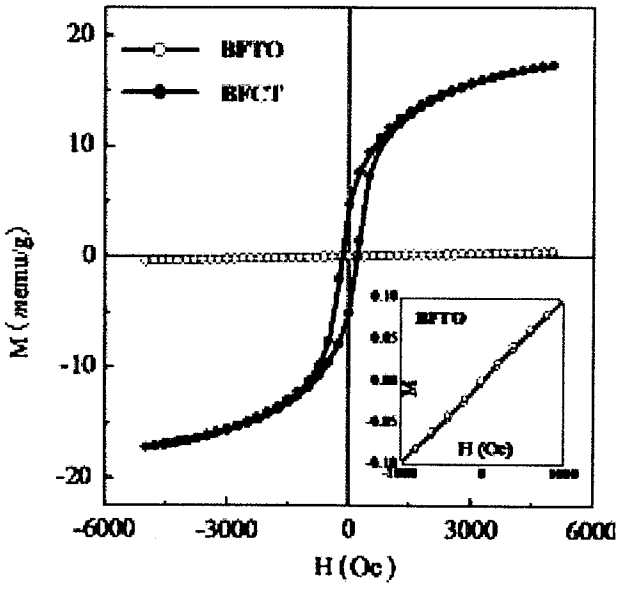

Figure 2-17 The M-H curve of Bi5FeTi3O15 (BFTO) and $Bi_5Fe_{0.5}Co_{0.5}Ti_3O_{15}$ (68).

$Bi_5Fe_{0.5}Co_{0.5}Ti_3O_{15}$ shows clear ferromagnetic behaviour, with a distinct magnetic saturation, and a remnant magnetisation (2Mr) of 7.8 memu/g and a coercive field ($2H_c$) of 410Oe. In contrast, pure iron doped $Bi_5FeTi_3O_{15}$ shows weak paramagnetism, with a weak remnant magnetisation of 2.7×10^{-3} memu/g, a thousand times smaller than that of BTFC with both Iron and cobalt doping.

As Co^{3+} ions have smaller magnetic moments than Fe^{3+} ion, an explanation based purely on the magnetic moment is not enough (69). Mao et al claimed that the rise in the ferromagnetism came from the long-range ordering of magnetic iron and cobalt ions(68). In $Bi_5Fe_{0.5}Co_{0.5}Ti_3O_{15}$, the concentration of iron and cobalt is even, resulting in a greater possibility of the Fe-O octahedron and the Co-O octahedron being close to one another, this results in a high probability of direct Fe-O-Co coupling which favours the ferromagnetic state.

Since the beginning of this project, more work has been performed that provides additional information on to the effect on iron and cobalt doping. In August 2013, Chen et al(4) demonstrated the effect of cobalt and iron doping in $Bi_4Ti_3O_{12}$ thin films and the resulting ferromagnetic and magnetocapacitance (MC) effect. As magnetic fields can induce changes in polarisation in a magnetoelectric material, changes in magnetic field must also induce change in the materials dielectric constant. This is called the magnetocapacitance effect, and provides a method to confirming magnetoelectric behaviours by measuring the dielectric constant under a range of magnetic fields.

The investigation performed by Chen et al involved bulk materials $(Bi_{3.15}Nb_{0.85})(Ti_2Fe_{0.5}Co_{0.5})O_{12}$ developed by solid state sintering, which retained it's three-layer Perovskite structure despite the heavy cobalt and iron doping. Figure 2.18 shows the ferroelectric, ferromagnetic and magentocapaitance effect for $(Bi_{3.15}Nb_{0.85})(Ti_2Fe_{0.5}Co_{0.5})O_{12}$ bulk samples investigated by Chen et al(4).

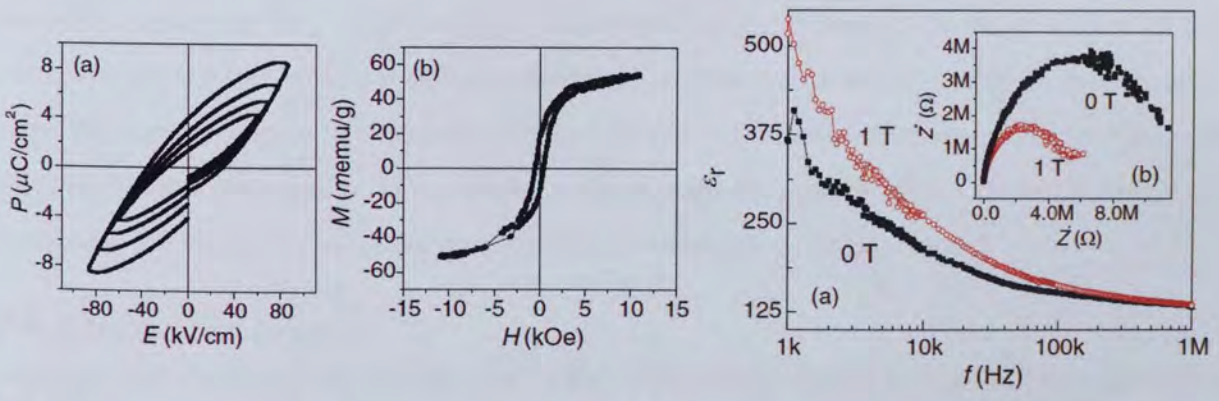

Figure 2-18 Ferroelectric loop PvE (left) Ferromagnetic Loop MvH (middle) magnetocapacitance effect fvε (right) Cole-cole plot (right, insert) for $(Bi_{3.15}Nb_{0.85})(Ti_2Fe_{0.5}Co_{0.5})O_{12}$ (4).

The ferroelectric hysteresis loop showed a maximum polarisation of 8 $\mu C/cm^2$ at an applied field of 86 kV/cm(4). The ferroelectric loop did not saturate, due to the samples low break down voltage, which

they attributed the poor density of the material. The MvH loop shows clear ferromagnetic behaviour with a remnant magnetisation (2Mr) of 32 memu/g and a coercive field (Hc) of 872 Oe.

The magentocapaitance measurement was performed by measuring the frequency response of the relative permittivity, with and without an applied magnetic field of 1 Tesla (T). It can be clearly seen that the relative permittivity of the material is enhanced by the presence of a magnetic field, indicating that the insertion of iron and cobalt into BTO induces the magnetoelectric effect.

The reason that iron and iron doping induces ferromagnetism in BTO is still not fully understood, but there are two prevailing theories. The first theory is that insertion of both iron and cobalt results in the formation of direct Fe-O-Co states, which favour ferromagnetism(68). Another prevailing theory, is that the different ion sizes between Fe and Co(70) results in structural distortion leading to a canted spin state, as seen in figure

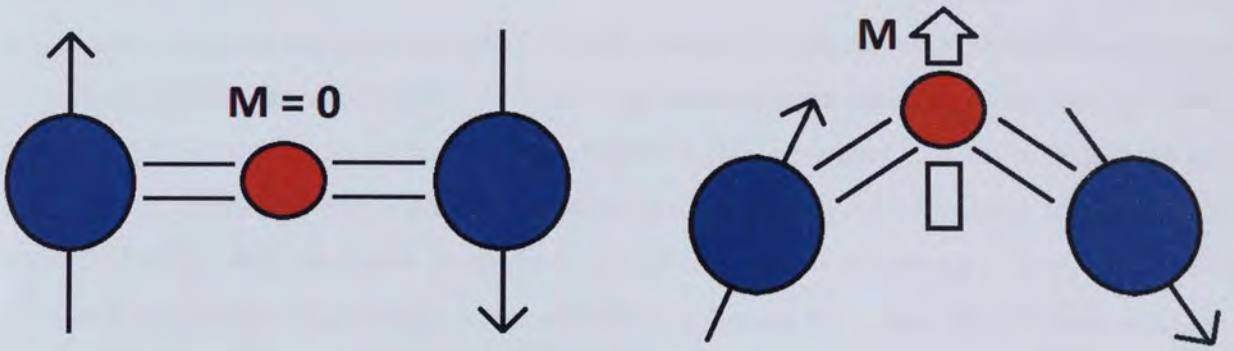

Figure 2-19 (left) Co-parallel spin structure, (right) Canted spin structure.

Normally, two ions of equal size are positioned either side one oxygen atom in the perovskite structure, they spin in co-parallel to one another, resulting in the magnetic moment of either ion cancelling each other out, leading to zero net-magnetisation. However, by inserting ions of two different sizes, the spin structure becomes distorted, leading to a canted spin state, and uncancelled magnetic moment leading to a net magnetisation across the material. Both iron and cobalt dopants are utilised in this investigation, by comparing the ferromagnetic properties of our thin films and those reported in the literature, we aim to contribute to understanding this phenomena.

2.4.4 Interface layers

The deposition of oxide thin films onto silicon substrates presents several difficulties. These difficulties arise due to the generation of interfacial charge traps between the thin film and substrate, and/or the diffusion of atoms from the thin film into the silicon(71). These challenges can be addressed by the insertion of an interface layer between the substrate and thin film, which is deposited onto the

substrate, prior to thin film deposition. In addition to influencing the crystalline properties of the deposited thin film, interface layers can also be utilised as rear electrical contacts.

Most investigations into BTO and other ferroelectric thin films on silicon utilise platinum interface layers(72). Platinum is a preferred interface layer due to its high conductivity and thermal stability, making it a suitable rear-electrical contact. It retains its conductivity when annealed at high temperatures in an oxygen rich atmosphere, were-as conductive silicon and other metals would oxidise, losing their conductivity, or go through thermal expansion damaging the thin film deposited upon them. The platinum layer also functions as an effective diffusion barrier due to the large platinum atom size preventing diffusion between the substrate the thin film. Whilst it is commonly used, the use of platinum can lead to poor absorption of oxygen, and thermally induced imprint(73). Due to this, other interface layers are being investigated, including IrO_2(74), SiON(75) and Al_2O_3(76).

Due to there being interest in new high dielectric constant oxide materials needed to replace SiO_2, which currently serves as a gate electrode for CMOS devices (77, 78), there has recently been interest in the integration of ferroelectric thin films with new semiconductor substrates and interface layers. ZnO is of particular interest in ferroelectric/semiconductor structures due to its wide-band-gap, piezoelectric, optical(79) and electrical properties(80) and its similar processing temperature of BTO(81). Recent work has been performed to characterise the properties of ferroelectric BTO deposited onto sapphire substrates coated with semi conductive ZnO, where the BTO presents a rare A-axis orientation(5). Therefore, there is interest in the integration of BTFC thin films with ZnO semiconductor interface layers on silicon substrates, for future applications in BTO/ZnO Metal-Ferroelectric-Semiconductor structures.

In this investigation, ZnO is utilised as an interface layer when depositing BTFC onto silicon substrates, due to the current interest in utilising ZnO in ferroelectric/semiconductor structures. The aim is to see how the crystalline properties of BTFC thin films on silicon can be improved by the insertion of the ZnO interface layer, and to provide a foundation for future investigations into BTFC/ZnO heterostructures.

2.5 Research Goals and Aims

This chapter has demonstrated to the reader the demand for single phase magnetoelectric materials, stemming from the need to develop practical magnetoelectric memory devices to further increase memory device value as minimisation reaches its practical limitations. To meet this demand, we will be investigating Aurivillius phase material BTO with lanthanum, niobium, cobalt and iron doping to form $(Bi_{3.25}La_{0.75})(Ti_{2.5}Nb_{0.125}Fe_{0.125}Co_{0.125})O_{12}$, which will be abbreviated as BTFC through this thesis.

Ferromagnetic BTO was recently demonstrated by Chen et al (4)and Mao et al (68) as previously discussed, however, this work was performed on bulk materials, whereas this thesis will focus on the thin film form. Whilst bulk is easier to fabricate and characterise in research, the industry requires the materials in thin film form for practical applications. Thin films present more design challenges than bulk materials, such as increased influence from the substrate interface and surface states, and more complicated fabrication procedures.

Additionally, this investigation utilises radio frequency (rf) magnetron sputtering for our thin films deposition. RF magnetron sputtering is the preferred technique for thin film deposition in industry due to its uniform surface coverage, accurate thickness control, and tuneable deposition control. These factors make research into thin films deposited by rf magnetron sputtering highly desirable for industrial applications.

Chapter 3 : The Growth and Characterization of BTFC Thin Films

3.1 Introduction

The previous chapter introduced the topic of multiferroic thin films and the surrounding field of memory devices that justify the need for this investigation. To achieve the set hypothesis, a range of bulk and thin film fabrication techniques were employed in this work, as well as a variety of characterisation techniques. The aim of this chapter is to provide a comprehensive explanation of the fabrication processes involved in the production of said multiferroic thin films, and the physical and electronic methods used to characterise them. Upon reading this chapter, the reader should fully comprehend the fabrication and characterisations methods used and understand how they achieve the necessary steps in thin film fabrication, or provide us with accurate characteristics of the involved samples.

3.2 Fabrication Equipment

The development of thin film devices is a multistage process, involving multiple fabrication methods. The first stage involves the fabrication of a bulk BTFC target using Spark Plasma Sintering (SPS) at Queens Mary University London. From this target, thin films were deposited using Aston University's rf-magnetron sputtering system, and annealed using a range of furnaces. Lastly, for the case of electrical and ferroelectric measurements, metallic contacts were deposited on the BTFC thin films surface using thermal evaporation. This chapter details these fabrication processes from a physics perspective, to inform the reader how they achieve the necessary steps in sample fabrication.

3.2.1 Spark Plasma Sintering

Sintering is the processes by which solid bulk samples are formed by the application of heat and pressure to compress the same material in another form, typically powder. In this thesis, SPS was used to fabricate the solid bulk BTFC target for sputtering. A diagram of the conventional sintering apparatus is presented in figure 3.1.

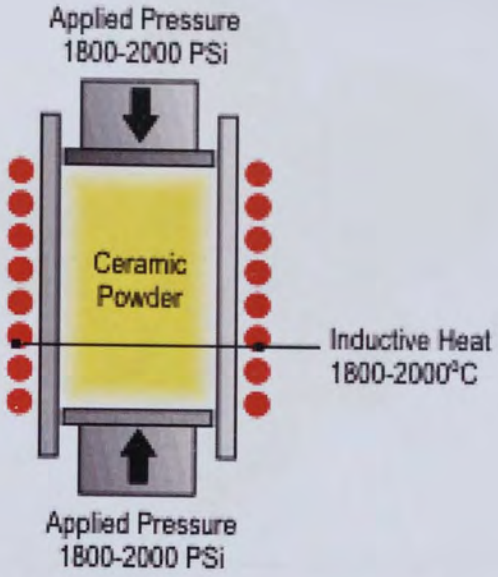

Figure 3-1 Diagram of covnentional hot pressing sintering(82) .

Conventional hot pressing (HP) sintering techniques generate heat through radiation from a surrounding furnace, which is transferred via inert gasses. This results in poor heat transfer, leading to a slow heating rate and long sintering time. In contrast, SPS generates a pulsed direct current (DC) voltage across the sample which produces thermal energy through joule heating(83). This method of heating minimises grain growth and allows for very rapid and efficient heating and fast cooling rates. The heating rate of the sample depends on the dimensions of the container, as well as the sample electrical and thermal properties, with heating rates as high as 1000^{o}C/min.

In SPS, the powder phase material sits in a conductive graphite die, allowing DC current to pass directly through the powder. Thermal energy is provided via joule heating, which occurs at the highest points of resistance. In powders, the highest points of resistance occur at the grain boundaries, as demonstrated in figure 3.2. The key advantage of this method is that heat is generated at the grain boundaries, which limits grain growth and suppresses powder decomposition.

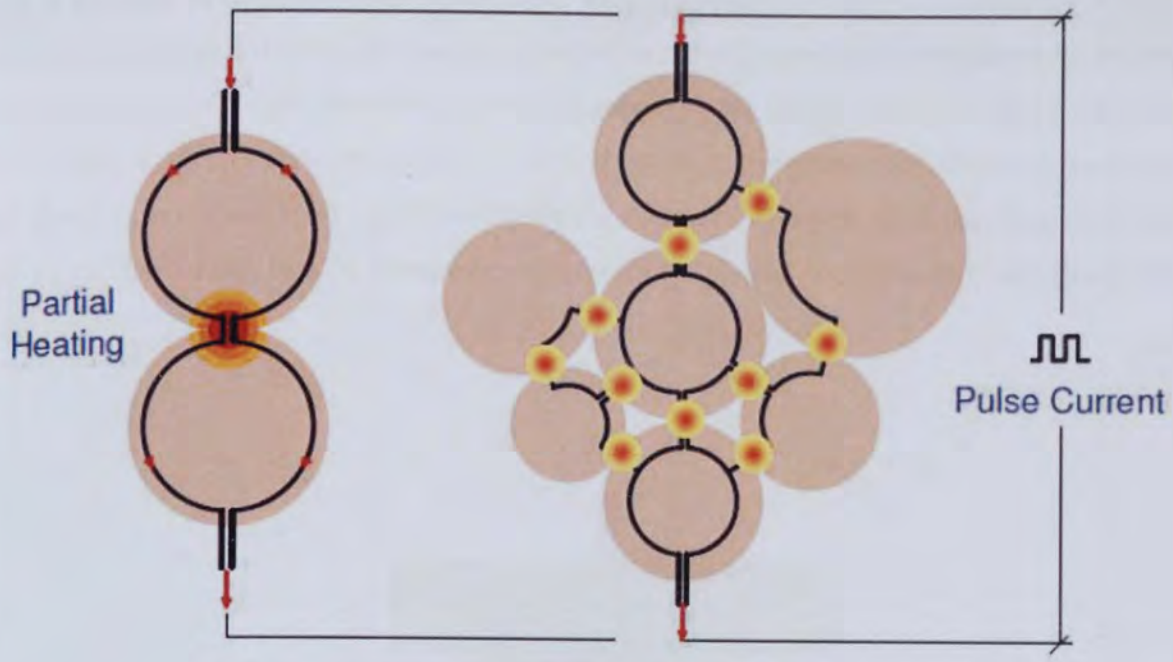

Figure 3-2 SPS, The current flow of a pulsed DC signal through grains in SPS. Thermal energy is concentrated at the grain boundaries between particles(84).

3.2.1.1 Fabrication of BTFC target

SPS was used to fabricate the stoichiometric $Bi_{3.25}La_{0.75}Ti_{2.5}Nb_{0.25}Fe_{0.125}Co_{0.125}O_{12}$ (BTFC) target with the desired elemental doping as discussed previously in chapter 2.4. To fabricate the target powders of Bi_2O_3, TiO_2 and La_2O_3 were mixed together by ball milling in ethanol for four hours at 350RPM. The mixture was calcined at 800°C for four hours. Additional powders of Nb_2O_5, Fe_2O_3, Co_2O_3 and Bi_2O_3 were mixed using the same ball milling methods with an ethanol solution. The complete mixture was then sintered using SPS at 900°C. A 3" diameter die was used to form a solid ceramic target. After SPS, the target was further annealed at 700°C and then sanded down with a mechanical sander to the required thickness. To assist in preventing thermal shock to the target during sputtering, a copper back plate was bonded to the target by indium paste. Copper was used as a back plate, as its high thermal conductivity allows it to dissipate heat from the target to the target holder more effectively. Indium paste was chosen for its high thermal conductivity, and large atom size, which prevents indium atoms from diffusing into the target.

To remove any surface states or impurities prior to any deposition, the target was sputtered for 10 hours at 150W. This processes etched away any surface states, ensuring later depositions were performed using material only from the uniform bulk of the target.

3.2.2 Radio Frequency Magnetron Sputtering

In this investigation, BTFC thin films were deposited via radio frequency (rf) magnetron sputtering by using the bulk BTFC target fabricated by SPS. Sputtering is the process by which atoms are ejected from a solid target by bombardment with energised particles. The ejected particles then travel across the chamber until they come into contact with the substrate, at which point they lose their kinetic energy and form a thin film. A standard direct current magnetron sputter is demonstrated in figure 3.3.

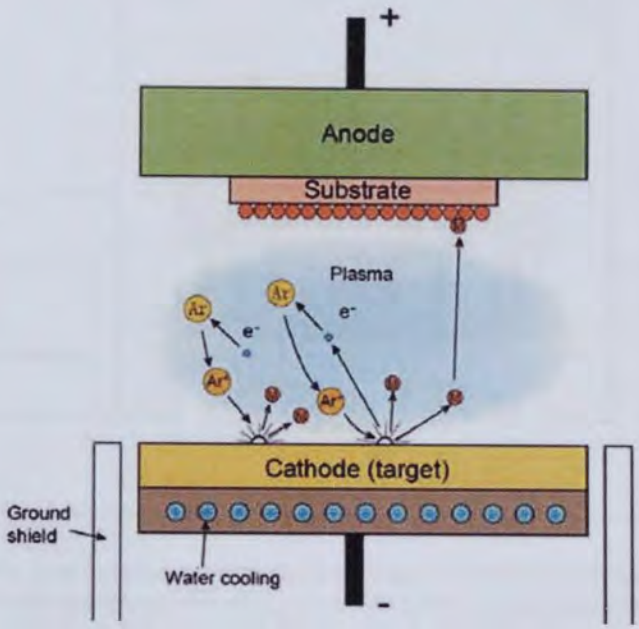

Figure 3-3 Diagram of DC sputtering. Ionised plasma (Ar+) is accelerated towards the cathode target by an electric field. Bombardment of target by argon atoms results in the ejection of target atoms, which land on the substrate(85).

Standard DC sputtering uses glow discharge to ionise a neutral gas, commonly argon, producing Ar^+. The ionised gas is then accelerated by an electric field towards the donor material target mounted on a cathode. When the Ar^+ ion collides with the target, the transfer of momentum knocks particles free from the target. The ejected atoms travel across the sputtering chamber until they come into contact with a surface, such as a substrate, at which point they lose their kinetic energy and form a thin film.

As well as ejecting target atoms, the argon ions transfer their positive electric charge to the target. When using a conductive target, any positive charge is discharged through the target into the cathode, However, resistive targets such as silicon dioxide and BTFC cannot discharge through the cathode due to their insulative nature. As they are unable to discharge, positive charge begins to build upon the surface of the target. When the targets surface charge is equal and opposite to that of the cathode, then there is no net electric field to accelerate the argon ions towards the target. This prevents ion bombardment of the target and the deposition of thin film. This limits DC sputtering to conductive

targets, such as metals. This limitation can be overcome by using rf magnetron sputtering. A diagram of the rf magnetron sputtering apparatus is presented in figure 3.4(86).

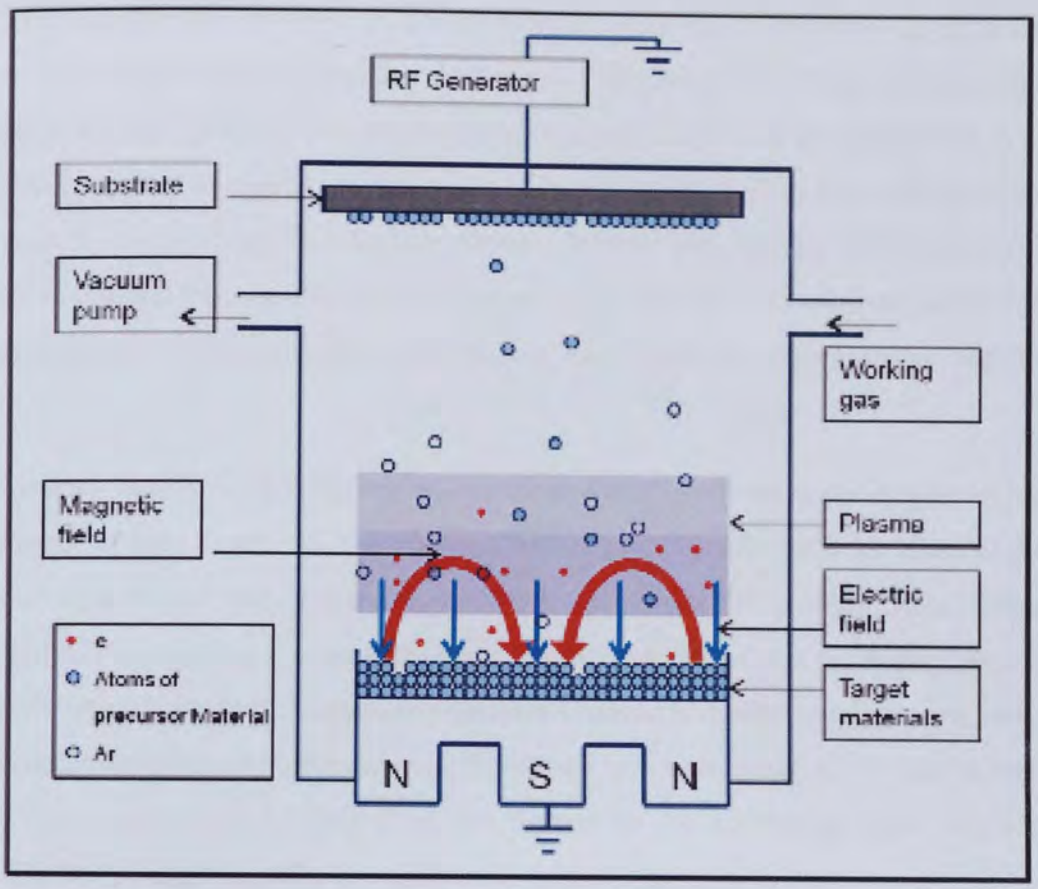

Figure 3-4 Schematic of rf magnetron sputtering. The radio frequency electric field accelerates charged electrons towards the target whilst in one voltage direction, and discharges the target during the opposing alignment. The magnetic field generated by the magnetron contain electrons near the target, increasing plasma generation rate(86).

Unlike DC sputtering, rf sputtering uses a radio frequency alternating current (AC) voltage (between 1MHz and 100MHz) to accelerate and build the kinetic energy of free electrons. The electrons are accelerated by the rf field, where they collide argon gas producing Ar^+ ions. In figure 3.4, (86) the Ar^+ ions are accelerated towards the target during the positive voltage cycle, where again they bombard the target, ejecting ions which travel across the sputtering chamber and form on the substrate. This, like in DC sputtering, results in the build-up of charge in the target. However, during the negative AC cycle, the charged ions are repelled, neutralising the charge on the target. This process repeats, causing charge to build up on the target during the positive cycle, and then discharged during the negative, preventing the build-up of a net charge across its surface.

This method allows for the continual sputtering of insulative and semiconducting targets, which would otherwise build up charge in a DC sputtering apparatus. As well as the RF- field generator, the process is assisted by a set of magnetrons located behind the target. The magnetic field of the magnetron

traps free electrons and plasma near the target. This process increases the rate of ionised argon atoms bombarding the target, improving the energy efficiency the sputtering rate of the target.

Rf magnetron sputtering is favorited for industrial applications due to its ability to use large targets, leading to large surface coverage and highly accurate deposition rates. This is advantageous in this investigation, as it allows for the deposition of thin films with a high level of repeatability, in which the thin film thickness and elemental composition remain consistent. The key disadvantage of sputtering derives from its dependence on solid bulk targets. Ceramic bulk targets, BTFC included, are very vulnerable to thermal shock due to their crystalline nature. The ion bombardment process generates a significant thermal energy upon the target surface, resulting in thermal expansion and cracking of the target.

Another disadvantage is that it is difficult to vary the thin film elemental contents without fabricating or purchasing a new target. In the combustion sol-gel(87) and chemical solution deposition method(88) the precursor materials can be varied with each deposition, making it easier to investigate the effect of different doping. Compared to rf magnetron sputtering, these techniques allow for faster investigation into the effect of dopants on thin films whereas in magnetron sputtering, any changes to the composition of the thin film requires fabrication of a new target, or the use of multi-target systems. This means that the thin films are limited to the sputtering target composition of $Bi_{3.25}La_{0.75}Ti_{2.5}Nb_{0.25}Fe_{0.125}Co_{0.125}O_{12}$ throughout this experiment.

3.2.2.1 Aston University's Magnetron Sputter.

Aston University's rf magnetron sputterwas utilised throughout this experiment to deposit BTFC and ZnO thin films from bulk targets. A picture of the sputtering apparatus itself is presented in figure 3.5.

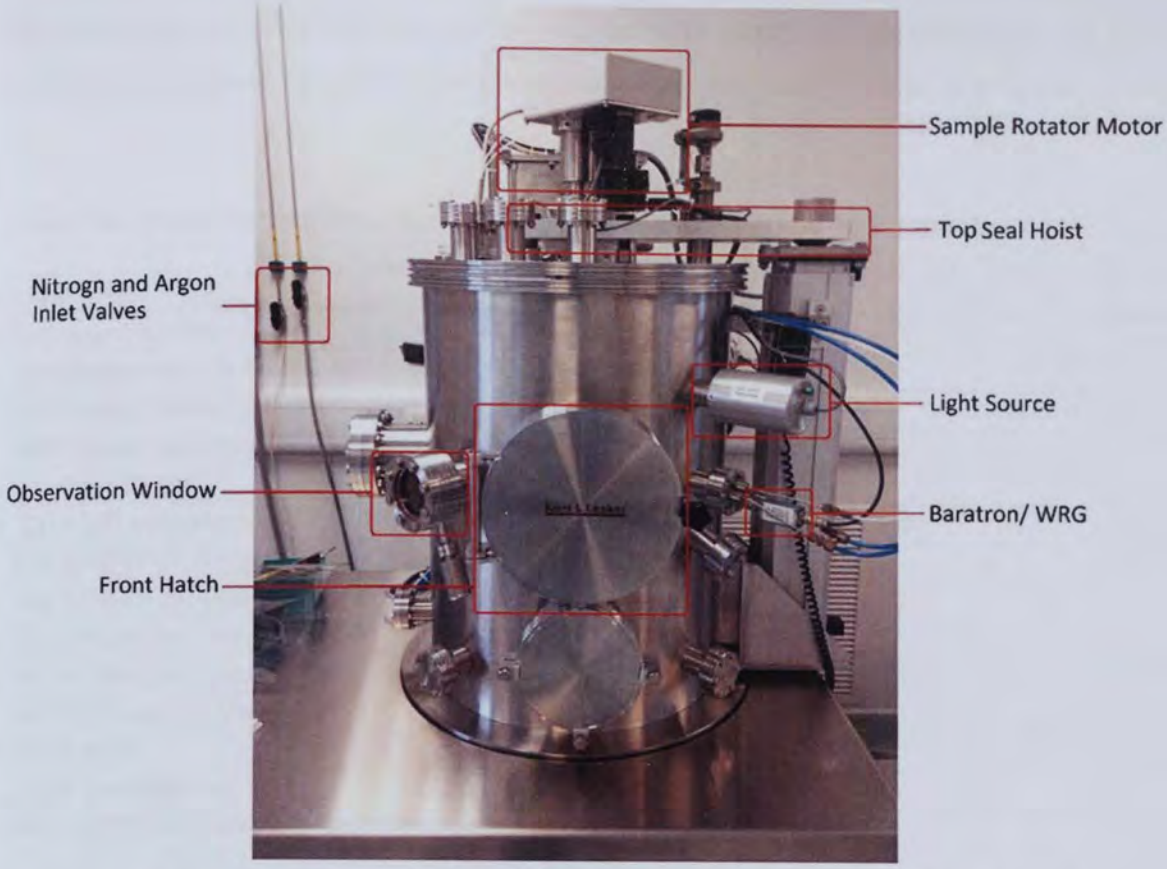

Figure 3-5 Front view of Aston Universities sputtering chamber, key parts have been labelled.

To achieve a high quality thin film, the chamber must be clear of any contaminate gasses prior and during sputtering. To achieve this, the procedure takes place in a single Kurt J. Lesker Vacuum chamber. The chamber has two entry points, a small front hatch for loading and removing samples, and a much larger lid, that can be removed using a hoist system. This is used for more complex processes such as changing the target and maintenance. The vacuum is generated via a two-stage pumping processes. Initially, a roughing pump is used at high pressures to bring the chamber down to low vacuum. Once a sufficient vacuum has been achieved, a cryo pump is activated to continue pumping the chamber. A base pressure of at least $1x10^{-5}$ Pa is achieved before sputtering, however, pressures as low as $6x10^{-6}$ Pa can be achieved depending on the pumping time. During sputtering, the valve connecting the cryopump to the chamber is set to a 'middle' position reducing the pumping rate so that a workable level of gas pressure can be achieved. With the cryopump set to the middle position, argon gas is released into the chamber via a mass flow controller. The mass flow controller allows for accurate chamber pressures by controlling the gas input rate against a fixed venting rate. The chamber pressure is measured using two different pressure gauges. A wide range gauge is used to measure the base pressure of the chamber, whilst a shorter range baratron is used to measure the pressure more accurately during sputtering.

The samples sit in a sample holder, 15cms away from the target. During deposition, the substrates are rotated at a rate of 10 rotations per minute, which ensures the deposition of an evenly coated thin film.

A list of the components used in the sputtering apparatus is presented in Table 1.

Unit	Type
Huttinger RF Generator	PFG 600 RF
Huttinnger Match Box	PFM 1500 A
MKS Mass Flow Controller	1179A 12CR15V
MKS Baratron Gauge	626 A01TCE
CTI Cryo Pump	8107807 G001
CTI 8200 compressor	8032550 G002
Ley Bold Wide Range Gauge	ITR90
Ley Bold Pirani Gauge	ITR90
Vat 3 Position Valve	64046-CE48
Lesker Roughing Valve	SA 0050 PUCF
Lesker Roughing Valve	SA 0150 PUCF
Linak Hoist	LP22A
Linak Transformer	CB08-1T-01-24

Table 1 Components used in Aston Universities RF magnetrons sputter.

Using Aston universities rf sputterer, high quality thin films have been produced, with controlled deposition rates, high repeatability, and high purity. However, it is limited by the fact that it cannot heat the substrates during deposition. BTFC thin films deposited by sputtering without substrate heating are amorphous in nature. This is true for BTFC deposited on platinum and other substrates, including IrO_2, Ir(74) and silicon(50). This is due to the crystalline nature of the Aurivillius phase requiring large amounts of thermal energy to form, requiring deposition at substrate temperatures typically above 500^{o}C(58, 89).

One alternative to substrate heating is the post deposition annealing of the as-deposited thin films. In this process, the film is removed from the chamber and annealed using a separate apparatus. Post deposition annealing allows for further control of the thin film properties by providing accurate temperature control, as well as variable annealing gas environment(90).

3.2.3 Thin Film Annealing

Annealing is the process of raising the temperature of a material to induce chemical and physical phase changes. In this experiment, annealing is used to crystallise amorphous as-deposited films into crystalline phases. This process was performed for both ZnO and BTFC thin films.

Annealing works by providing the atoms the thermal energy needed break existing chemical bonds and migrate within the solid material, moving them towards a more stable phase. In addition to

diffusing free atoms, the thermal energy breaks down existing bonds and phases that are not stable at the annealing temperature. Annealing temperature can influence the grain size in crystallite films, as larger grains tend to grow when they receive more thermal energy.

Annealing can be performed in a range of atmospheres, including vacuum, ambient, oxygen enriched and inert gasses. As well as affecting heat transference, atmospheric gasses can be absorbed into the thin film during annealing, for example, oxygen rich environments can reduce the oxygen vacancy in thin films. Vacuum and inert gasses can also be utilised when it is necessary to avoid oxidisation of samples, such as preventing rust in metals, or the formation of insulative silicon dioxide on semi conductive silicon substrate.

The annealing temperature can have a wide range effects on the crystallinity of BTFC thin films. Alfonso et al(58) investigated the effect of annealing temperature on $Bi_4Ti_3O_{12}$ thin films deposited on Si(100) substrates. The X-ray diffraction patterns of BTO thin films deposited on Si(100) substrates are presented in figure 3.6(58).

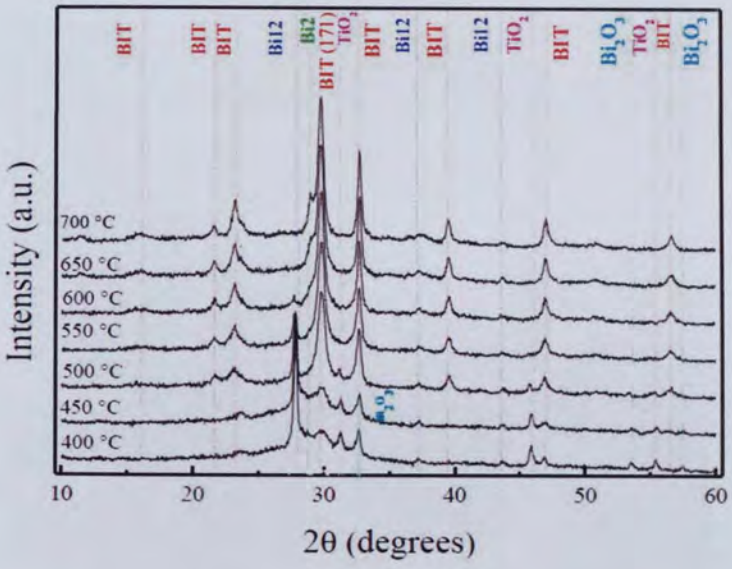

Figure 3-6 X-ray diffraction patterns of $Bi_4Ti_3O_{12}$ thin films deposited on Si(100) silicon substrates after annealing at various temperature using rf magnetron sputtering (58).

As seen in figure 3.6, In order for the amorphous as-deposited BTO to form the Aurivillius phase, it requires annealing at least 500°C, which has be demonstrated elsewhere(58). The Bi-deficient phase $Bi_2Ti_2O_7$ appears at temperatures above 600°C was also observe, which can be attributed to the emissions of volatile bismuth at high annealing temperatures. As the annealing temperature increases above 500°C the full width at half maximum(FWHM) decreases, indicating that the crystallite domain size is increasing as crystallinity improves(91). Wu et al(56) found that BTO presents the best

ferroelectric properties with the highest 2Pr when annealed at the curie temperature, with increasing temperature leading to decreasing polarisation and coercive fields.

The films deposited by RF sputtering without substrate heating in this experiment are amorphous as expected, and require thermal energy to form the necessary crystalline phase. In this experiment, post deposition annealing apparatuses is utilised for greater control over the annealing temperature and atmosphere. Two different apparatuses were used, a Carbolite CWF 11/23 ambient atmosphere and Siomm SGL-1700 for vacuum annealing. Both are now discussed in detail.

3.2.3.1 Carbolite CWF 11/23 ambient atmosphere furnace

To perform annealing in ambient atmospheric conditions, Aston University's Carbolite CWF 11/23 furnace was utilised, as presented in figure 3.7. The furnace utilises free radiating coils elements to generate thermal energy via joule heating. The two sets of coils are located either side of the chamber to help form a uniform temperature. Due to the difference between the furnace internal measured temperature and the samples true temperature, an external thermometer is utilised to gauge the temperature of the samples during annealing.

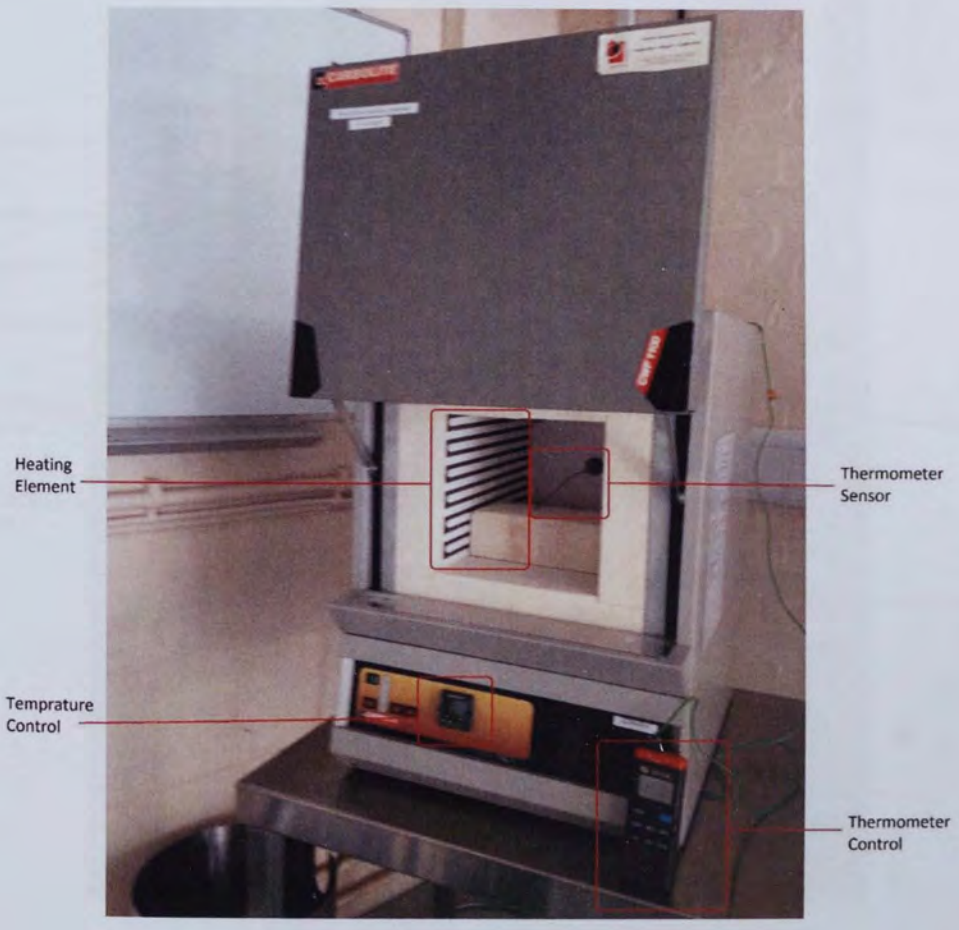

Figure 3-7 Astons Carbolite, CWF 11/23, Furnace.

To perform annealing, the furnace temperature is pre-set. Once the furnace has reached the desired temperature, the samples are placed in a ceramic boat, and loaded in, and later removed, using a pair of steel tongs for safety. During loading, the temperature will drop up to 150^{O}C, and then take approximately 10 minutes to reach within 5^{O}C of the original temperature. The annealing time is measured from this point as it is within the error of sensors accuracy, and as it takes up to 20 minutes to reach the full temperature. After the annealing period is over, the ceramic boat is removed and place on a ceramic brick to cool. To minimise contamination whilst cooling, another ceramic boat is placed on top of the ceramic boat holding the samples, with a small gap to allow air to circulate.

3.2.3.2 Vacuum Furnace

Annealing in an atmospheric vacuum is of interest to prevent the oxidisation of silicon substrates, and to measure the effect of oxygen vacancies in BTFC and ZnO thin films. For this purpose, Aston Universities' Siomm SGL-1700 is utilised, as seen in figure 3.8.

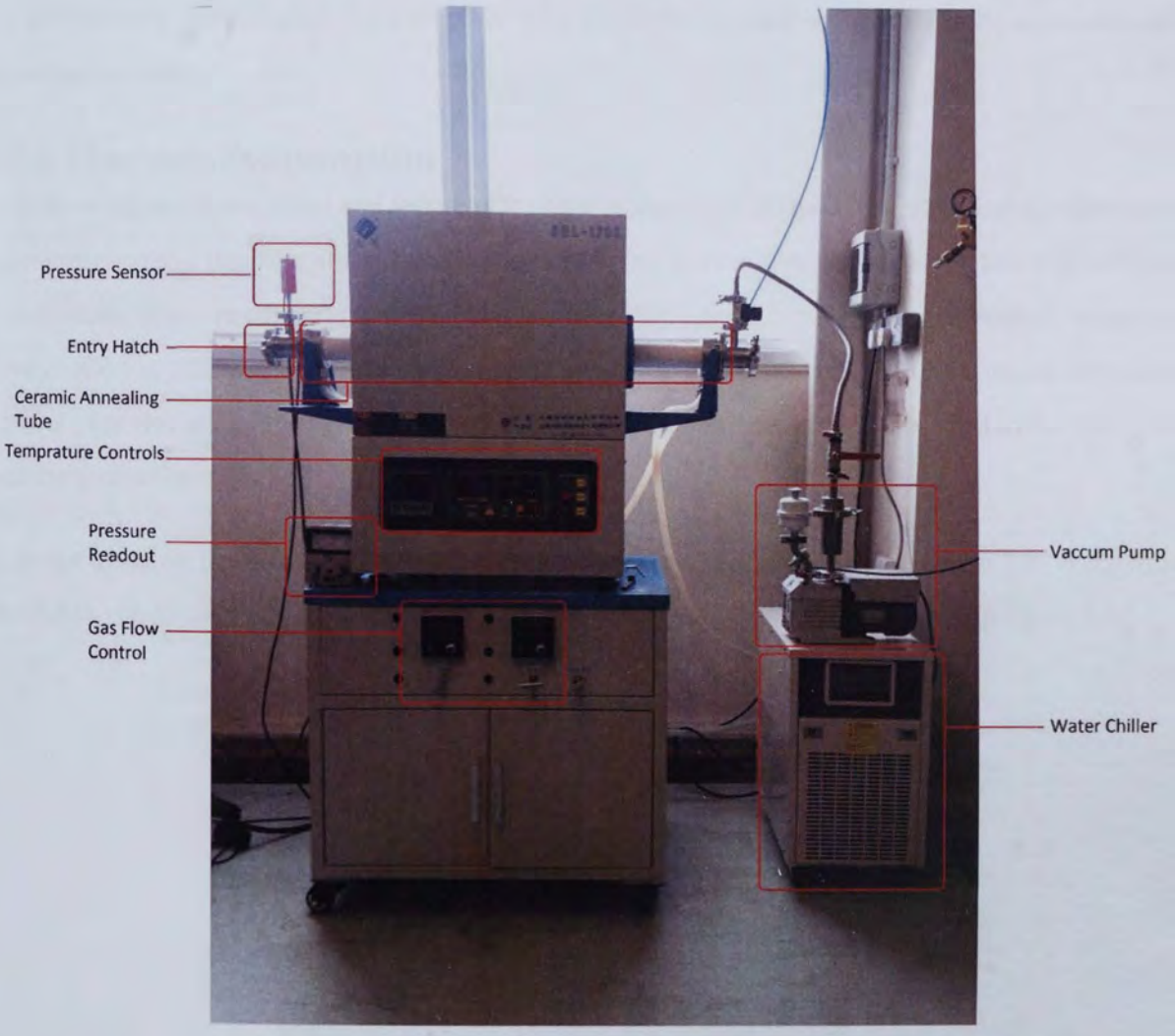

Figure 3-8 Aston Universities' Siomm SGL-1700 Vacuum furnace.

The samples were placed inside a ceramic boat, that is loaded intothe centre of the ceramic tube. The heating elements are located around the tube, giving it much greater temperature uniformity and accuracy than the Carbolite atmospheric furnace. A water chiller keeps the ends of the ceramic tube cool, allowing for greater temperature control and fast cooling rates. Either end of the tube is sealed with stainless steel hatched and O-rings, which can be opened for sample loading. The annealing can be performed under vacuum and inert gasses.

During annealing, a working vacuum of $1x10^{-3}$ Torr is generated before annealing. The temperature is controlled by a pre-scripted program, which allows the temperature to be set to certain values using specified ramping and cooling rates. After the annealing time has been reached, the heating element is turned off, and the annealing tube is left to cool naturally, assisted by the water cooling element. After the furnace reaches room temperature, the vacuum is broken, and the samples removed. As well as preventing the oxidisation of silicon, the Siomm SGL-1700 has significantly better temperature and atmosphere control than the Carbolite, CWF 11/23 furnace allowing films to be annealed with higher repeatability.

3.2.4 Thermal Evaporation

To perform accurate electrical and ferroelectric characterisation of thin films, electrical contacts were deposited onto the thin film and substrate surface. At the start of this investigation, this was achieved by depositing titanium contacts with tungsten carbide (WC) protection layers using Aston Universities rf magnetron sputteras described earlier. Later in this experiment, we utilised a newly purchased thermal evaporator for this task, due to its speed, ease of use and to minimise contamination in the sputtering chamber.

An image of Aston Universities Moor field thermal evaporator is presented in figure 3.9, and a more detailed image of the critical components located within the bell jar are presented in figure 3.10.

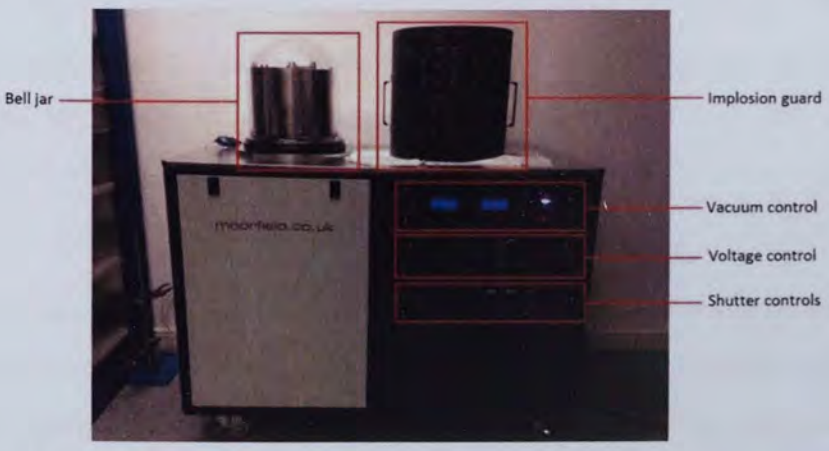

Figure 3-9 A picture of the outside of Aston University's Moorfield thermal evaporator

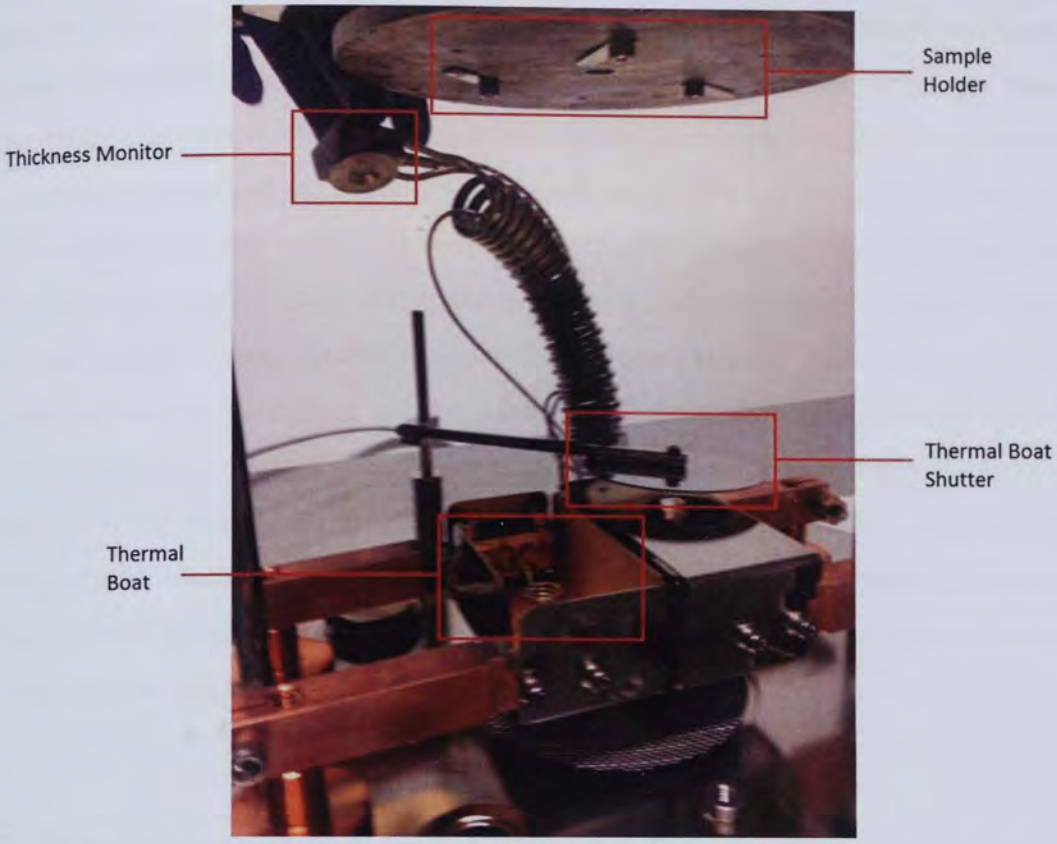

Figure 3-10 A picture of the inside the bell jar of Aston University's Moorfield thermal evaporator

Like rr sputtering, the evaporation process takes place in a low-pressure environment to minimise contamination from atmospheric gasses. The evaporation apparatus and low-pressure environment is contained within the bell jar, and generated by a Turbo pump. A minimal pressures of $3x10^{-6}$ Torr is achieved before evaporation is performed. To help minimise contamination, the boats were preheated at a temperature below the evaporating point of the material before each deposition. This preheating assists in ejecting any impurities absorbed into the chamber walls that would otherwise be emitted during material evaporation. During deposition, the film thickness was monitored by a quartz crystal film thickness monitor, and the deposition was patterned using conventional shadow masks. Only gold is used in evaporation in this work, which has a melting point of 1,064^{o}C. On average, gold evaporation begins when the voltage and power reaches 1.5V and 8W, however this varies slightly with material sample dimensions. All evaporation, however was done with a higher voltage and power of 2.5V and 44W in order to achieve a faster rate of deposition.

Whilst the rf-sputter was initially used to deposit tungsten carbide (WC) and titanium contacs in the early stages of this thesis. The Moor field evaporator was used later experiments after it was purchased, as it possesses several advantages. The key advantage is that by using a separate system for contact deposition, we could limit the usage of the rf sputtering to just BTFC and ZnO thin film

deposition, minimising contamination. Performing titanium and WC deposition leads to these materials contaminating the walls and target holder; this could lead to resputtering of these materials during BTFC deposition, leading to impurities embedding themselves in the thin films. By using thermal evaporation, the purity of the BTFC thin films could be significantly improved by limiting the use to the RF magnetron sputter to just that material. Another key advantage of thermal evaporation is that it can evaporate materials using smaller material samples, whilst rf magnetron sputtering is limited to large bulk targets, making sputtering expensive materials such as gold or platinum unaffordable. Thermal evaporation, by contrast can work with very small samples, typically in the form of millimetre thick wire, or pellets, making it affordable to work with precious materials like gold. Lastly, the thermal evaporator is significantly faster than the RF sputter, due to the smaller vacuum chamber size. Whereas the RF sputter requires 5 hours to produce a workable atmosphere, the evaporator can achieve a similar atmosphere in only 1 hour, which typically allows the deposition to be performed on the same day the thin film was deposited.

3.3 Characterisation and Analysis Apparatus

The discussion in this chapter so far has been concerned with the fabrication methods involved in developing the thin film and capacitor structures needed to examine the properties of BTFC thin films. This section will focus and discuss in detail the characterisation techniques used throughout this thesis in order to examined these fabricated samples.

3.3.1 X-Ray Powder Diffraction

X-ray crystallography, commonly referred to as X-Ray powder diffraction (XRD) is a crystal structure analysis technique that uses the diffraction of an x-ray beam to map the molecular structure of a crystal. In this experimentation, we use XRD to determine the phase and orientation of deposited thin films.

XRD uses the constructive interference between monochromatic-rays and the samples crystal lattice to produce a 3D image. The X-rays are generated using cathode tube, and filtered to produce a monochromatic beam. When the beam satisfies Braggs law, $n\lambda = 2d\sin\theta$, the beam undergoes constructive interference, increasing the intensity of the return beam detected by a sensor. Bragg's law is defined as

Where

n = an integer (usually 1)

λ = X-ray wavelength.

d = d-spacing, distance between planes

θ = Bragg angle (incident angle)

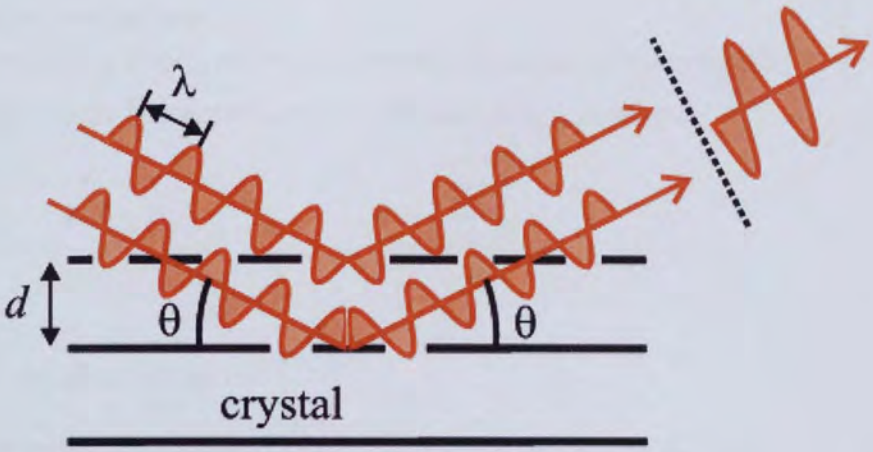

Figure 3-11 Braggs Law, X-rays of wavelength λ, experience maximum constructive interference when the condition, nλ=2dsinθ, is met, where d is the separation of crystal planes and θ is the angle of incident(92).

Figure 3.11 demonstrates Bragg's law. Bragg's law determines the condition based on the crystal plane separation, d, and angle of incident, θ, at which X-rays of wavelength λ will undergo maximum constructive interference. When the incident angle vs X-rays intensities is plotted on a X-Y graph they form a diffraction pattern. The diffraction pattern of each mineral and crystal is unique, allowing the identification of experimental samples by referencing against known databases.

XRD instrumentation consists of three vital parts. An x-ray tube, the sample holder, and the detector (93). A cathode tube ray is used to generate X-rays, it achieves this by bombarding a target material (typically Cu, Fe, Mo, Cr) with electrons. When the electrons dislodge electrons from the inner shells of the target material atoms, they emit x-rays characteristic of the material. The spectra of x-rays emitted consists of multiple components, Kα and Kβ being the most common. The emitted x-rays are then monochromised by filtering or crystal monochrometers. During measurements, the emitter and detector are rotated over the desired range of angles. The detector counts the intensity of emitted x-rays and converts into accounts per second at specific angles of incident. In this thesis, two separate

instruments were used, initially, Queens Mary University London's Bruker d8 with CuKa1 radiation with wavelength 1.57 Å was utilised, but Aston University's X'PERT-PRO using Cu Kα radiation with a wavelength of 1.54 Å was in the later stages of this investigation due to the easier access.

In this study, XRD is used to characterise the crystallinity of BTFC thin films and ZnO interface layers. This technique allows us to confirm that the possessed BTFC thin films are Aurivillius in phase, and to determine if any secondary or amorphous phases are present.

3.3.1.1 Scherrer equation

The sheerer equation is a formula that allows the calculation of the crystallite domain size from the line broadening in X-ray diffraction patterns. The equation is defined as

$$\tau = \frac{K\lambda}{\beta cos\Theta}$$

Where

τ = the size of crystallite domains.

K = is the shape factor, with a value close to 1. It is taken as 0.9 in this thesis

λ = X-ray wavelength

β = the line broadening, full-width at half maximum (FWHM), of the investigated peak in radians.

Θ = Bragg angle

The value of β, is calculated by taking the top and bottom half maximum values, calculating the difference in degrees (keeping the angle in 2-theta), then converting the value into radians. The Bragg angle, however, is kept in degrees with the 2Θ value presented in the diffraction pattern converted into Θ. Using the sheerer equation, it is possible to determine the crystallite size of domains within the analysed thin films. Thin films are typically polycrystalline, consisting of multiple grains; however, each grain consists of multiple single crystal crystallite domains. By using the sheerer equation, we can determine the size of these domains. One notable limitation of the Scherrer equation, however, is that it does not consider changes in the tensile stress of the thin film. Increasing tensile stress results in peak shifts to higher Bragg angles, a result of the d spacing is reduced as the lattice is compressed. In this thesis, the Scherrer equation is utilised to calculate the crystallite domain size in BTFC and ZnO thin films, to investigate the effect of deposition and annealing conditions on crystallinity.

3.3.2 Scanning Electron Microscopy

Scanning electron Microscopy (SEM) is a surface analysis technique that investigates the surface topology of samples by scanning them with a beam of high energy elections. The electrons reflected from the sample surface are detected by a sensor, which is then used to produce an image of the samples surface. This provide information regarding the grain size, orientation and roughness. In this experiment, SEM is utilised to investigate the surface morphology of thin films and to determine the cross-sectional thickness so that the deposition rate can be calculated accurately.

Figure 3.12 demonstrates the SEM apparatus. Electrons are generated by an electron gun at the top of the apparatus after which they are accelerated and focused into a single beam. The direction of the beam is controlled by a set of scanning coils above the objective lens, which is used to scan the beam across the surface of the sample. As the beam scans over a defined area of the sample, the detectors collect information regarding X-Rays, backscattered electrons and secondary electrons, to build a picture of the surface of the sample. To help eliminate interference of the electron beam, the process is performed in a vacuum chamber.

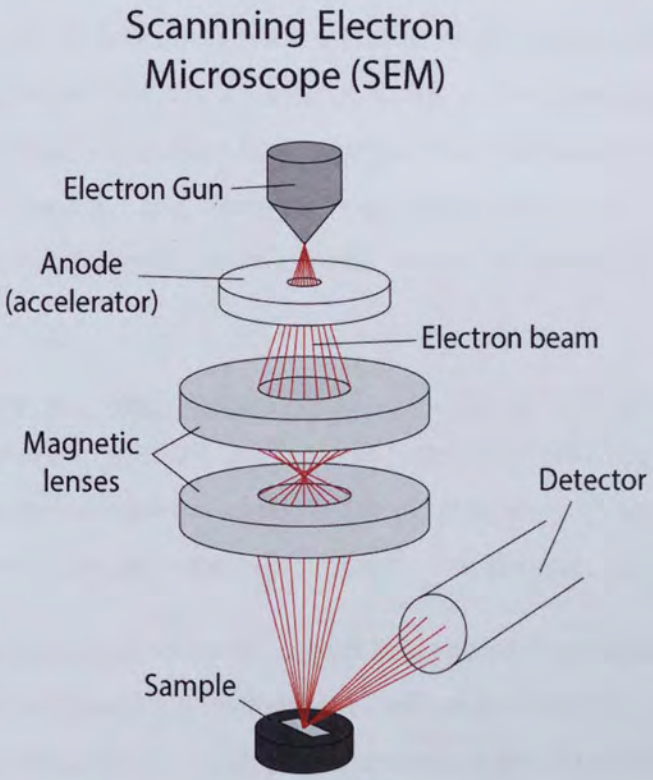

Figure 3-12 Schematic of the SEM apparatus(94).

The electron beam penetrates the sample to a depth of a few micrometres depending on the sample density and the accelerating voltage(95). The signal generated by the sample consists of primary

electrons, secondary electrons, back scattered electrons and x-rays. These signals are collected by one or more detectors, and used to produce an image of the surface of the sample at a high spatial resolution. The backscattered electrons can be used to determine the elemental composition of the film, as the intensity of the backscattered electrons is proportional to the atomic number of the compositional atoms. X-ray emitted from the sample can be collected and used in Energy Dispersive X-Ray spectroscopy (EDS), which provides qualitative and quantitative elemental analysis.

A standard SEM has a magnification range of between 10 to 50,000X for conductive samples (17). For non-conductive samples, a conductive coating, typically gold, is applied in order to avoid charging defects. High magnifications in the range of 100,000-1,000,000X can be achieved using field emission scanning electron microscopy.

In this project, SEM is used for two different purposes. Firstly, it is used for surface analysis wherein the thin films surface morphology and roughness is investigated. It is known that the surface roughness of thin films is proportional to grain size(96). Grain size has been demonstrated to affect the leakage and ferroelectric properties of thin films. SEM images can therefore be utilised in explaining the variation in electrical properties, surface roughness and grain size with annealing temperature. Secondly, SEM is utilised in cross sectional measurements to determine thin film thickness to calculate deposition rates. Cross-sectional measurements were performed by cutting the thin films in half and measuring the thin films cross sectional area. This allows us to visually distinguish the thin film/substrate regions, and measure the thicknesses using pixel measurements. Measurements were taken from the centre of samples, where no shadowing effect from the mask during deposition occurred.

3.3.3 Energy Dispersive Spectroscopy

Energy dispersive X-ray spectroscopy (EDS), is an analysis technique were a beam of charged particles, is used to excite the emission of x-rays from a sample. The resulting emission spectrum is characteristic of the chemical makeup of the sample, allowing for quantitative elemental characterisation.

To excite the sample, a beam of charged particles, such as electrons or photons, is used to radiate the sample. These particles excite electrons in the inner shells of the atoms orbits, resulting in the emission of the electron. When the electron is emitted, an electron hole is left in the inner ring. In response to this, an electron in a higher energy state in an out ring will drop to into this electron hole. As it drops to a lower energy state, it emits energy in the form of an x-ray, which possesses energy and wavelength characteristic of the difference in energy levels. A diagram of this process is presented in figure 3.13.

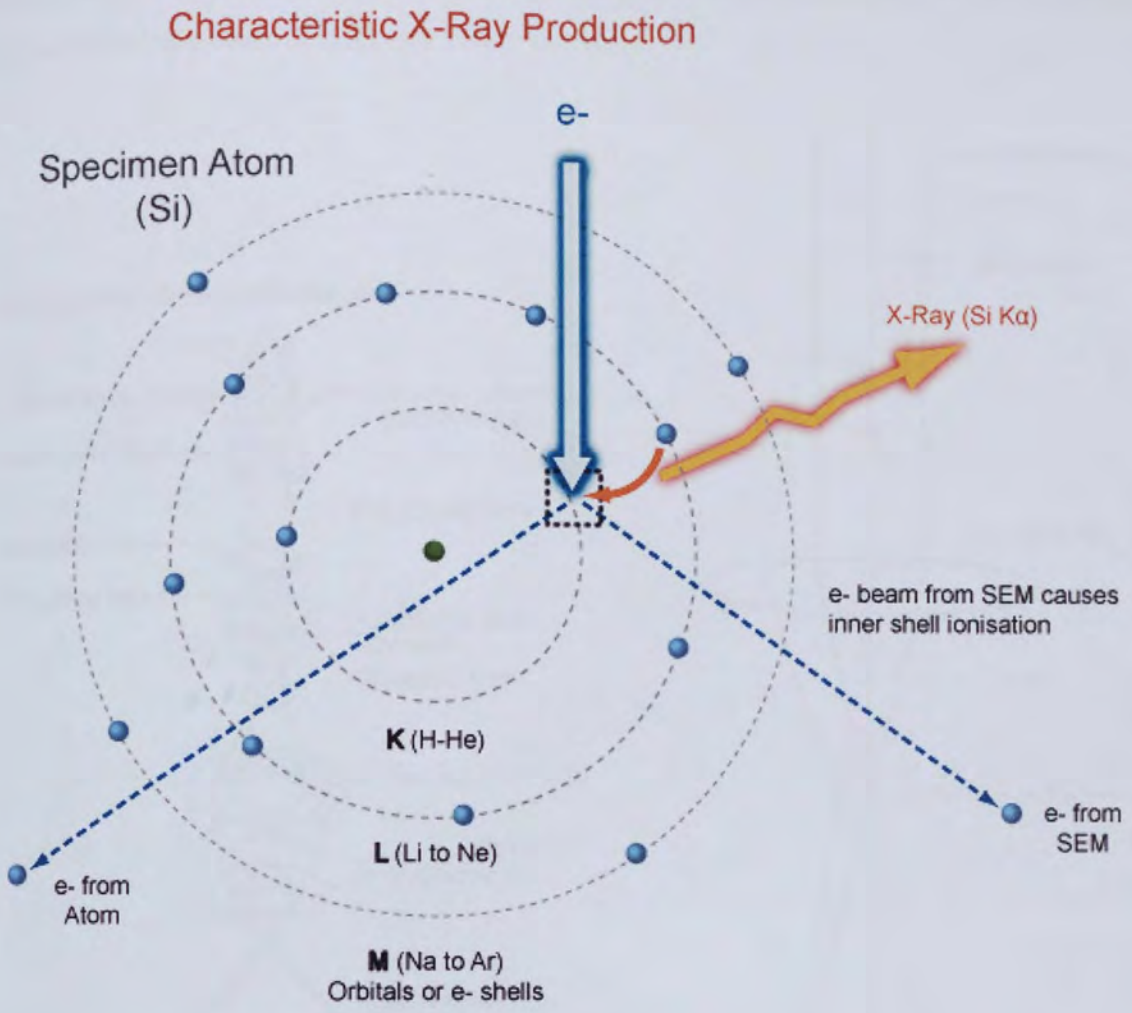

Figure 3-13 The process of electron emission in EDS for a silicon atom. The incident electron removes an electron from the inner K ring, resulting in the emission of the two electrons and the generation of an electron hole. An electron in the L orbital drops then into the electron hole, emitting x-ray radiation characteristic of silicon in the process(97).

As the wavelength of the x-rays is characteristic of each element, analysis of the x-ray wavelength and quantity allows the characterisation of the samples elemental content and quantities. EDS is employed in the field of ferroelectric to confirm the chemical composition of thin films and ceramics(98-100). In this investigation, EDS is used to confirm the insertion of La, Nd, Fe and Co dopants into the BTFC thin films, and to characterise their quantities.

3.3.4 Transmission Electron Microscopy

Transmission electron spectroscopy (TEM) is a spectroscopy technique in which a focused beam of electrons is passed through an ultrathin sample. As the electron beam passes through the sample, it interacts with it, producing a pattern that reflects features internal structures such as grain shapes

and boundaries. A TEM operates in the same way that a light microscope does, however, it improves upon it but utilising a beam of electrons, rather than light.

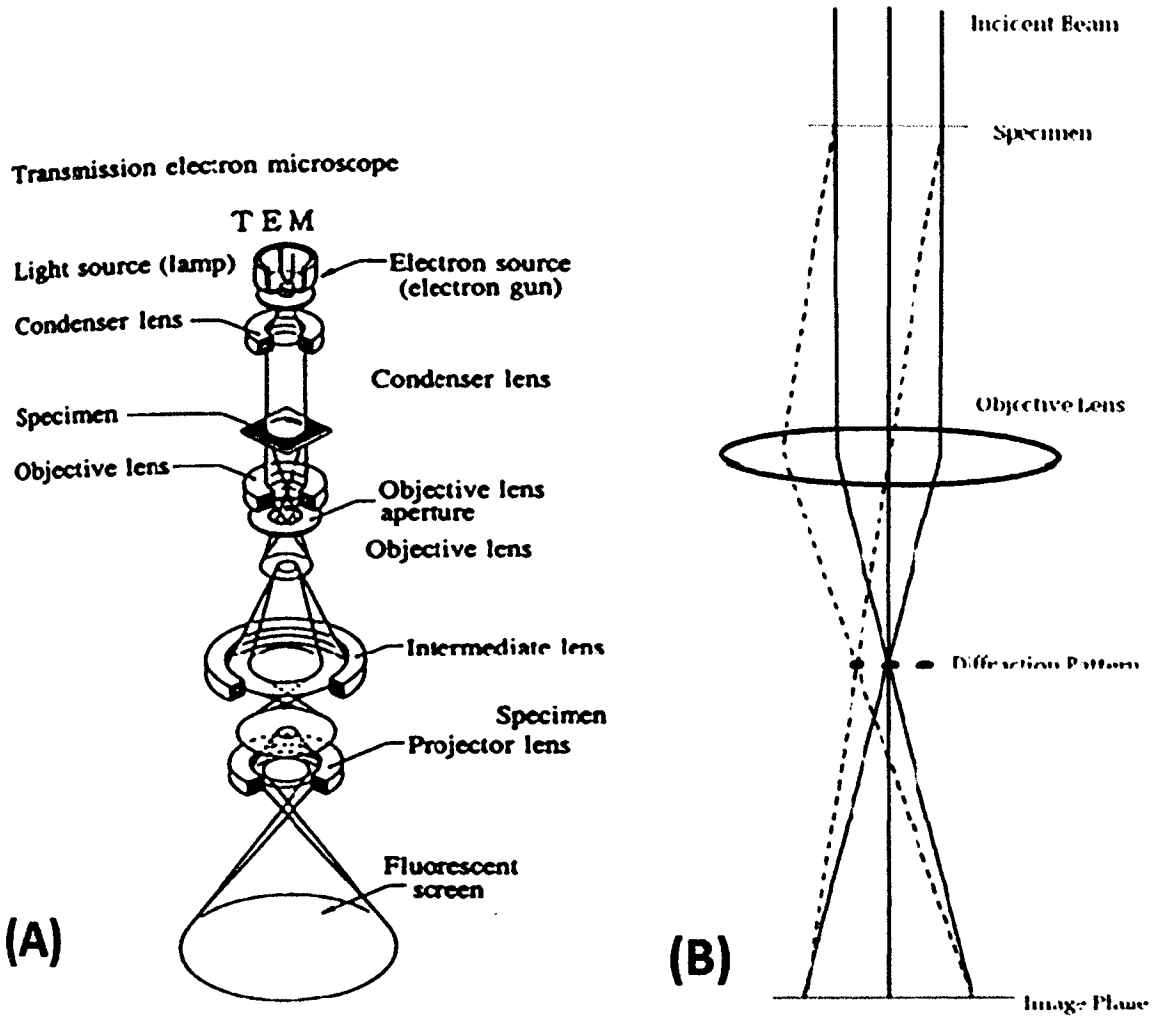

Figure 3-14 (A) schematic of TEM apparatus, (B) diagram of electrons diffracted by specimen being focused onto imaging plane (101).

A schematic of the TEM is presented in figure 3.14. A beam of electrons produced by the electron gun is focused into a single beam by a set of condenser lens. The beam is then incident on the sample where the electrons interact with the sample in various ways, including reflection and refraction. The electrons that pass through the sample are then collected by an objective lens. The lens focuses and enlarges the image onto an imaging device. This device may consist of a phosphor screen, or in a more modern system, a charge coupled device camera.

TEM is utilized in this investigation to analyse the crystal structure of BTFC thin films. In order to analyse the cross sectional area, the samples were cut perpendicularly to form an ultra-thin film by a focused Ion Beam, allowing for the electron beam to be incident upon the cross sectional area.

High resolution transmission electron microscopy (HRTEM) is a mode of TEM. In this mode, a large objective lens is used to collect a wider range of diffracted beams. These widely diffracted beams allow TEM to determine the exact position of specific atom columns. Using HRTEM, atomic column of planes can be accurately detected, making it a useful tool for analysing grain boundaries, interfaces between different materials, and the d-spacing of crystalline planes.

In this investigation, TEM is used to analyse in detail the grain boundaries of the cross sectional TEM samples. It allows us to analyse the interface between them, and by utilising HRTEM, to look at the exact crystallographic structure at the interfaces, in a way that cannot be achieved using XRD, or with the smaller resolution of SEM. All TEM data collection was performed by staff at the National Institute for Material Science of Japan.

3.3.5 Magnetometer - Superconducting Quantum User Interface Device

Superconducting Quantum User Interface Device (SQUID) magnetometers are highly sensitive apparatus used to measure the magnetic moment of samples. They are utilised in this investigation to characterise the ferromagnetic properties of BTFC thin films.

In SQUID magnetometry, as demonstrated in figure 3.15 the sample is attached to a non-magnetic actuator, which is placed inside of a fixed magnetic field generated by superconducting electromagnets. When the sample holder vertically oscillates a magnetic sample, the samples movement will induce a change within the magnetic flux of the chamber proportional to the samples total magnetic moment. These changes in magnetic flux will induce changes in the current of superconducting wires, which act as pick up coils.

The super conducting wire forms a closed loop with the SQUID, which converts any change in current to an output voltage. The SQUID in effect works as a highly sensitive current to voltage converter, allowing the samples magnetic moment to be characterised by the level of voltage detected by the SQUID.

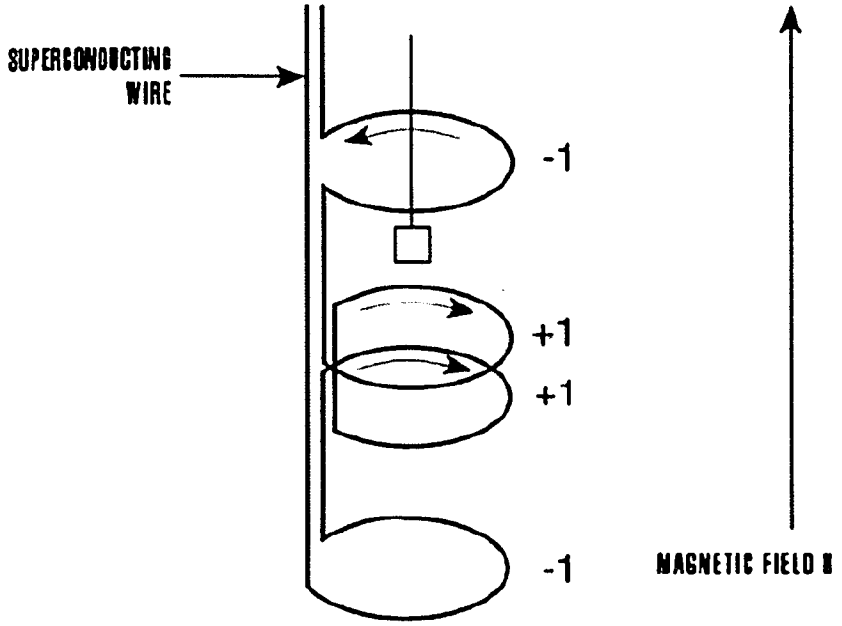

Figure 3-15 diagram of SQUID magnetometer. The sample is oscillated within magnetic field H, which induces a change in the magnetic flux inside the chamber depending on the samples magnetic moment. This in turn leads to a change in current of the through the superconducting wires(102).

Unlike ferroelectric measurements, where the thin film nature makes characterisation easy due to the small driving voltage necessary to generate a ferroelectric response. The samples thin film nature makes ferromagnetic characterisation difficult due to several factors. The leading problem is that the small volume of thin film samples make the resulting magnetic moment extremely small compared to bulk samples. It is reported that bulk BTO doped with Iron and cobalt have magnetic moment of 7.8memu/g (68, 69). Using the reported density of 9.10g/cm^3(103), we can calculate that the total remnant magnetisation for a 400nm thick thin film with a surface area of 1cm^2 to be:

Volume = 400nm x 1cm x 1cm = $4x10^{-5}cm^3$.

Total mass = $4x10^{-5}cm^3$ x 9.10g/cm^3 = $3.64x10^{-4}g$

Total magnetisation = 3.64 x 10^{-4}g x 7.8memu/g = $28.4x10^{-6}$emu

Because of the thin films incredibly small mass, the remnant magnetisation is expecting to be in the region of 10^{-6} emu. Magnetisations of the size are out of the sensitivity ranges of most conventional Vibrating sample magnetometers (VSM)(104, 105). In order to accurately gauge the samples magnetisation, a SQUID Magnetometer must be employed, as they are capable of measuring the magnetic moment to such a deep of sensitivity(106).

The Ferromagnetic properties of doped BTFC thin films were characterised using Warwick University's Quantum Design MPMS-S5 SQUID Magnetometer, all measurements were performed at 5K.

3.3.6 X-Ray Photoelectron Spectroscopy

X-Ray photoelectron spectroscopy (XPS) is a surface characterisation technique used to determine sample elemental compositions and chemical states. XPS is performed by targeting the sample with a beam of X-rays, with the intensity and energy of the resulting emitted electrons providing information regarding sample elemental composition. Like SEM, XPS is performed at a high vacuum, to prevent interference from atmospheric gasses.

The process by which photoelectrons are emitted is presented in figure 3.16, When X-rays are incident with the sample, photoelectrons are emitted from different energy levels. The energy of the photoelectron can be determined using the equation:

$E_b = HV - E_{kin} - W_f$

Where

E_b = Electron binding energy

HV = Energy of the incident X-Ray

E_{kin} = Kinetic energy of emitted electrons

W_f = The work function of the spectrometer

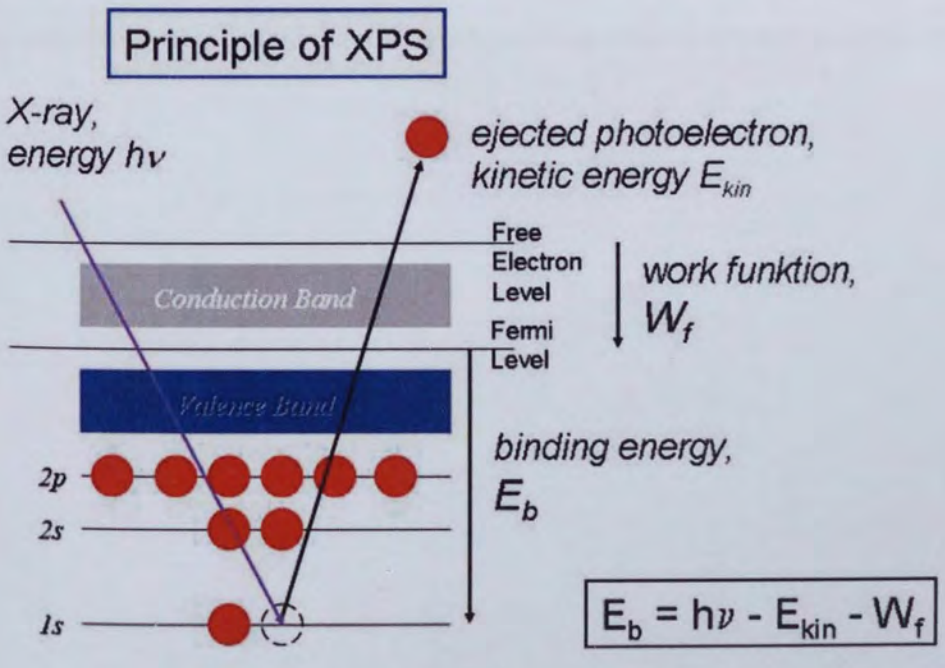

Figure 3-16 The process of electron emission in XPS (107).

The energy of electrons ejected by X-ray interaction is used to plot a XPS spectrum, which consists of the intensity on the Y-axis and electron binding energy along the X-axis. The specific binding energy of the peaks is characteristic of the electron configuration of specific elements eg 1S 2S, 2P etc. Thus, it is possible to determine the elemental composition of sample surfaces by comparing the peak binding energy of the spectra to the known binding energy of each element. Furthermore, by comparing the intensity of the peaks, it is possible to determine the quantities and elemental information of the film.

In addition to elemental composition, XPS is able to determine the chemical states of the sample. This is possible as the binding energy of electrons varies with the oxidation state, allowing us to determine the bounding state by measuring the shift in peak locations. As well as using XPS to confirm the elemental composition of the BTFC thin films, we can utilise the chemical shifts to detect if any undesirable metallic clusters have formed in the thin film, or if only the desired oxidisation states have formed.

3.3.7 Ferroelectric Tester

Ferroelectric materials are defined by their non-zero spontaneous polarisation, which can be switched by the application of an electric field. This non-zero polarisation is usually presented in the form of a hysteresis curve, which ferroelectric polarisation (P) on the Y-axis, and electric field (E) or applied voltage(V) on the X-Axis. A detailed explanation the phenomena of ferroelectric hysteresis can be found in the previous chapter 2.3.1. In this investigation, to characterise the P-E hysteresis loop of BTFC thin film samples, the triangular voltage waveform is utilised method. A schematic of the measuring apparatus utilised in this experiment to achieve these measurements is presented in figure 3.17.

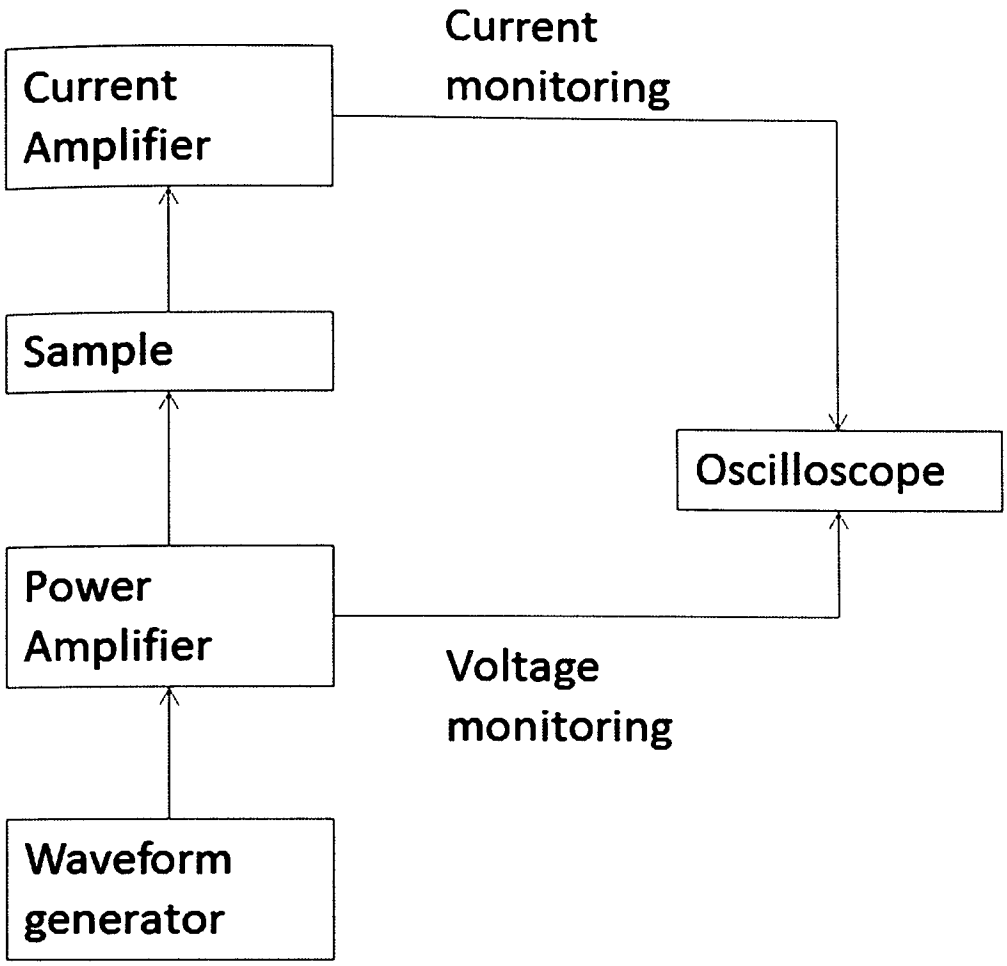

Figure 3-17 Schematic of the ferroelectric testing apparatus

The apparatus used in this experimentation is a combination of a Hewlett 33120A Waveform generator, a Trek601C Power Amplifier, a Keithley428 Current Amplifier and an Agilent 54624A oscilloscope. These are presented in figure 3.17. The waveform generator produces triangular voltage waveform in the frequency range of 10Hz to 1KHz. As the waveform generator cannot produce sufficient voltage, the output voltage is then multiplied by a factor of 100 by a power amplifier. The amplified triangular waveform is applied to the sample using a conventional probing station. The output current is amplified to a readable level by a current amplifier, which is then measured and recorded using an external oscilloscope.

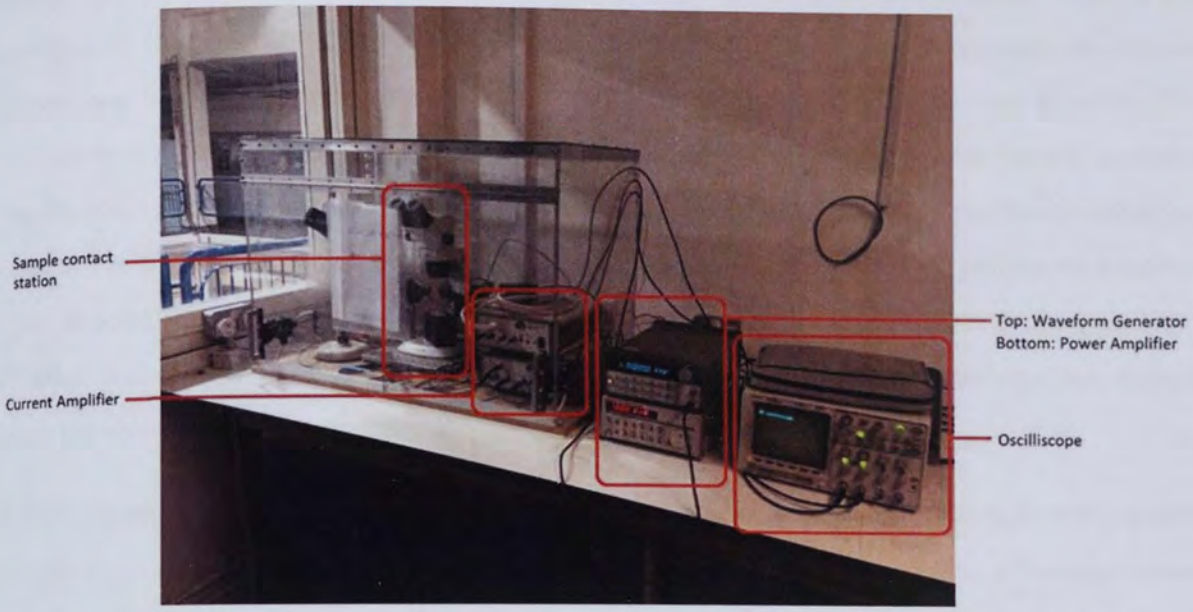

Figure 3-18 A picture of the apparatus used in the ferroelectric measurements performed in this investigation

Using this method, Yan et al(108) investigated the electric displacement - electric field (D-E) loops ferroelectric $Na_{0.5}K_{0.5}NbO_3$ (NKN), as demonstrated in figure 3.19.

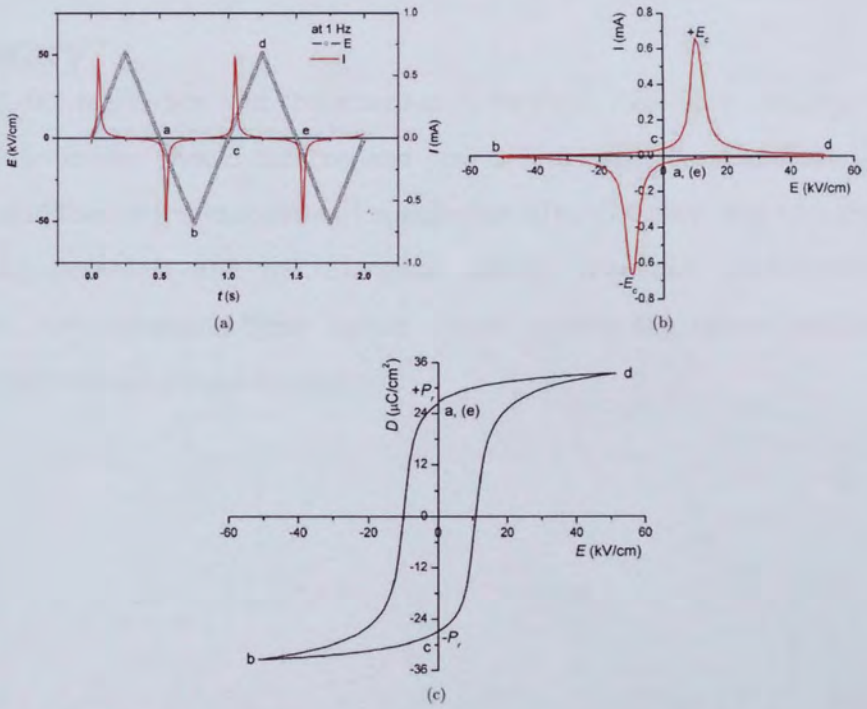

Figure 3-19 The ferroelectric analysis of NKN performed measured at 1Hz and 25°C, Electric Field and Current Vs Time, Current Vs Electric field for a single voltage cycle, Electrical Displacement Vs Electrical Field Loop (108).

Figure 3.19. (a)(108) demonstrates the applied triangular voltage and current response over time. As seen between point's c and d, the current peaks leads the voltage peak. The current peak leading the voltage peak is evidence of ferroelectric behaviour, as current in a ferroelectric capacitor is due to it charging/discharging as the ferroelectric dipoles change direction around the coercive field. As the

current at the maximum applied field is extremely low, we can also conclude that there is little contribution from leakage current or dielectric contributions. Figure 3.19.b presents the current-voltage loop for a single voltage cycle. Each current peak location indicates the each location of the coercive field in each switching cycle. Figure 3.19.c presents the same plot with current converted into electrical displacement, to form a D-E hysteresis loop. The loop presents a hysteresis behaviour, with clear remnant polarisation and coercive field points. Once the electric field reaches its maximum value at point D, the electrical displacement begins to drop as the electric field is reduced. This is evidence that we have a fully saturated ferroelectric, as charge no longer accumulates, but depletes when the voltage direction changes

In most literature, ferroelectric hysteresis loops are presented as ferroelectric polarisation (P) - electric field (E) loops (109, 110). This is inaccurate, as the measured polarisation consists of leakage current and dielectric contributions, as well as ferroelectric ones. In this thesis, the ferroelectricity effect of BTFC thin films will be reported as electric displacement (D)- electric field (E) as the discussion will include additional information regarding the leakage current and dielectric contributions to the calculation of the remnant polarisation.

3.4 Summary

In this chapter, the fabrication and characterisation methods have been presented and discussed. After reading, the reader should comprehend how SPS, RF-magnetron sputtering, annealing and evaporation are utilised in the formation of multiferroic BTFC thin films, and how and why SEM, XPS, TEM, EDS Magnetometers and the triangular voltage waveform methodology are used in characterisation. Understanding these factors should provide the reader with the capability in understanding the following experimentation.

Chapter 4 : The Integration of BTFC Thin Films on Silicon Substrates Using ZnO Interface Layers

4.1 Introduction

The Aurivillius phase material, bismuth titanate oxide, has been frequently studied for applications in the field of FeRAM, due to its low coercive field, high electric resistivity and fatigue resistant properties along the C-axis(58, 59, 111). The properties of BTO can be improved and tuned by substituting different ions into existing bismuth and titanium sites (112, 113). Recently, there has been growing interest in the insertion of iron and cobalt ions into B-site locations to induce ferromagnetism, which is an emerging approach in producing novel single phase magnetoelectric materials for use in novel data storage devices(68, 69, 114).

Investigations into $Bi_4Ti_3O_{12}$ thin films are typically performed using platinum coated silicon substrates (66, 112, 115). This is due to platinum's ability to retain its electrical conductivity and smoothness when annealed at the high processing temperatures needed to form Aurivillius phase BTO thin films, whilst other substrates go through oxidisation or thermal expansion during the same annealing process.

Platinised silicon, however is extremely expensive, with 10cm diameter wafers costing typically up to £300. Therefore, it is beneficial to look for alternative substrates. The deposition of ferroelectric thin films directly on silicon is impaired by diffusion of ferroelectric constituent elements from the thin film into the silicon substrate(75). To improve the growth of ferroelectric thin films on silicon substrates, interface layers, also known as buffer layers, can be inserted between the ferroelectric thin film and silicon substrates (116, 117). Interface layers are thin films that are sandwiched between the ferroelectric and substrate, which can improve the crystalline properties of the thin films in two ways. Firstly, they act as a diffusion barrier, preventing atoms diffusing between the substrate and thin film, and secondly, they can act to improve the crystallinity of the thin films, by changing the surface it is deposited upon.

In memory device applications, one of the key device structures is the metal-ferroelectric-semiconductor(MFS) device structure. With this device structure, it is not only desirable that the interface layer acts to improve the crystallinity of the ferroelectric, but also functions as a semiconductor channel(118). Zinc Oxide (ZnO) is an excellent semiconductor due to its wide bandgap, nontoxicity, affordability and abundance, whilst possessing chemically and thermal

stability under the plasma processes and high temperatures(119). There is therefore interest in the integration of doped BTO thin films on ZnO interface layers to improve the crystal quality of BTO, and to study the feasibility of a BTO/ZnO MFS device.

The aim of this study is to investigate the growth and crystallinity of doped-BTO, $Bi_{3.25}La_{0.75}Ti_{2.5}Nb_{0.25}Fe_{0.125}Co_{0.125}O_{12}$(BTFC) thin films with novel Fe, Co, Nb and La dopants on P-type silicon substrates using ZnO interface layers. The effects of the dopants, annealing temperature and pre-treatment of the ZnO interface layer on the crystallography structure and surface morphology of BTFC are investigated by XRD, SEM and TEM. Elemental diffusion of BTFC constituent elements between the ferroelectric layer and the substrate and across the interface layer are investigated by HRTEM. The chemical composition of the BTFC thin films is investigated by XPS and EDS.

4.2 Experimental

In this study, 500 micrometre thick P-type (111) silicon substrates were used. The substrate was cut into 1.5cm by 1.5 cm pieces, followed by cleaning and degreasing before deposition. This was achieved by sonicating them in acetone for 30 minutes, followed by rinsing with deionised water and blow-drying with nitrogen gas. This process was then repeated using isopropanol instead of acetone. Finally, the samples were sonicated for 5 minutes and rinsed with deionised water, followed by blow-drying with nitrogen. The samples were then immediately loaded into the rf sputter chamber to minimise contamination. The chamber was set to pump for at least 8 hours, achieving a base pressure of at least 1x 10^{-7}mBar. Sample cleaning and RF-sputtering was performed in clean room environment to minimise contamination during handling.

Thin films were sputtered from a $Bi_{3.25}La_{0.75}Ti_{2.5}Nb_{0.25}Fe_{0.125}Co_{0.125}O_{12}$ (BTFC) target, the fabrication of which was described in chapter 3.2.1.1. At the beginning of the sputtering procedure, the sample shutter was closed to eliminate deposition during the plasma ramping process. To minimise damage from thermal shock to the BTFC target, plasma ignition was achieved with a power of 20 W, a working argon gas pressure of 4.9 Pa (flow rate = 60 SCCM) and with the target shutter remaining closed to help contain plasma near the target. The power was ramped up to a working power of 150 W at a rate of 1W every 10 seconds. When the target power was achieved, Ar gas pressure was dropped to 1 Pa (flow rate = 14 S.C.C.M)

and the target shutter was opened. With the set plasma sputtering conditions achieved, the conditions were maintained for 10 minutes to ensure any surface contamination on the target was sputtered off prior to deposition. After ten minutes, the substrate shutter was opened, allowing the deposition to begin. ZnO thin films were deposited using the same methodology, however, a higher power and ramping rate of 300 W and 1 W/S were utilised due to the targets resistance to thermal shock. BTFC and ZnO thin films were allowed to deposit for the desired amount of time to achieve the desired thickness. When deposition was complete, the sample shutter was closed, ending deposition, and the plasma power turned off. Thin film thickness and deposition rates were pre-determined by depositing thin films on substrates coated with kapton tape. After deposition and annealing, the kapton tape was removed and the height difference between the thin film and substrate was measured using Taley Step.

When investigating the effect of the ZnO interface layers on BTFC, two variables were used. The first was the effect of annealing the ZnO interface layers prior to BTFC deposition, one set of samples were fabricated using BTFC deposited on as-deposited ZnO, and for the other half, the ZnO thin films were annealed at 700^{O}C in ambient atmosphere to change their crystallinity, prior to BTFC deposition. The second variable was the post- deposition annealing temperatures of the BTFC thin films. All BTFC thin films were annealed for one hour in ambient atmosphere after deposition, but the temperature was varied between 550^{O}C, 650^{O}C, 700^{O}C and 750^{O}C.

Annealed ZnO interface layers were fabricated by depositing 180 nm ZnO on P-type Si (111) and then annealing in a preheated ambient atmosphere at 700 ^{O}C for 60 minutes. BTFC thin films were then deposited onto these ZnO interface layers. As-deposited ZnO thin films were achieved by depositing 180nm of ZnO on silicon, followed directly by BTFC deposition without any further treatment to the ZnO layer. As Aston University's RF magnetrons sputter is a one target system, the vacuum of the sputtering chamber had to be broken so that the sputtering target could be changed, exposing the as-deposited ZnO thin films to atmospheric gasses prior to BTFC deposition. BTFC thin film annealing was performed in a pre-heated furnace for 1 hour in ambient atmosphere. The crystal structures of the ZnO and BTFC films were characterized using a XRD with an x-ray wavelength of 1.54 Å. Aurivillius phase BTO peaks were identified using the Joint Committee on Powder Diffraction Standards (JCPDS) card number 36-1486. SEM and EDS were performed using an FEI inspect-F SEM. The composition

and chemical bonding states of the BTFC thin films were characterized by X-ray photoelectron spectroscopy (XPS) (Thermo ESCAlab 250), using an X-ray source of Al Kα with an excitation energy of 15 keV and emission current of 6 mA. The analyser pass energy was 20 eV with a step of 0.1 eV and a dwell time of 50ms for the measurements. TEM was performed using a JEOL JEM-2100F, with a voltage of 200kV.

A list off the samples fabricated and variables is listed in table 2. All samples were deposited on silicon (111) substrates. ZnO interface layers were either as-deposited or annealed post deposition, with the deposition time varied to control thickness. All BTFC thin films were deposited utilising the same sputtering method, however, deposition time was again varied to control film thickness. BTFC post-deposition annealing temperature was varied, but always performed for 1 hour in an ambient atmosphere.

Sample number	ZnO interface layer type	ZnO interface layer thickness (nm)	BTFC thin film thickness (nm)	BTFC layer annealing temperature (^{O}C)
1	None	None	100	650
2	Annealed	180	None	None
3	Annealed	180	300	None
4	Annealed	180	300	550
5	Annealed	180	300	650
6	Annealed	180	300	700
7	Annealed	180	300	750
8	As-deposited	180	None	None
9	As-deposited	180	300	None
10	As-deposited	180	300	550
11	As-deposited	180	300	650
12	As-deposited	180	300	700
13	As-deposited	180	300	750
14	As-deposited	50	300	700

Table 2 details of fabricated samples.

Two or more copies of each sample were measured in XRD, SEM, XPS and EDS measurements. Only one sample was measured in TEM

4.3 Results and Discussion

The crystallinity of BTFC deposited directly onto p-Si (111) substrates (Sample 1) was first investigated. Figure 4.1 presents the XRD of 100nm BTFC deposited on silicon, and annealed post-deposition at 650^{O}C for one hour in ambient atmosphere. Data between 2-theta = 27^{O} to 29^{O} was removed due to the strong silicon substrate reflection.

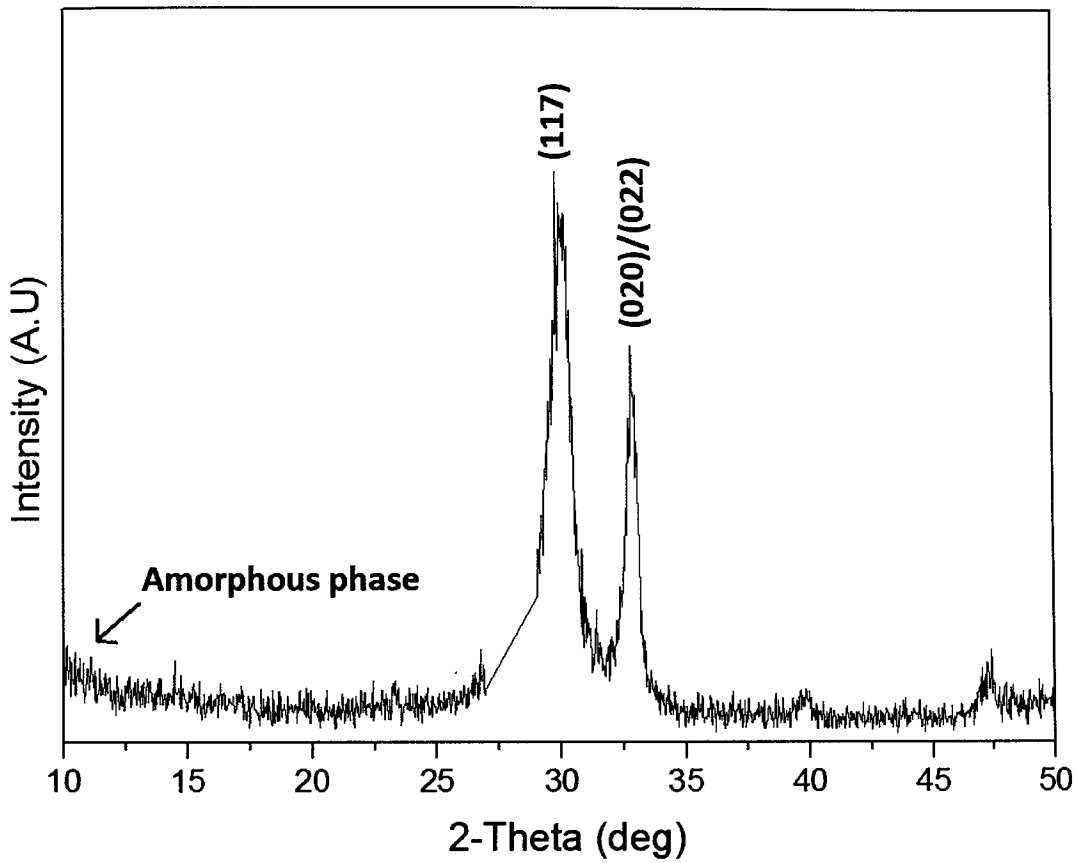

Figure 4-1 XRD pattern 100nm of BTFC thin films deposited directly onto P-Si (111) and annealed post deposition at 650^{O}C in ambient atmosphere.

Aurivillius BTO phase peaks can be seen at 2-theta = 29.73^{O} and 32.76^{O}, characteristic of the (117) and overlapping (020)/ (022) BTO orientations respectively. A curve can be seen at low 2-theta angles, indicating the presence of amorphous phase material. The (117) peak is broad, indicative of a small crystallite size and poor crystallinity, by utilising the Scherrer equation, the crystallite size of the (117) phase is calculated to be 8.4nm.

To compare the crystallinity of BTFC on silicon with and without a ZnO interface, the crystallinity of BTFC thin films on p-Si (111) substrates with ZnO interface layers was characterised by XRD. Samples consisted of 300nm BTFC thin films deposited on (111) p-Si

substrates with 180nm ZnO interface layers. The effect of the ZnO interface layer pre-treatment, and the annealing temperature of the BTFC thin films were investigated.

Figure 4.2 presents the XRD diffraction patterns of the BTFC thin films deposited on silicon with annealed ZnO interface layers (samples 2 through 7). The diffraction pattern for the interface layer, the as-deposited BTFC, and BTFC annealed at 550^{O}C, 650^{O}C, 700^{O}C and 750^{O}C in ambient atmosphere are presented. Data points between 2-theta = 27^{O} to 29^{O} were omited due to the strong silicon reflection.

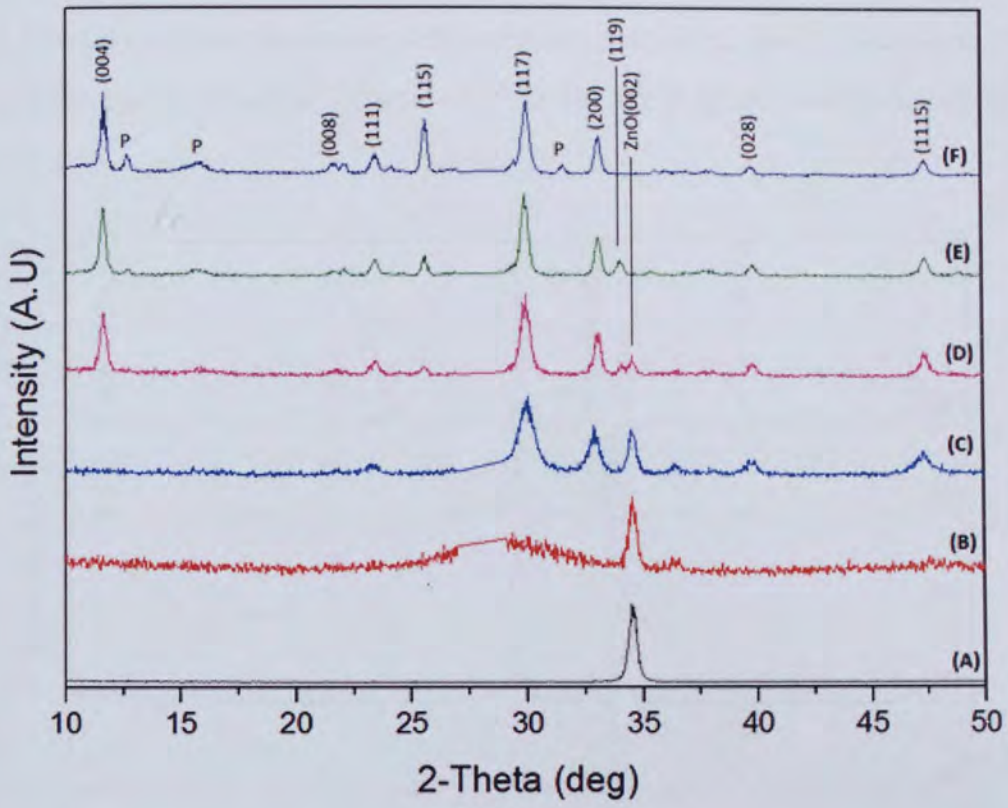

Figure 4-2 XRD patterns of 300nm BTFC thin films on annealed ZnO interface layers, (A) Annealed ZnO interface layer on P-Si(111), (B) BTFC thin film on ZnO interface layer without annealing, (C) BTFC annealed at 550^{O}C, (D) BTFC annealed at 650^{O}C, (E) BTFC annealed at 700^{O}C, (F) BTFC annealed at 750^{O}C. Pyrochlore phase peaks labelled 'P'. ZnO peaks labelled 'ZnO'.

Figure 4.2.A presents the diffraction pattern for the annealed ZnO interface layer, it shows a single crystalline peak characteristic of (002) orientated ZnO(120). The diffraction patterns of as-deposited BTFC seen in figure 4.2.B presents no crystalline peaks except the underlying crystalline ZnO peak, indicating the as-deposited thin film is amorphous. Figure 4.2.C, 4.2.D, 4.2.E and 4.2.F present the diffraction patterns of BTFC annealed at 550^{O}C, 650^{O}C, 700^{O}C and 750^{O}C respectively. The diffraction patterns show the existence of Aurivillius phase BTO, with dominant (117) orientation and other notable (004), (008), (111), (1115), (200), (119), (028)

and (115) peaks. In addition, peaks characteristic of pyrochlore phase BTO, $Bi_2Ti_2O_7$, labelled 'p'(121-124) can be seen at high temperatures. The underlying ZnO (002) is also present at lower temperatures, with the intensity dropping as the temperature increases. This can be attributed to the x-rays being unable to penetrate the BTFC thin film as crystallinity increases with annealing temperature.

Figure 4.3 presents the XRD of BTFC thin films deposited on Si(111) with as-deposited ZnO interface layers (Samples 8 through 13). The diffraction pattern of the as-deposited ZnO interface layer, the as-deposited BTFC thin film on as-deposited ZnO interface layers, and BTFC thin film on ZnO interface layers after annealing at 550°C, 650°C, 700°C and 750°C are included. Data points between 2-theta = 27° to 29° were again omitted due to the strong silicon reflection.

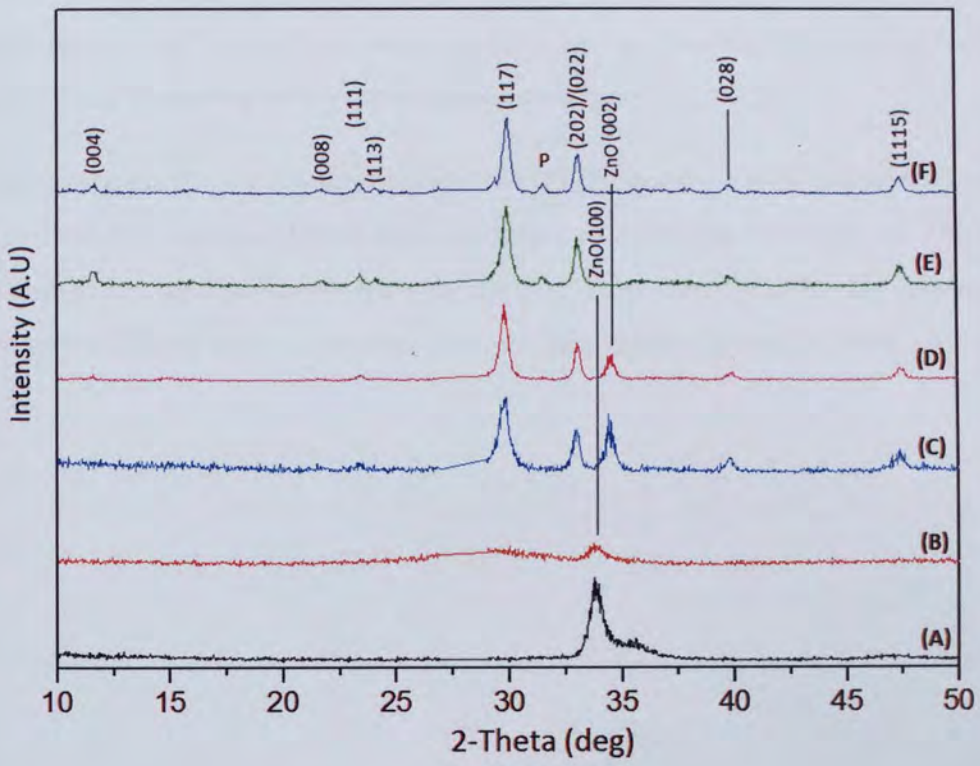

Figure 4-3 XRD patterns of 300nm BFCT thin films on as deposited ZnO interface layers, (A) As-deposited ZnO interface layer on Si(111), (B) BTFC thin film on ZnO interface layers without annealing; (C) BTFC annealed at 550°C, (D) BTFC annealed at 650°C, (E) BTFC annealed at 700°C, (F) BTFC annealed at 750°C. Pyrochlore phase peak labelled 'P'. ZnO peak is labelled 'ZnO'.

Figure 4.3.A presents the diffraction pattern of the as-deposited ZnO interface layers. The diffraction pattern presents (100) oriented ZnO located at 2 θ = 33.8° theta, were as the (002) orientated peak present in annealed ZnO interface layers was previously located at 2θ = 34.5(125) This change in orientation can be attributed to a the ZnO interface layer switching to a preferred orientation during

the annealing process. Figure 4.3.B presents the diffraction pattern for as-deposited BTFC on as-deposited ZnO. No other peaks can be observed except for the underlying ZnO peak are present, indicating the film is non-crystalline. Figure 4.3.C, 4.3.D, 4.3.E and 4.3.F present the diffraction patterns of BTFC annealed at 550^{o}C, 650^{o}C, 700^{o}C and 750^{o}C respectively. The films are Aurivillius in phase as evident by the (004), (008), (111), (113), (117), the overlapping (202)/(022) ,(028) and (115) peaks. A single pyrochlore phase peak, labelled 'p' is present in the films annealed at higher temperatures. Peaks characteristic of the (002) orientation of ZnO are present at lower temperatures annealing, indicating the ZnO interface layer has undergone a change in crystallinity during BTFC annealing, changing dominant orientation from (100) to (002).

For BTFC deposited on both annealed and as-deposited ZnO interface layers, the films show peaks characteristic of Aurivillius phase BTO. This indicates that the BTFC thin films have retained their ferroelectric Aurivillius phase after La, Nb, Fe and Co elements have been inserted into the crystalline structure. It is observed that the full width at half maximum (FWHM) of the (117) peak for BTFC thin films on both types interface layers decreases with increasing annealing temperature, indicating that the crystallite size is increasing with increasing annealing temperature(56).

Using the Scherrer equation, the crystallite size of the (117) phase was calculated for BTFC on annealed and as-deposited ZnO interface layers over all ranges of annealing temperature. The plot of the crystalline domain size against temperature for the (117) orientation of BTFC thin films deposited on silicon both with annealed and as-deposited ZnO interface layers is presented in Figure 4.4.

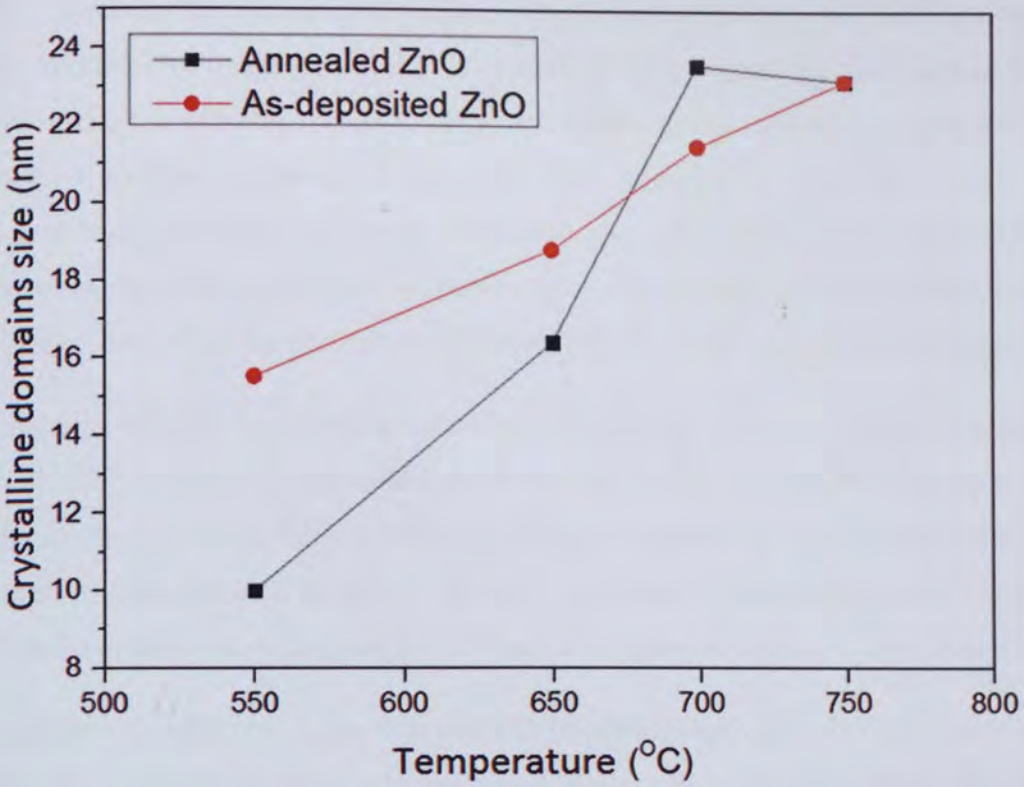

Figure 4-4 The grain size of BTFC annealed at different temperatures on P-Si(111) with annealed ZnO (black) and As-deposited ZnO (red) interface layers, as calculated by the Scherer equation.

The crystallite size can be observed increasing with annealing temperature, with the crystallite domain size doubling between 550°C and 750°C for BTFC on annealed ZnO interface layers. Wang et al (126) investigated the crystallite size of BTO on fused quartz substrates using the metalorganic solution deposition technique. They found that the crystallite domain size of films annealed at 650°C and 550°C were 18.3 nm and 15.4 nm respectively, indicating that inserting Fe, Co, Nb and La, and the use of a ZnO buffer layer, has not significantly influenced the crystallite size. The increase in crystallite size with increasing annealing temperature can be attributed to the increase in thermal energy during the annealing process, which breaks down existing chemical bonds and provides energy to form the crystalline phase.

As discussed in chapter 3.3.1.1, error occurs in the Scherrer equation due variations in the Bragg angle, resulting from changes in internal stress. By examining the bragg angle of the (117) peak, we can see that BTFC deposited on annealed ZnO has a constant 2-theta value for the (117) peak indicating no change in the films internal stress. However, BTFC deposited on as-deposited ZnO gradually shifts to higher values of 2-theta at higher temperatures, from 2-theta = 29.8° at 550°C to 2-theta = 29.95° at 750°C. This would result in the calculated crystallite size increasing slightly as the temperature increased. However, as the change is just 0.15° degree, it would not have any major effect on the calculation.

It is evident, by comparing the XRD of BTFC with and without ZnO buffer layers, that inserting a ZnO buffer layer improves the crystallinity of BTFC thin films. BTFC deposited directly on silicon without a ZnO interface layer has a smaller crystallite size as determined by the Scherrer equation, and possess large amounts of amorphous material. In comparison, BTFC deposited on either type of ZnO interface possess a large crystallite domain size at the same annealing temperature, and presents no evidence of amorphous material, indicating improved crystallinity. This can be attributed to ZnO acting as a diffusion barrier, preventing the absorption of oxygen from the BTFC into the silicon substrate.

At a temperature of 650^{o}C, secondary phase pyrochlore BTO, $Bi_2Ti_2O_{17}$, begins to appear. The formation of this phase can be attributed to the volatile nature of bismuth, resulting in it being vaporised from the thin film at high temperatures. This phase appears at temperatures of 600^{o}C when BTO has been deposited directly on Si(111), as reported elsewhere(58), indicating the insertion of a ZnO interface layer does not suppresses the emissions of volatile bismuth.

The investigation using XRD concludes that the BTFC retains its Aurivillius phase structure after the doping of La, Nb, Co and Fe elements into the target. The insertion of a ZnO interface layer between the BTFC thin film and the silicon substrate improves the crystallinity of BTFC, promoting larger crystallite sizes, and preventing the formation of amorphous material. The use of an annealed ZnO interface layer promotes larger crystallite size at lower temperatures than an as-deposited ZnO interface layer. However, both types produce films of similar quality in the 700^{o}C to 750^{o}C annealing region. Like BTO deposited on P-Si reported elsewhere, the thin films are predominantly (117) in orientation, with multiple secondary C-axis orientations.

To further investigate the effect of the ZnO interface layer and annealing temperature on the crystallinity of BTFC. The surface morphology of BTFC deposited directly on silicon and deposited on annealed and as deposited ZnO interface layers after post deposition annealing at different temperatures was investigated by SEM. The SEM of 100nm BTFC deposited directly on Silicon and annealed at 650^{o}C (sample 1) is presented in figure 4.5.

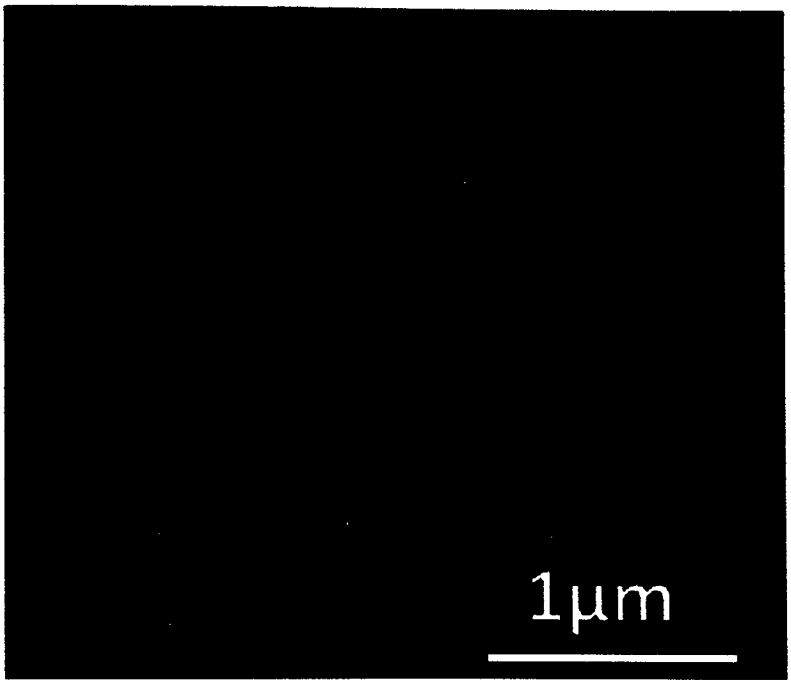

Figure 4-5 SEM images of 100nm BTFC deposited directly onto P-Si (111) substrates and annealed at 650°C for 1 hour in ambient atmosphere.

BTFC deposited directly onto silicon shows smooth granular features, with featureless regions between them, indicating an amorphous phase surface layer.

The SEM images for the annealed ZnO interface (sample 2), the as-deposited BTFC thin films on annealed ZnO interfaces (sample 3) and BTFC thin films annealed at 550°C, 650°C, 700°C and 750°C on annealed ZnO interface layers (sample 4 through 7) are shown in Figure 4.6.

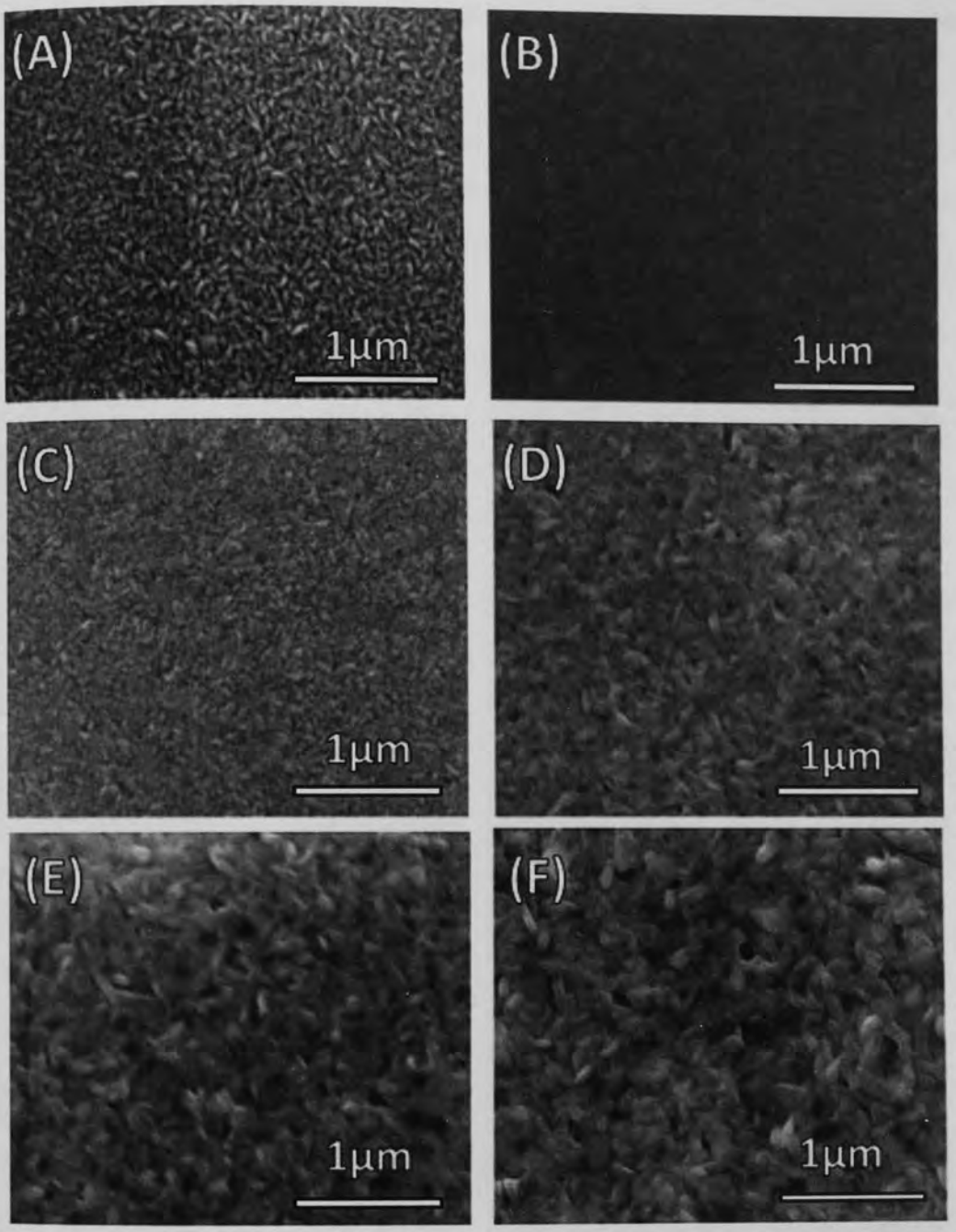

Figure 4-6 SEM images of BTFC thin films on p-Si(111) with annealed ZnO interface layers, A) The annealed ZnO interface layer, B) As-deposited BTFC, C) BTFC annealed at 550°C, D) BTFC annealed at 650°C, E) BTFC annealed at 700°C, F) BTFC annealed at 750°C.

Figure 4.6.A shows the surface morphology of the ZnO interface layer. The film shows crystallised granular features with a randomly orientated pallet-like structures. Figure 4.6.B presents the as-deposited BTFC on annealed ZnO interface layers, the film presents large islands of poorly crystalline material, suggesting an amorphous phase material, as seen in the XRD. Figures 4.6.C, 4.6.D, 4.6.E, 4.6.F present the surface morphology after annealing at 550°C, 650°C, 700°C and 750°C respectively. When annealed at 550°C, the amorphous materials form pallet-like granular features with random orientations. With increasing temperature, the size of the features increases, but the random orientation remains. For films annealed at 550°C, the width varies from 17.2nm to 39.4nm, and the

length varies from 70nm to 125.4nm. For the largest features in films annealed at 750°C, the width varies from 70nm to 135nm, and the length varies from 162nm to 223.8nm.

The SEM images for BTFC on as-deposited ZnO interface layers is presented in Figure 4.7. The surface morphology of the as-deposited ZnO interface layer (sample 8), the as-deposited BTFC (sample 9), and BTFC annealed at 550°C, 650°C, 700°C and 750°C(sample 10 through 13) are included.

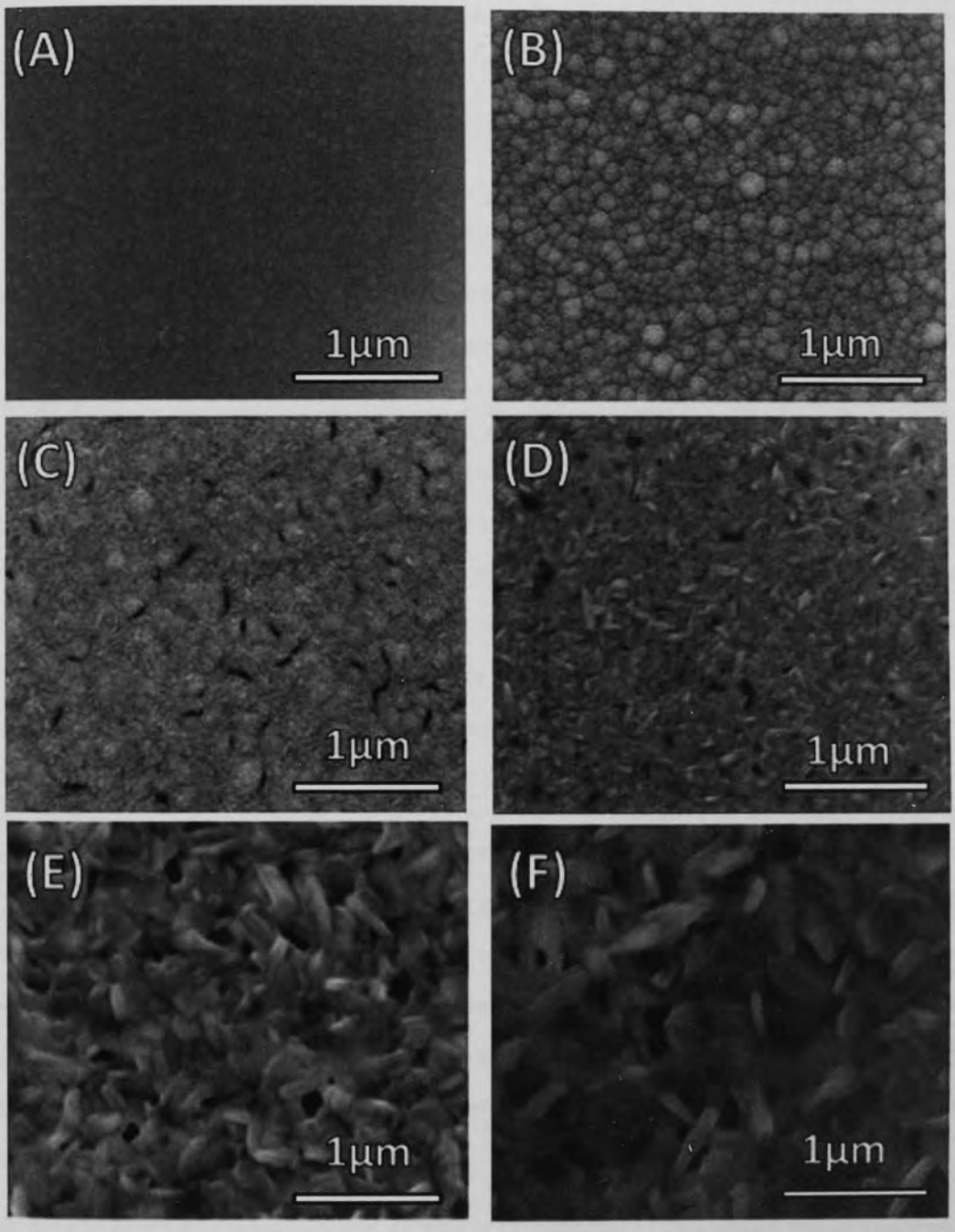

Figure 4-7 SEM images of BTFC thin films on P- Si(111) with annealed ZnO interface layers, (A) ZnO interface layers, (B) As-deposited BTFC (C), BTFC annealed at 550°C, (D) BTFC annealed at 650°C, (E) BTFC annealed at 700°C, (F) BTFC annealed at 750°C.

Figure 4.7.A presents the surface morphology of the as-deposited ZnO interface layer. The surface present granular features that are significantly smoother than that of annealed ZnO. The as-deposited BTFC seen in figure 4.7.B is still amorphous like, indicating good heteroepitaxial growth of as-deposited BTFC on ZnO interfaces. Like BTFC on annealed ZnO interfaces, BTFC annealed at 550^{o}C, 650^{o}C, 700^{o}C and 750^{o}C shown in figure 4.7.C, 4.7.D, 4.7.E and 4.7.F present pallet like granular features with random orientation, with surface-feature size increasing with annealing temperature. For the films annealed at 550^{o}C the feature length varies between 50nm and 60nm, and the width varies between 5.88nm and 9.24nm. For films annealed at 750^{o}C, the length varies between 280nm and 492nm, and the width varies between 86nm and 153nm.

By comparing the surface morphology of BTFC on silicon (figure 4.5), and BTFC on both types of ZnO interface layers, annealed at the same temperatures (4.6.D and 4.7.D), It can be see that inserting a ZnO layer improves crystallinity, eliminating amorphous phase material, and increasing the granular structure size. Surface roughness also increases, which can be attributed to the roughness of the ZnO interface layer.

By comparing the surface morphology of the two interface layers (Figure 4.6.A and 4.7.A), the roughness of the ZnO surface layer increases after annealing. The as-deposited BTFC thin films present a non-crystalline phase, suggesting they are amorphous in nature. The XRD data also suggests the as-deposited thin films poorly crystalline, indicating that the thin films require thermal energy to form the Aurivillius crystalline structure, with the surface roughness increasing with annealing temperature. Therefore, it is evident that both ZnO interface layers type and temperature play a role in promoting the preferential growth of plate-like grains, rather than round ones.

To investigate the chemical stability of the ZnO layer, TEM was used to investigate the cross-sectional area of 300nm BTFC thin films on (111) P-Si using an as-deposited 50nm ZnO interface layer (sample 14). As-deposited ZnO interface layers were chosen is to eliminate contamination during the ZnO annealing process. A 50nm ultra-thin layer was used so to better investigate the atomic/ion diffusion across the interface boundaries. The BTFC layer was annealed at 700^{o}C in ambient atmosphere, to maximize crystallinity, whilst avoiding a peak temperature of 750^{o}C to minimise secondary phase pyrochlore growth.

The cross-sectional TEM of 300nm BTFC on P-Si (111) with an as-deposited 50nm interface layer is presented in Figure 4.8.

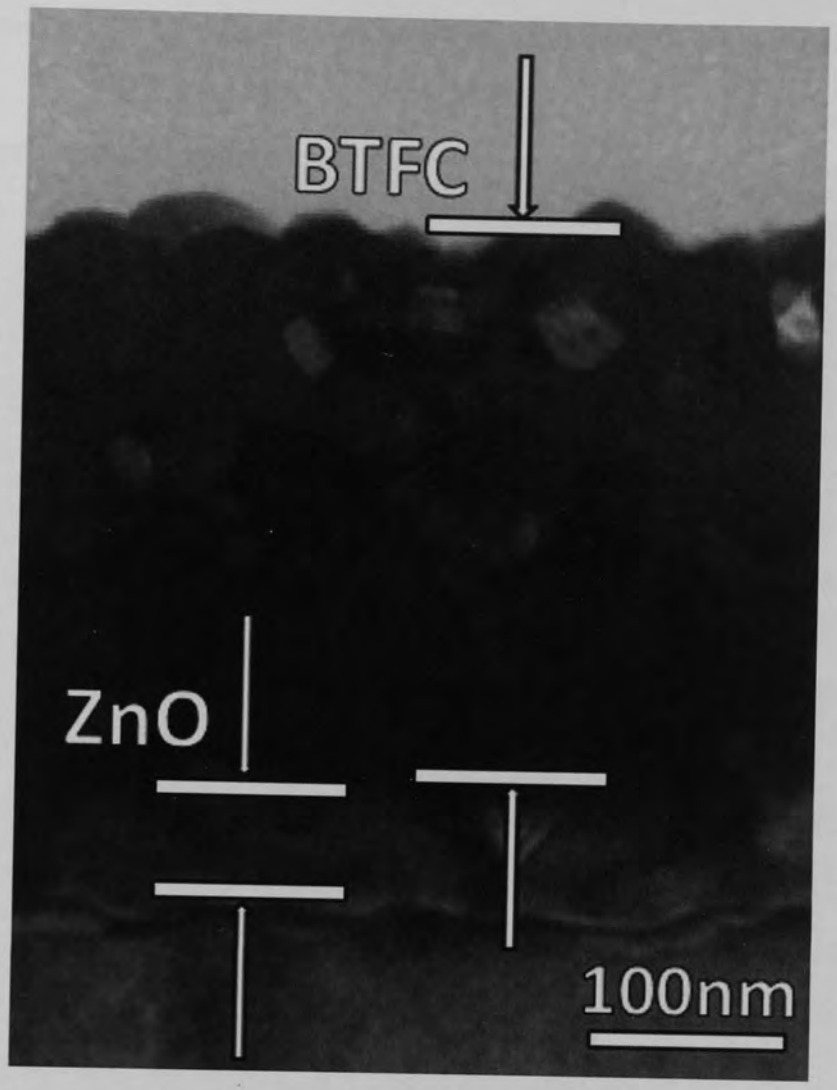

Figure 4-8 Cross-sectional TEM of 300nm BTFC on 50nm ZnO interface layers.

As seen in figure 4.8, the as-deposited ZnO layer appears to crystalline, supporting the evidence in the XRD data that the as-deposited ZnO layers crystallises during the BTFC annealing stage. The BTFC surface, and BTFC/ZnO interfaces appear very rough, which can be attributed to the large grain size of both films. The thickness of the rough ZnO film varies between 40 and 65nm showing a big variation in the exact interface layer thickness.

To investigate the crystalline structure of the BTFC thin film and the BTFC/ZnO interface, HRTEM was utilised to investigate these regions of the film. HRTEM of the BTFC thin film is shown in Figure 4.9 and

the HRTEM on the ZnO/BTFC interface is shown in Figure 4.10, key BTO planes based on d-spacing are labelled.

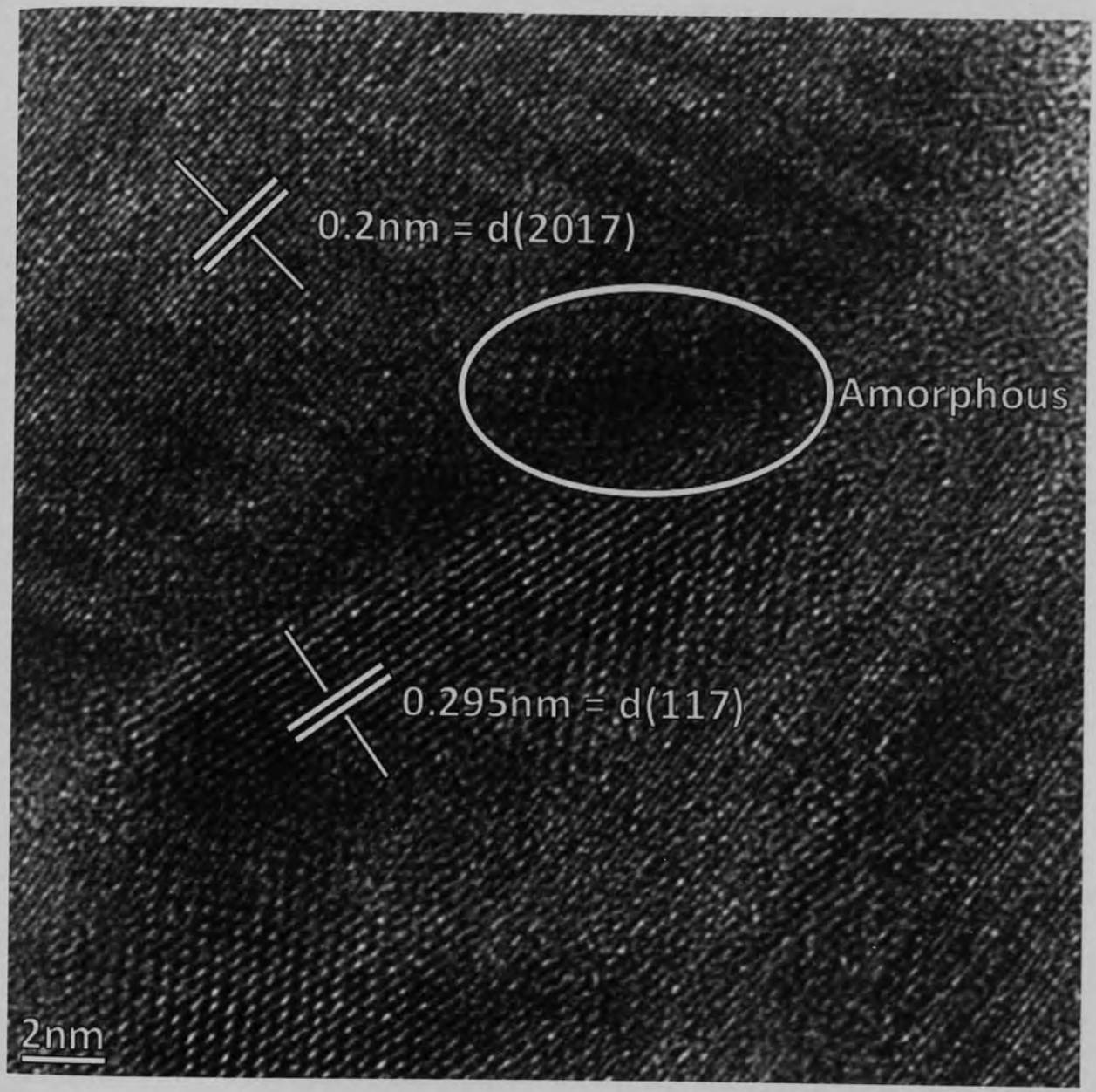

Figure 4-9. HRTEM image of 300nm BTFC on 50nm ZnO interface on P-Si(111) substrates.

The HRTEM of the BTFC thin films shows a largely crystalline film with mixed orientations. Amongst the BTFC crystalline phases, some deposits of amorphous material remain between the grain boundaries, which has been reported elsewhere for BTO thin films (127). By measuring the d-spaceing of the presented crystalline lattices, we can determine that the plane separation of the 0.295nm is characteristic of the (117) phase of Aurivillius phase BTFC (128), whilst the d-spacing of 0.2nm can be accredited to the (2012) phase of Aurivillius BTFC (127). The (117) orientation of BTFC was present in the XRD of BTFC deposited on annealed ZnO as seen in figure 4.3.

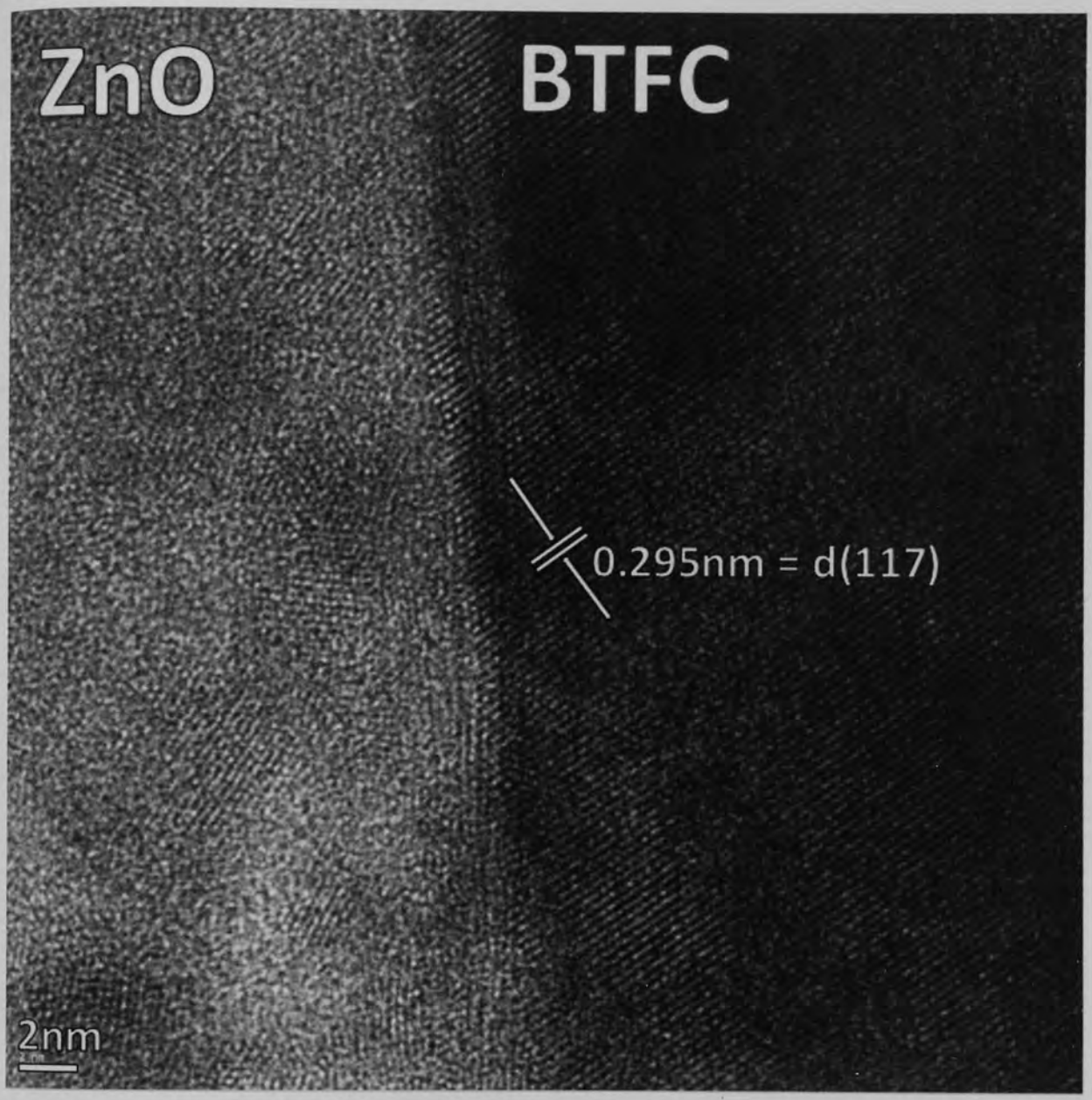

Figure 4-10 HRTEM image of ZnO/BTFC interface layer- Left ZnO interface layer, right BTFC thin film.

HRTEM was used to investigate the ZnO/BTFC thin film junction and is presented in Figure 4.10. The images show a well define ZnO/BTFC interface layer. The BTFC thin films at the interface are predominantly (117) axis in orientation.

Select Area Electron Diffraction (SAED) of the BTFC thin film is presented in Figure 4.11. The SAED shows a polycrystalline film with two dominant orientations and multiple smaller ones, and a bright circle, indicative of amorphous phase material. These multiple smaller diffractions are characteristic of BTO thin films with multiple orientations as investigated by Suyal et al (129). This confirms that the films are polycrystalline with multiple orientations, as seen in the XRD of BTFC thin films on as-deposited ZnO buffer layers seen in Figures 4.2 and 4.3. The bright circle is evidence of a polycrystalline phase thin film, with the circle occurring due to diffraction of electrons in all directions by amorphous

phase material in the grain boundaries(130). This is contrary to the SAED pattern of single crystal BTO that possess no amorphous phase material(131).

Figure 4-11 Selected Area Electron Diffraction of BTFC thin films.

To examine if the ZnO interface layers aided in inhibiting diffusion between the BTFC thin films and Si substrates, the chemical abruptness of the interface was examined by elemental mapping. The results of which are plotted in figure 4.12.

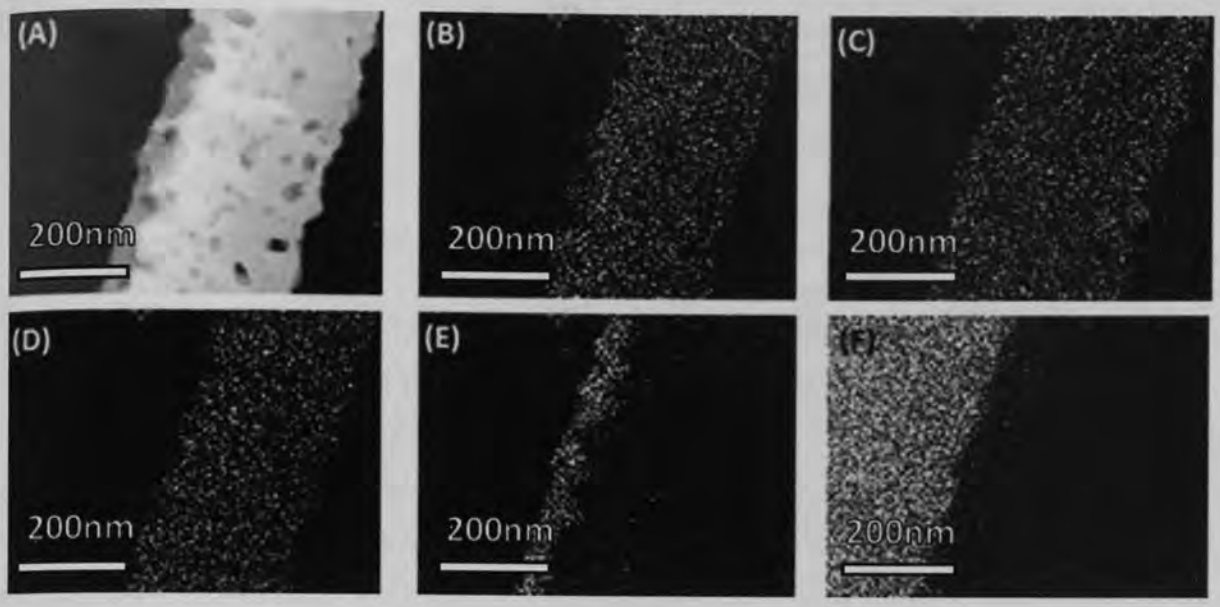

Figure 4-12 Elemental mapping of 300nm BTFC on P-Si (111) using a ZnO interface layer. (A) Image of the sample for dimension reference, (B) Bismuth elemental mapping, (C) Oxygen elemental mapping, (D) Titanium elemental mapping, (E) Zinc elemental mapping, (F) Silicon elemental mapping.

Figure 4.12.A shows the HRTEM with all three layers for reference, the uneven BTFC and ZnO interface layer are approximately 300nm and 45nm thick. Figure 4.12.B shows a high concentration of bismuth in the BTFC layer. Some bismuth is detected in the silicon, but as there is no gradient transition, it is likely due to the result of noise, rather than actual bismuth diffusion. Figure 4.12.C presents the oxygen concentrations, the concentration between the ZnO interface layer and BTFC layer is uniform. As the BTFC thin film has a higher concentration of oxygen than ZnO, this suggests oxygen is diffusing from the higher density BTFC to the lower density ZnO. Figure 4.12.D shows the titanium concentration, like bismuth, there is some evidence of titanium in the interface layer and the substrate, which can be attributed to noise due to the lack of gradient. Figure 4.12.E presents the zinc concentration, the highest concentration of zinc atoms can be found in the interface layer, however there is clear of evidence zinc diffusion into the BTFC thin film as evident by the zinc gradient, with higher concentration in the BTFC near the ZnO interface layer, and a lower concentration near the BTFC surface. Figure 4.12.F shows the distribution of silicon throughout the sample. Large quantities of silicon can be detected within the substrate, however silicon can be seen diffusing throughout the BTFC and ZnO thin films, as evident by the gradient.

The diffusion of atoms, can be explained by the following two mechanisms. One mechanism is the migration of particles between the amorphous BTFC and ZnO layers and Si substrate during the annealing process. As both BTFC and ZnO are as-deposited prior to annealing, both will experience the breakdown of existing bonds and the migration of atoms as they search for more stable bonds and phases during the annealing. It is likely that during this stage, zinc atoms diffuse from the ZnO interface

layer into the BTFC, and that oxygen diffuses from the higher concentration regions (BTFC) to the lower concentration region (ZnO). The other possible mechanism responsible for the migration of atoms is the re-sputtering of the ZnO layer during BTFC deposition. When atoms from the BTFC target land on the substrate coated with the ZnO interface layer during deposition, zinc particles are ejected by atomic bombardment from the surface and then absorbed into the BTFC thin films.

The ZnO interface layer has failed to completly prevent the diffusion of atoms between the BTFC and the substrate, as evident by the silicon diffusion into the BTFC films. Moreover, as ZnO has a lower concentration of oxygen than BTFC, oxygen can easily diffuse from the higher concentration (BTFC) to the lower concentration (ZnO), increasing the oxygen vacancies in BTFC which have been shown to lead to contribute to leakage current and domain pinning(132). It is also noted that zinc atoms have diffused from the ZnO to the BTFC layer. We can theorise that being a period 4 transition metal with a similar atomic radius to titanium, iron and cobalt, Zinc can diffuse into the Perovskite cubic structure and occupy B-site titanium positions, allowing BTFC to retain its Aurivillius phase structure, as evident by the XRD data.

TEM and HRTEM analysis show a rough interface between the two interfacial boundaries of the ZnO interface layers, resulting in the rough crystalline nature of ZnO. The ZnO interface layer fails to eliminate diffusion between the ferroelectric layer and substrate, with evidence of silicon and Zn atoms diffusing into the ZnO BTFC layer. Future investigations should involve repeating the experiment with an annealed ZnO interface layer, to see if the pre-treatment of the ZnO interface layer prior to BTFC annealing has any influence on the elemental diffusion.

In order to determine if the La, Nb, Co and Fe dopants have been successfully inserted from the target into the thin film, XPS and EDS were utilised to examine the chemical composition of 300nm BTFC annealed at 700^{o}C on (111) silicon with 170nm annealed ZnO interfaces(sample7). XPS was used to analyse the chemical binding energies of the BTFC thin film. The aim is to determine if the BTFC constitute elements possess oxide bonding, characteristic of the Aurivillius phase, rather than non-Aurivillius metallic clusters which may contribute to ferroelectric and ferromagnetic reading in future studies. XPS provides information regarding only the top 10nm of the thin films, so we must consider that the finding represents only the surface of the thin film, which often has different states than the bulk. Considering that the BTFC films are highly resistive the XPS peaks were calibrated by the C 1s core-level energy peak. Figure 4.13 presents sample high-resolution XPS core-level spectra, whilst Figure 4.14 presents the wide XPS spectrum of the sample.

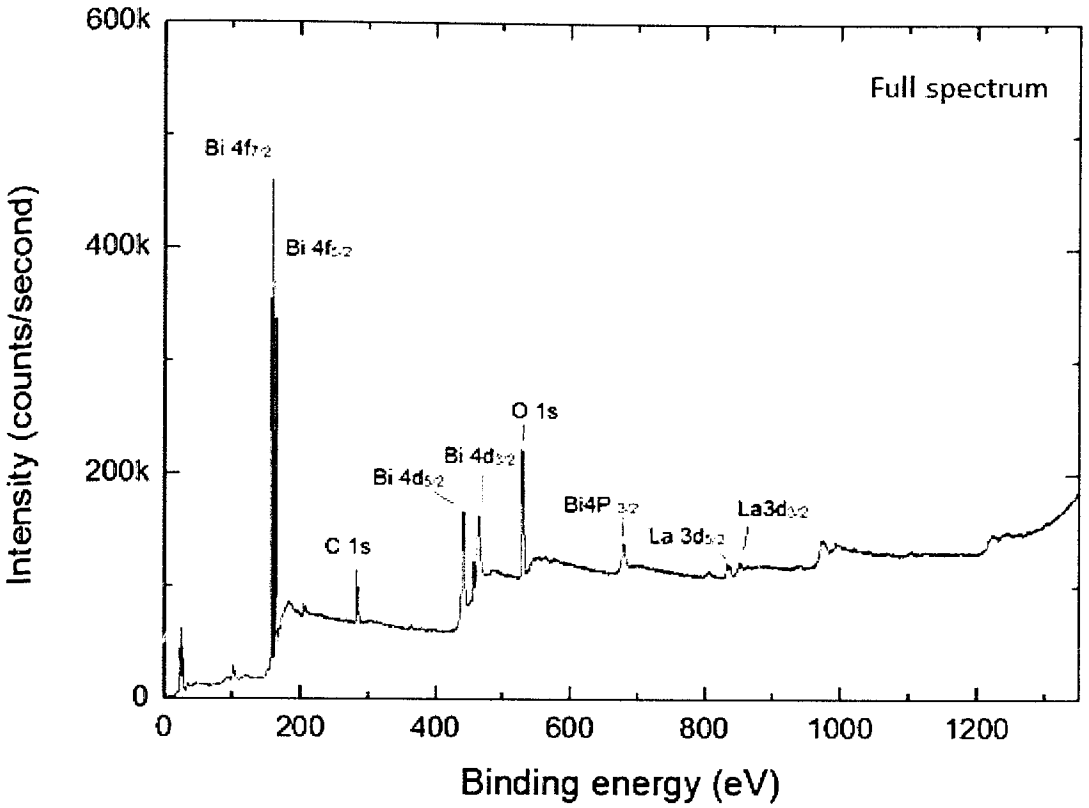

Figure 4-13.Wide spectrum XPS for BTFC thin films annealed at 700^{O}C on P- Si (111) with As-deposited ZnO interface layers.

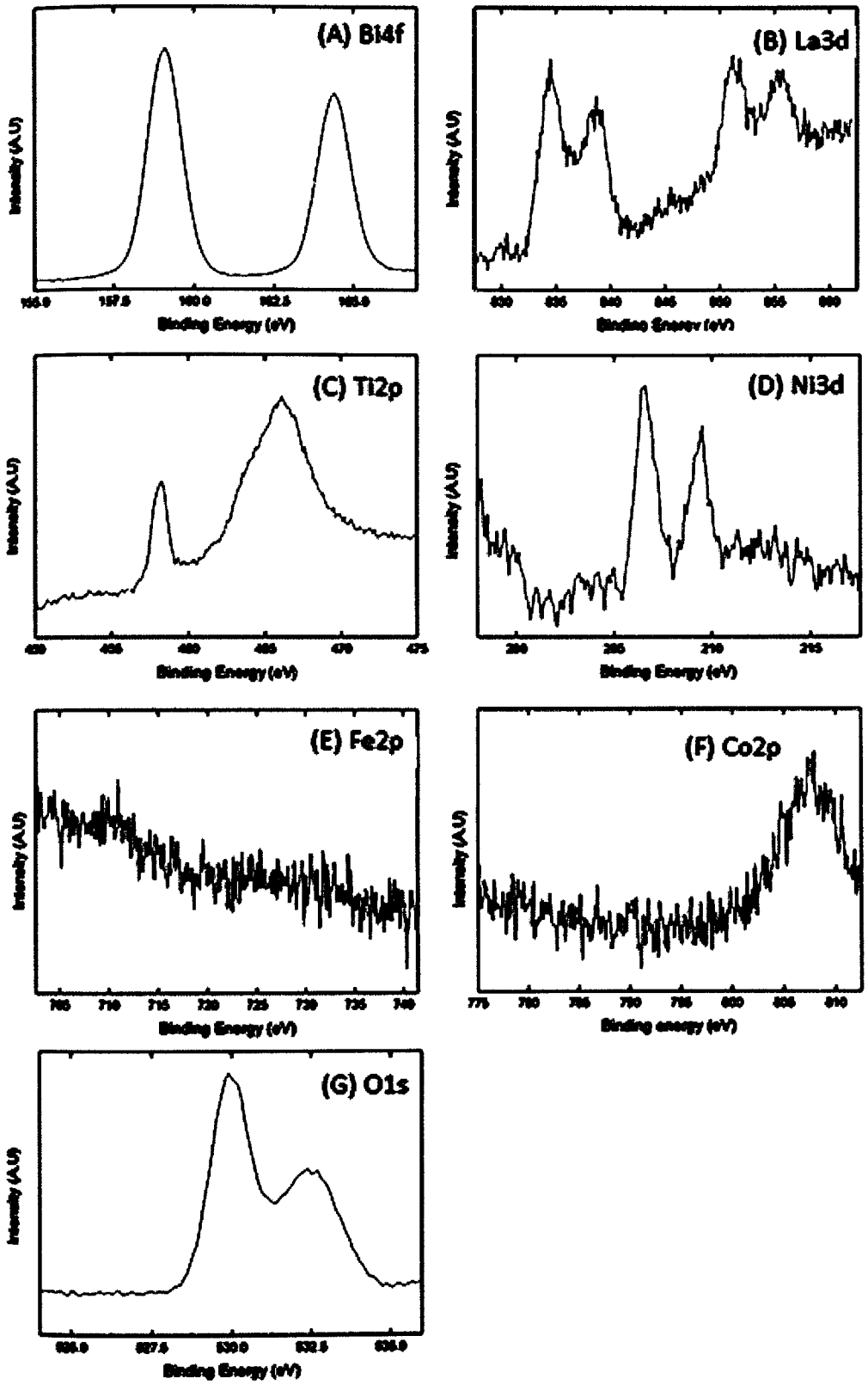

Figure 4-14 High-resolution XPS core-level spectra of Sample 14: (A) Bi4f, (B) La3d, (C) Ti2p, (D) Ni3d, (E) Fe2P, (F) Co2p, (G)O1s.

The survey spectrum, seen in figure 4.13, shows visible peaks consistent with BTFC constitute atoms bismuth, titanium and oxygen, it also shows that La has been successfully doped inside the BTFC thin films. Nb, Fe and Co peaks cannot be seen, which can be accredited to the low sensitivity of the wide

spectrum and the low doping content of those elements. Figure 4.14 illustrates the high-resolution XPS core-level spectra of the elements Bi, La, Ti, Nb, Fe, Co and O. The Bi 4f spectrum shown in Figure 4.14.A consists of a spin-orbit doublet with binding energies of 159.0 eV (Bi 4f7/2) and 164.3 eV (Bi 4f5/2), with binding energies similar to that of bismuth oxide binding energy reported for $Bi_4Ti_3O_{12}$ elsewhere(133). In the spectrum of the La 3d shown in Figure 4.14.B, two doublet peaks are observed, with the corresponding binding energy of 834.5 eV and 851.7 eV being for the La 3d5/2 and La 3d3/2 respectively, which is similar to the binding energy of oxide La_2O_3 reported elsewhere(134).The high resolution Ti 2p spectrum shown in Figure 4.14.C consists of a spin-orbit doublet with binding energies of 458.2 eV (Ti 2p3/2) and 466.1 eV (Ti 2p1/2). These binding energies are similar to that of the titanium oxide phase reported in BTO elsewhere(133). The Nb 3d peak shown in Figure 4.14.D at 206.6 eV is characteristic of the Nb_2O_5 oxide state, implying the oxide phase(135). XPS has difficulty detecting both Fe and Co dopants, it could be argued that some iron is detected as evident by the Fe 2p3/2 peak shown at 710.9 eV, which is consistent with the oxide Fe_2O_3 bond(136), however, this peak is barely above noise level. The Co2p3/2 oxide peak shown should ideally appear at 779.7eV, however no peaks distinguishable from noise can be seen at this point. Finally, XPS O1s spectrum is illustrated shown in Figure 4.14.G. The O 1s spectrum was fitted by two peaks: one is located at 529.8eV and the other at 532.6eV, these two peaks can be assigned to the Bi-O and Ti-O bonds respectively (137).

XPS confirms the presence of Aurivillius phase BTFC, with the prominent Bi4f, Ti2p and O1s core spectrum peaks possessing binding energies similar to that of BTO reported in other investigations. The Nb3d and La3d5 peaks were found to correlate to oxides also report elsewhere. Noise level Fe and Co can be attributed to the low doping concentrations in BTFC and the low sensitivity of XPS for these particular elements. Additionally, this could be attributed to surface 'dead layers' (138) without Fe/Co doping, which arise due to structural defects upon the surface. XPS analysis concludes that the BTFC composite elements are exist in oxide bonds characteristic of Aurivillius phase BTO, Fe and Co elements could not be confirmed, which can be attributed to Fe and Co deficient surface states.

To confirm the presence of iron and cobalt doping and to analyse the stoichiometric nature of BTFC thin films, EDS measurements were performed for the same sample. The EDS spectrum is presented in Figure 4.15 and atomic and weight percentage of elements is presented in Table 2.

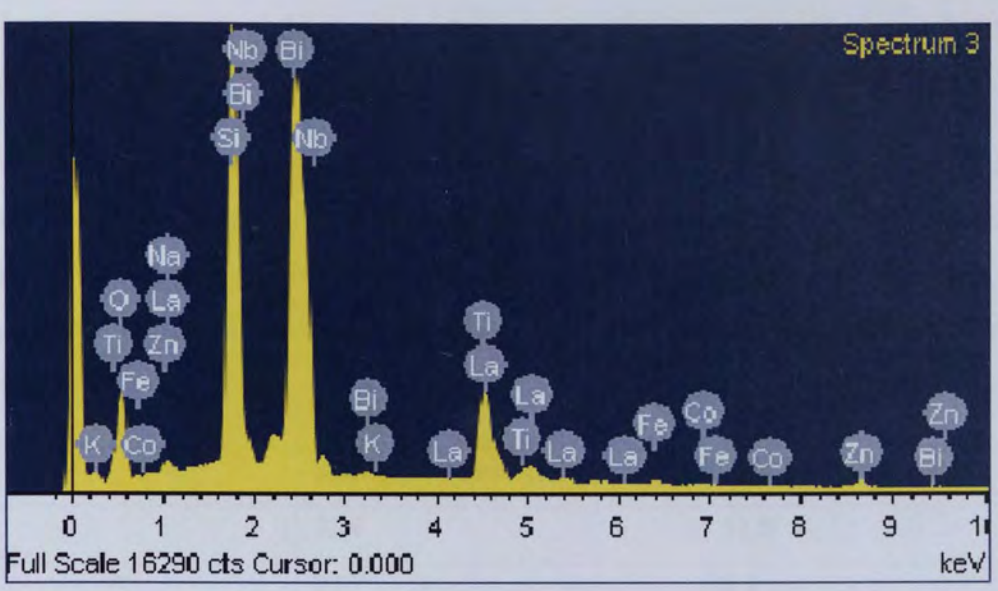

Figure 4-15. EDS spectrum for BTFC thin films annealed at 700°C on P- Si(111) with as-deposited ZnO interface layers.

Element	Weight %	Atomic %
Bi	49.3	10.8
La	5.3	1.7
Ti	6.8	6.5
Nb	2.6	1.3
Fe	0.5	0.4
Co	0.3	0.2
O	19.0	54.3
Zn	1.6	1.1
Si	14.2	23.0
Ni	0.3	0.6
K	0.01	0.01

Table 3 EDS elemental weight and atomic percentage of BTFC thin films annealed at 700°C on P- Si(111) with As-deposited ZnO interface layers.

The EDS spectrum of the BTFC sample shows distinct oxygen, bismuth, and titanium peaks with similar energy levels to BTO microparticles reported elsewhere(139). Additionally, a Lanthanum peak bordering the titanium peak around 4.5kEv is present, as well as a small niobium peak around 2.8KeV. Iron and cobalt peaks are also present but have low intensities. These low intensities can be attributed to the low concentrations within the thin film. The strong peak located at 1.8keV is characteristic of silicon as reported elsewhere (140), along with the presence of zinc, this indicated that the electron beam has penetrated the entire bulk of the thin film. EDS confirms that both Fe and Co elements have successfully been doped into the thin film. The lack of Co in the XPS data can, therefore, be attributed to the lower sample penetration of XPS (roughly 10 nm) and surface states in the BTFC thin film that

do not contain cobalt. Nickle and potassium elements are also detected, which can be attributed to surface impurities.

To compare the chemical composition of the BTFC thin film to that of the ideal sample, the atomic percentages of bismuth, lanthanum, titanium, niobium, iron and cobalt were compared to the ideal percentages of the target, the results are plotted in Table 3. Oxygen was subtracted from the calculation, as it is impossible to distinguish between contributions from the BTFC thin film and the ZnO interface layer.

Element	Ideal percentage (%)	Thin films Percentage (%)
Bi	46.4	51.5
La	10.7	8.4
Ti	35.7	31.0
Nb	3.57	6.1
Fe	1.79	1.9
Co	1.79	1.1

Table 4 Measures atomic percentage compared to ideal atomic percentage of BTFC thin films annealed at 700°C on P- Si (111) with as-deposited ZnO interface layers. Oxygen substrate due to ZnO interface layer interference.

The EDS data shows that all dopants have been successfully doped into the thin film. Cobalt and niobium levels showed larger deviation from the ideal percentages than other elements, however, repeat measurements performed found levels of niobium and cobalt closer to that of the ideal value, with similar levels of deviation found in other elements.

4.4 Conclusions

This chapter concludes that Aurivillius phase BTFC thin films have successfully been achieved on silicon substrates using zinc oxide interface layers. XRD data demonstrated that the insertion of a ZnO interface layer improves the crystallinity of BTFC, and aids in eliminating unwanted amorphous phase material. Aurivillius phase BTFC were demonstrated using both as-deposited and annealed ZnO interface layers. On both types of interface layers, the BTFC thin films were primarily (117) in orientation, typically of Aurivillius phase BTO thin films. BTFC deposited on as-deposited ZnO present a larger grain and crystallite size than pre-annealed ZnO when annealed at low temperatures, but present similar grain sizes above 700°C. At temperatures of 700°C, secondary pyrochlore phase was evaporated from the thin film, as evident by the formation of the Bi-deficient pyrochlore phase suggesting that the insertion of a ZnO interface layer does not prevent the formation of the secondary phase. Elemental mapping demonstrated zinc diffusion into the BTFC thin film, and O diffusion from

BTFC into the interface layer, indicating that as-deposited ZnO interface layers are limited in their function as diffusion barriers. EDS confirmed that cobalt and iron, as well as niobium and lanthanum had successfully been inserted into the BTFC lattice whilst maintaining the Aurivillius phase structure. The use of ZnO interface layers improves the quality and crystallinity of BTFC thin films when deposited onto silicon substrates.

Chapter 5 : The Investigation into the Electric and Ferroelectric Properties of BTFC Thin Films on Silicon with ZnO Interface Layers

5.1 Introduction

In the previous chapter, the author demonstrated that Aurivillius phase BTFC thin film, can be achieved on silicon substrates by utilising ZnO interface layers. For a ferroelectric thin films, most authors characterise the polarisation - electric field (P-E) loop of the material, However, these loops alone are not always sufficient to characterise the ferroelectric domain switching, due to mixed contributions from dielectric switching and leakage current to the measured hysteresis. Yan et al (24) proposed the triangular waveform voltage method for characterising ferroelectric materials, which succeeds in distinguishing leakage current and dielectric contributions from ferroelectric switching.

The aim of this chapter is to report on the properties of doped BTO thin film, $Bi_{3.25}La_{0.75}Ti_{2.5}Nb_{0.25}Fe_{0.125}Co_{0.125}O_{12}$ (BTFC), deposited on silicon substrates with ZnO interface layers, as demonstrated in the previous chapter. The leakage current and dielectric constant are investigated, as well as the ferroelectricity over a range of driving voltages.

5.2 Experimental

A thin film capacitor structure was fabricated to analyse the electronic properties of BTFC thin films deposited on silicon substrates with ZnO interface layers. The device consisted of a 600nm BTFC ferroelectric layer deposited on a 50-nm ZnO interface layer on p-type (100) silicon. Titanium metal contacts were deposited onto the BTFC and silicon surfaces to form top and bottom ohmic contacts, followed by tungsten carbide(WC) protection layers. Titanium was chosen for its affordability over gold when utilising rf magnetron sputtering. The device structure is presented in Figure 5.1.

Boron doped p-type silicon substrates were utilised in this investigation with a resistivity of 0.002-0.005 Ohmcm. To fabricate the capacitor device, silicon substrates were first cleaned by sonicating in acetone for 5 minutes, followed by rinsing in Di water, then blow drying with N_2. The process was then repeated, using isopropanol instead of acetone. Finally, the substrates were sonicated in deionised water, followed by blow drying with nitrogen. 50nm ZnO thin films were deposited directly onto the cleaned silicon surface by rf magnetron sputtering. The ZnO interface layer was left as-deposited prior to BTFC thin film deposition, as annealing the ZnO before BTFC deposition would risk contaminating the interface layer surface. 600nm BTFC thin films where deposited directly onto the ZnO interface surface. BTFC and ZnO layers where deposited using the same sputtering procedure described in chapter 4.2. Initial investigations were carried out using 300nm thick BTFC, consistent with the BTFC film thickness examined in chapter 4. However, these samples broke down at low driving voltages, prompting a repeat experiment with the thickness increased to 600nm to help prevent break down. After BTFC deposition, the sample was annealed at 700^{o}C for 1 hour in a vacuum environment of 1x10^{-}

^{3}Torr. The vacuum environment was utilised to prevent oxidation of the silicon substrate. Afterwards, titanium dot contacts were sputtered onto the silicon and BTFC surface form ohmic contacts on both surfaces, followed by tungsten carbide protection layers. The diameter of the dotted contacts was 430 μm.

Thin films and electrode contacts were deposited using Aston University's RF-Magnetron sputterer. Sample annealing was performed using a Siomm SGL-1700 furnace. Thin film crystallinity was investigated by XRD using a Bruker d8 with CuKa1 radiation with wavelength of 1.57 Å. C-V and leakage current measurements were performed using a Keithley 4200 Semiconductor Analyser, and ferroelectricity was measured using the triangular voltage waveform method described in chapter 3.3.7.

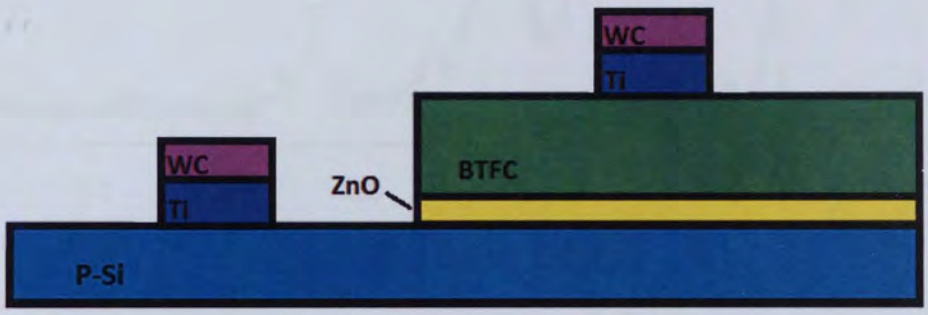

Figure 5.5-1 Device configuration of BTFC thin films on P-Si using ZnO interface layers. 50nm ZnO is deposited directly onto P-Si, followed by 600nm BTFC. After sample annealing in vacuum atmosphere, Ti contacts are deposited onto the silicon and BTFC to form electronic contacts, followed by a tungsten carbide (WC) protection layers.

5.3 Results and Discussion

To confirm that the BTFC thin film sample retains its Aurivillius phase structure after annealing in a vacuum atmosphere rather than an ambient atmosphere, XRD measurements were performed to examine the devices crystallinity, the results of which are presented in figure 5.2.

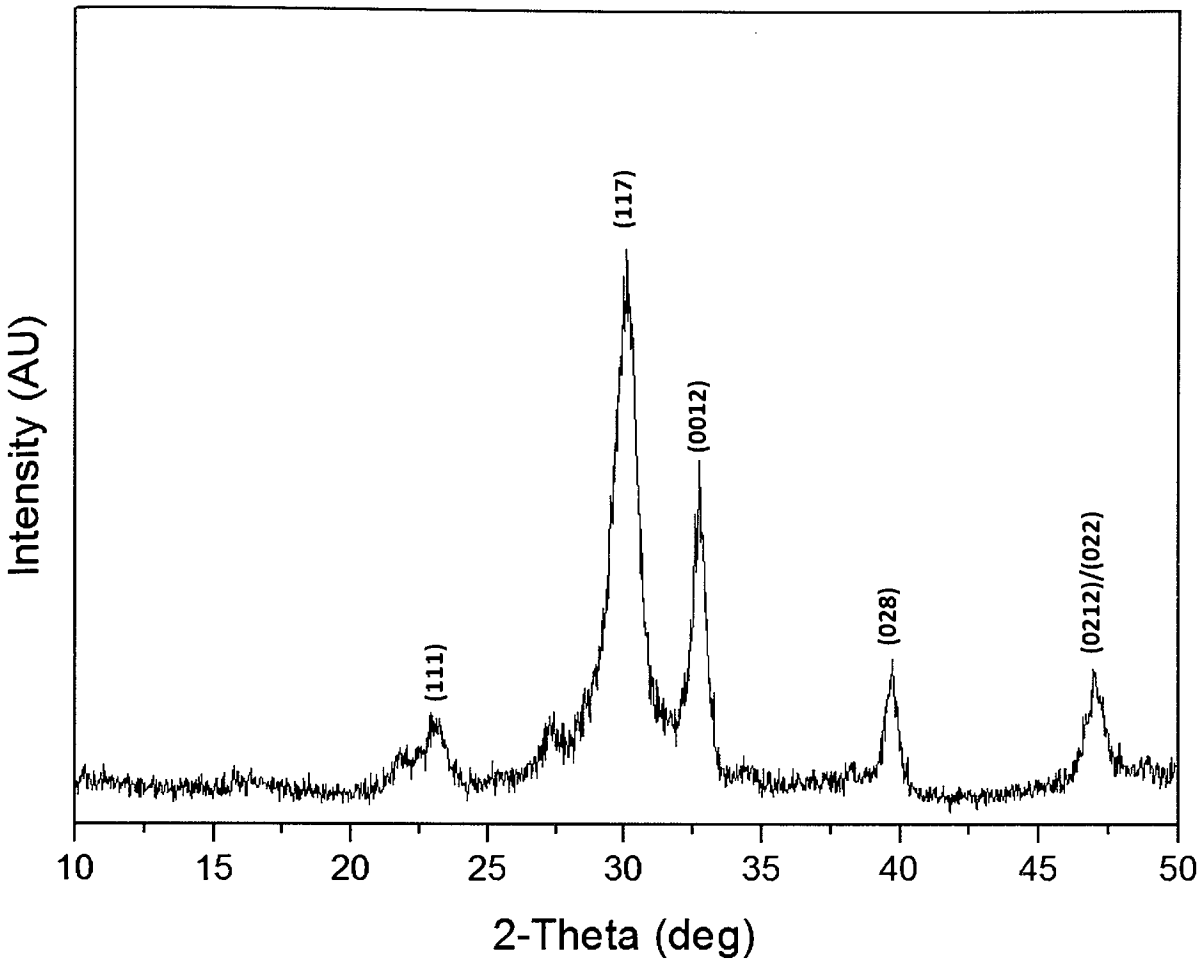

Figure 5-2 XRD pattern of device 1, which consists of 600nm BTFC thin films on P-Si substrates with 50nm ZnO interface layers. Samples annealed in vacuum for 1 hour at 700°C.

After annealing in vacuum, the BTFC thin film retain its Aurivillius BTO phase, with high intensity (117) and (0012) orientations, in addition to (111), (028) and the overlapping (0212)/(022) orientations. Using the Scherrer equation, the crystallite domain size of the (117) peak was calculated to be around 6.8nm. This result confirms that BTFC thin films retain its Aurivillius phase after annealing in vacuum, rather than ambient atmosphere.

Prior to any thin film electrical measurements, the silicon's series resistance with the BTFC thin film capacitor was measured. This was performed by measuring the resistance across a pair of silicon surface contacts, with identical separation as those used to make contact across the BTFC thin film and silicon. Since the silicon is boron-doped and offers very high electrical conductivity, the resistance effect of the silicon substrate can be ignored.

To determine the leakage properties of the BTFC thin film, the leakage current density (J) against Electric Field (E) across the device was measured, and is presented in figure 5.3.

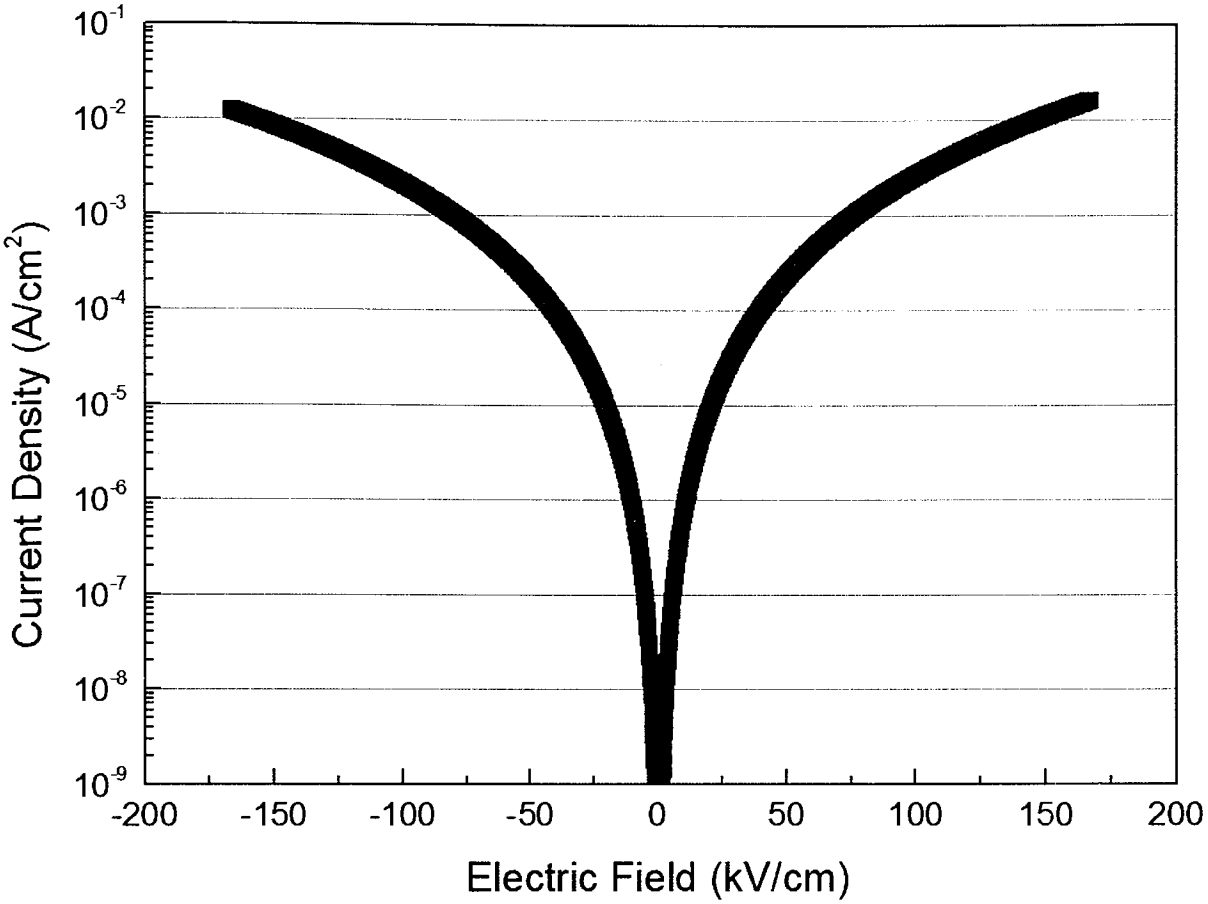

Figure 5-3 Current density (J) – Electric Field (E) for BTFC thin films on silicon with ZnO interfaces layers.

Current density was measured over the range of 0 to 10 V, the equivalent of 0 to 167 kV/cm. Leakage current density peaks in the positive region at 0.0164 A/cm^2, and at 0.0125 A/cm^2 in the negative region. This difference in current is typical for asymmetrical capacitors (141). The leakage current measured is larger than that of non-doped BTO deposited reported elsewhere (142-144). This comparably large leakage current can be explained by two possible mechanisms: firstly most BTO thin films reported are c-axis oriented, which possess a higher resistivity due to the insulating nature of the Bi_2O_2 layer(49). Were-as our XRD result show the films have a non-c axis orientated crystal dominance of (117). Secondly, the annealing in a vacuum environment will lead to the generation of oxygen vacancies within the thin film (145). Oxygen vacancies act as free charge carriers, contributing to electric conduction (132, 140, 146).

To examine the dielectric nature of the BTFC thin films, the capacitance was measured over the same range of voltages. The capacitance against electric field relationship is plotted in figure 5.4. The measurement was performed by sweeping the voltage from positive bias to negative bias and back again. A measurement signal of 30mV$_{rms}$ with a frequency of 1MHz was used.

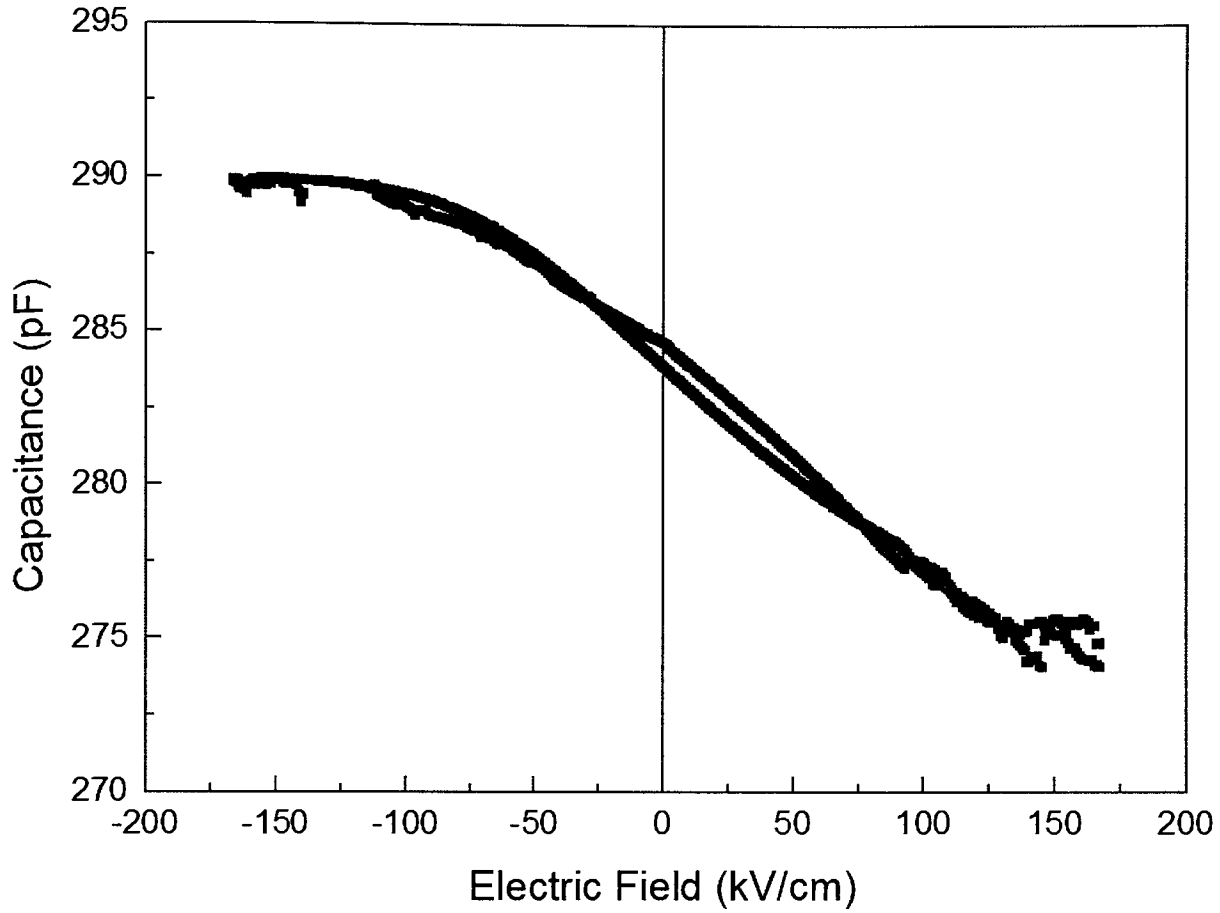

Figure 5-4 Capacitance (C) – Electric Field (E) plot for the BTFC thin films on p-type silicon with ZnO interfaces layers.

The Capacitance-Electric Field plot, shows a curve characteristic of a MOS device, which can be attributed to the p-type semiconductor silicon. Positively charged holes gather at the BTFC barrier during the negative bias, increasing the measured capacitance. However as positive bias is applied, these charges are repelled, decreasing the accumulated charge, and the measured capacitance. The maximum and minimum capacitances measured are 290pF, and 275pF, with the dielectric constant at these values calculate at 135 and 128 respectively, a similar dielectric constant to BTO thin films reported elsewhere (50, 66, 147). A small difference in capacitance depending on the sweeping direction can be seen at E = 0 kV/cm, This can be attributed to SiO_2 charge trappings in the silicon/ZnO interface (148).

To examine the domain switching of the BTFC thin film device, ferroelectric measurements were performed using the ferroelectric testing method described in Chapter 3.3.5. Initial measurements were performed with an electric field of 172kV/cm peak to peak, which was then increased to 362kV/cm peak to peak. The sample broke down when an electric field as high as 400kV/cm was applied. The frequency was fixed at 20Hz for all measurements. The electric field versus time and current versus time (E-t, I-t), current versus electric field (I-E) hysteresis loops and the electrical

displacement versus electric field (D-E) hysteresis loop of BTFC thin films measured at 172kV/cm and 400kV/cm are presented in Figure 5.5 and Figure 5.6 respectively.

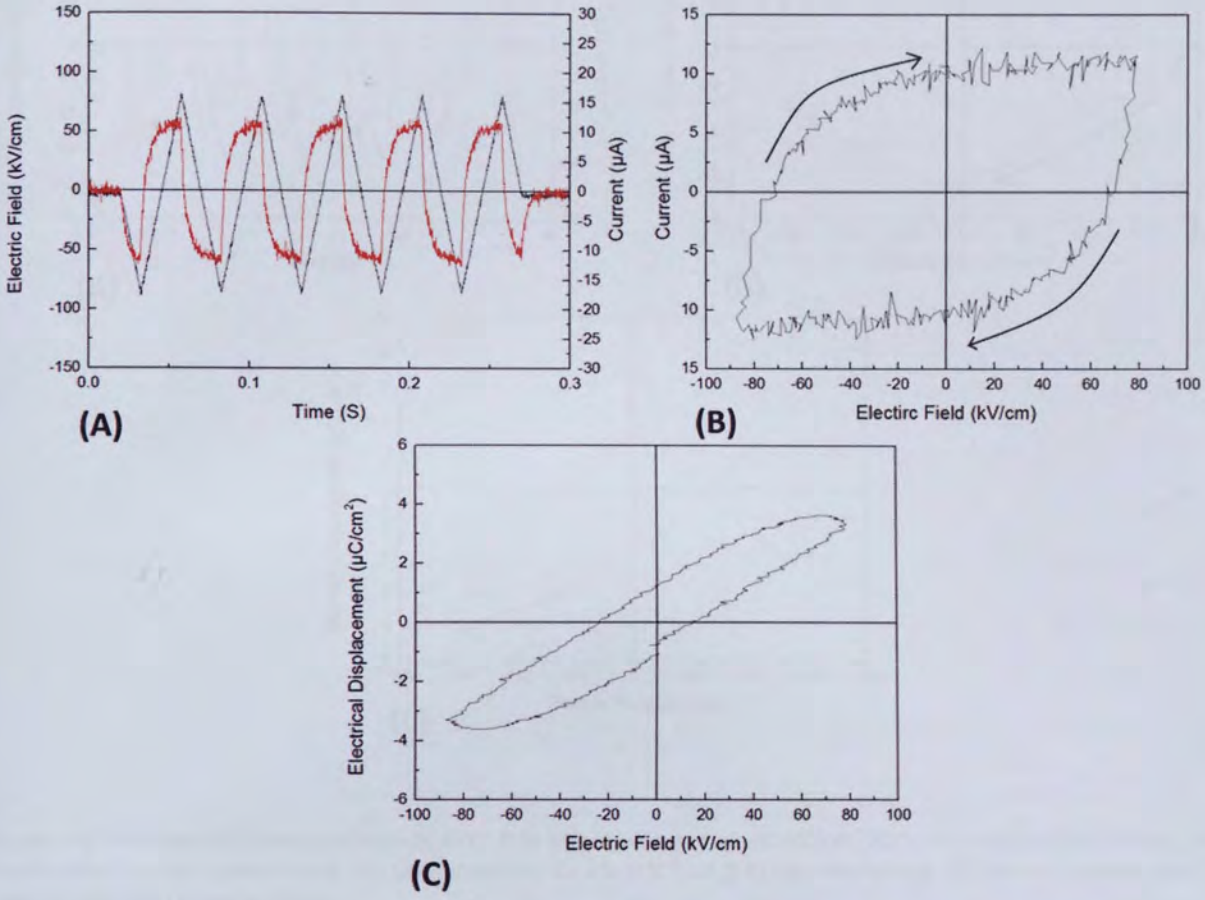

Figure 5-5 Ferroelectric characterisation of BTFC thin films measured at 172kV/cm, 20Hz. (A) Electric field (black) and current (red) versus time (E-t, I-t), (B) Current verses electric field (I-E) hysteresis loop, (C) Electric displacement vs electric field (D-E) hysteresis loop.

The E-t and I-t plot at 172 kV/cm is presented in Figure 5.5.A. The current peak occurs at the same point as the voltage peak, indicating no ferroelectric domain switching. The I-E loop seen in figure 5.5.B shows similar behaviours with the peak current occurring at the maximum applied electric field, again indicating a lack of ferroelectric behaviour. The D-E plot (Figure 5.5.C) shows an hysteresis curve with aa non–zero electric displacement at E=0 characteristic of a ferroelectric material.

In combination with the observed E-t, I-t and I-E curves, the nature of the electric displacement on the D-E curve is likely caused by the combination of leakage current and dielectric effects, rather than ferroelectric domain switching.

In order to stimulate ferroelectric domain switching, the experiment was repeated, but the applied electric field was increased to 362 kV/cm peak to peak, as seen in Figure 5.6.

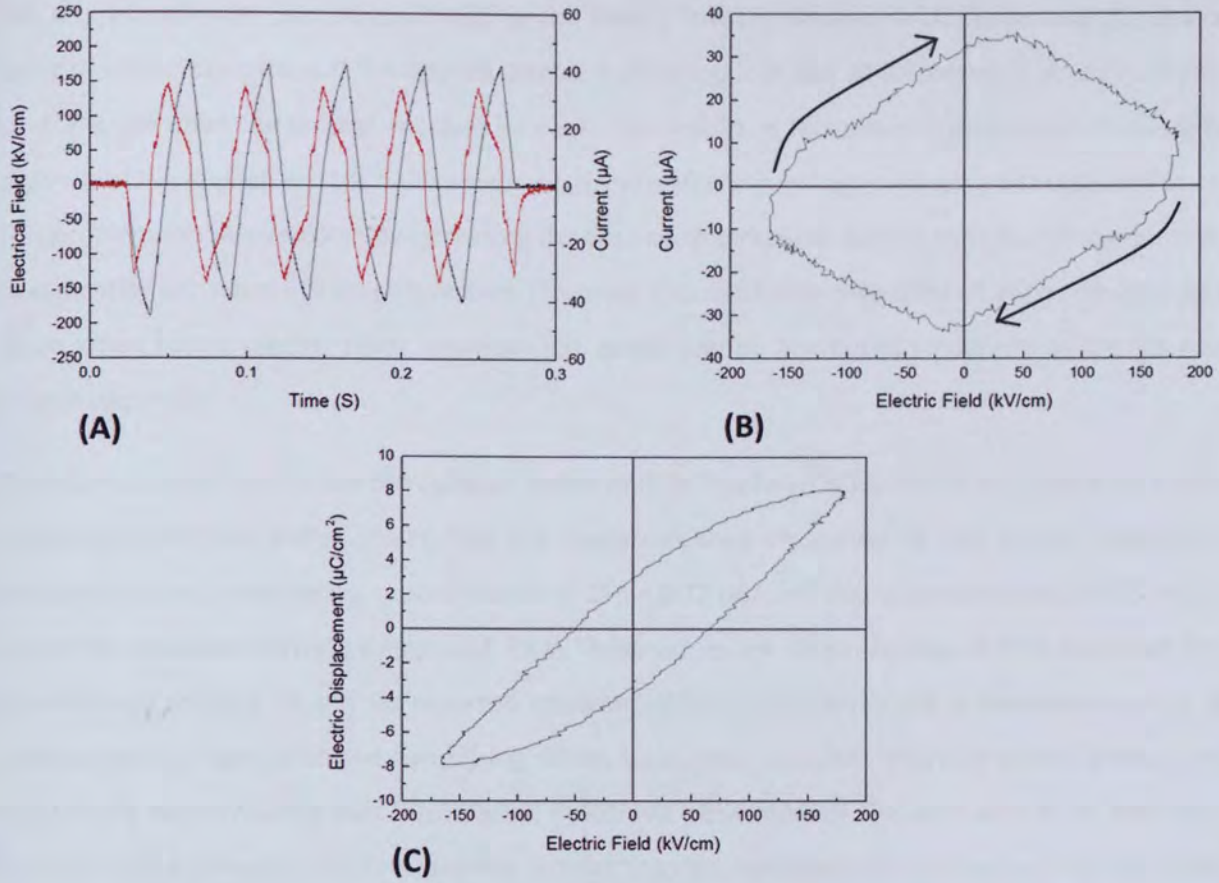

Figure 5-6 Ferroelectric characterisation of BTFC thin films measured at 362kV/cm, 20Hz. (A) (Electric field (black) and current (red) versus time (E-t and I-t), (B) Current verses electric field (I-E) hysteresis loop, (C) Electric displacement vs electric field (D-E) hysteresis loop.

When the electric field is increased to 362 kV/cm peak to peak, the E-t and I-t plot (Figure 5.6.A) presents a distinct current peak leading the electric field peak, indicating ferroelectric domain switching. The current peak itself is notably wide, which is most likely due to the poly crystalline nature of the thin film. The multiple grain like nature of polycrystalline films allows for domains to switch gradually as the voltage rises pass the coercive field, rather than the more spontaneous switching that would occur in a single crystal. From the I-E loop (Figure 5.6.B) the current peak forms after the electric field passes 0 kV/cm, but before the maximum voltage is reached, indicating ferroelectric domain switching.

From the D-E hysteresis loop (Figure 5.6.C) we can see clearly the ferroelectric switching, with a remnant polarisation of $2Pr = 6.72\ \mu C/cm^2$, and a coercive field of $2Ec = 115$ kV/cm. From the shape of the hysteresis curve, we can observe that the electrical displacement continues to increase for a short time after the voltage reaches its maximum value, indicating that the device has not fully saturated.

The lack of saturation can be attributed to the limited low breakdown field, preventing the device being driven to saturation. If the applied electric field is too low, not all ferroelectric domains would have aligned when the voltage reached its peak. This results in ferroelectric domains continuing to align whilst the applied electric field remains high, even after the voltage sweeping direction switched. This problem can be overcome by increasing the applied electric field, forcing all ferroelectric domains to align prior to change in voltage direction. However, this method proves difficult as the device broke down when higher electric fields were applied, which can be attributed to defects in the form of oxygen vacancies.

These results confirm that the ferroelectric phase of BTFC has been achieved by deposition on silicon substrates with ZnO buffer layers. The D-E hysteresis loop measured at 362 kV/cm presents a ferroelectric loop, with remnant polarisation of $2Pr = 6.72\ \mu C/cm^2$, and a coercive field of $2Ec = 115$ kV/cm the equivalent driving voltage of 6.98 V. These values are similar to that of BTFC thin films and ceramics doped with Fe and Co reported elsewhere(68-70, 149) indicating a comparable level of polarisation has been obtained by utilising silicon substrates with ZnO interface layers. It has been successfully demonstrated that ferroelectric hysteresis behaviours of the deposited BTFC thin films forms at high applied electric field, and the non-ferroelectric hysteresis properties occur at low fields.

5.4 Conclusion

Ferroelectric BTFC thin films have been fabricated on silicon substrates using ZnO interface layers. A measured remnant polarisation of $2Pr = 6.72\ \mu C/cm^2$ and coercive field of $2Ec = 115$ kV/cm were similar to that of BTO doped with Fe and Co reported elsewhere, indicating films with comparable properties had been achieved on silicon using a ZnO interface layer. The investigation was limited to samples annealed in vacuum, rather than ambient or oxygen enriched environment, to prevent the oxidisation of the silicon substrates. This leads to the generation of oxygen vacancies in the BTFC thin films, increasing leakage current, and resulting in a low breakdown voltage, preventing the device being driven to saturation during ferroelectric measurements.

Chapter 6 : The Multiferroic Properties of BTFC Thin Films on Platinised Silicon Substrates

6.1 Introduction

As demonstrated in chapters 5, $Bi_4Ti_3O_{12}$ retains its ferroelectric properties after inserting ferromagnetic elements (iron and cobalt) into its Perovskite structure. The study in chapter 5 was carried out on silicon with ZnO interface layers, which leads to the following drawbacks. Firstly, the thin films had to be annealed in a vacuum atmosphere to prevent oxidation of the silicon substrates, which resulted in the generation of oxygen vacancies in the BTFC thin film, leading to a drop in the breakdown voltage and an increase in the leakage current. Secondly, the ZnO layers cannot prevent the diffusion of elements (silicon and zinc) between the substrate, interface and ferroelectric layer under the high temperature annealing process.

To accurately investigate the ferroelectric properties of BTFC thin films, it is important to utilise a substrate possesses the following functionality: 1) to facilitate the growth of Aurivillius phase BTFC, 2) to be chemically and structurally stable at high processing temperatures, 3) and to have metallic conductivity necessary for back electrode contacts.

Ferroelectric materials deposited on $Pt/TiO_2/SiO_2/Si$ substrates are well documented (66, 112, 150). The Pt surface is oxidation resistant, allowing it to maintain its conductivity and smooth surface whilst annealing at high temperatures and in an oxygen rich environment. Moreover, Pt works as an outstanding barrier material, preventing the diffusion of elements between the substrate and thin film(151). The titanium oxide layer works as an adhesive layer between the platinum and silicon. By depositing BTFC onto Pt/TiO2/SiO/Si substrates, we expect to achieve BTFC thin films with good Aurivillius phase crystallinity, minimal substrate/BTFC diffusion and good quality back contacts, allowing accurate characterisation of BTFC ferroelectric and ferromagnetic properties.

This chapter aims to investigate the crystalline structure and the ferroelectric and ferromagnetic properties of BTFC thin films on platinised silicon substrates. The effect of post deposition annealing treatment and deposition time were investigated to determine the optimal conditions to produce the highest quality thin film. Using these findings, the leakage current, dielectric properties, ferroelectric properties, and ferromagnetic properties of the optimal sample were investigated, to determine the optimal processing conditions for BTFC thin films.

The results were compared to that of the same material deposited on silicon with ZnO interfaces to analyse the substrate effect comparison, and against other BTO based materials reported elsewhere to analyse the effect of doping on the ferroelectric and ferromagnetic properties.

6.2 Experimental

BTFC thin films were deposited on platinised silicon substrates by RF magnetron sputtering. The platinised substrates consisted of (100) silicon coated with a surface layer of Pt(150nm)/TiO_2(40nm)/SiO_2 (0.5μ) which were purchased from Vin Karola Instruments. The titanium oxide layer works as an adhesive between the platinum and silicon layers. The platinised silicon substrates were cut up into 1.5cm by 1.5cm pieces and cleaned using the same procedure used for silicon substrates in chapter 4.2. It is noted that the surface top platinum layer is very fragile, and is easily scratched. Extra care should be taken when handling the substrates. After cleaning, with no further treatment, BTFC thin films were deposited directly on top of the platinised substrates following the sputtering method as described in chapter 4.2. After deposition, the films were annealed in an ambient atmosphere using a pre-heated Carbolite CWF 11/23 furnace for 1 hour.

To fabricate devices for electrical measurements, 400 nm BTFC was deposited onto platinised silicon, with a region of the substrate surface left exposed to form an electrical contact. The sample was then annealed at 650^{o}C for 1 hour in an ambient atmosphere. After annealing, 430 μm wide gold dots were deposited onto the BTFC surface to act as top contacts utilising a faster, newly purchased Moorfield thermal evaporator. To perform ferromagnetic measurements 400nm BTFC thin films were deposited onto platinised silicon, covering the entire surface, and then annealed at 650^{o}C in an ambient atmosphere to crystallise. The samples were then mechanically cut into 3.5mm x3.5mm pieces. No further treatment was performed. Two or more samples where utilised in each measurement.

BTFC Thin film crystal structure was characterised by XRD using a Bruker d8 utilising CuKa1 radiation with a wavelength 1.57 Å. Leakage current and capacitance-voltage measurements were carried out using a Keithley 4200 Semiconductor Analyser. Ferroelectricity properties were measured using the triangular voltage waveform method, and ferromagnetism was characterised using a Quantum Design MPMS-S5 SQUID Magnetometer at 5 kelvin.

6.3 Results and Discussion

The effect of annealing temperature on the crystallinity of BTFC thin films was investigated. BTFC thin films were deposited on Pt/TiO_2/SiO_2/Si substrate by RF magnetron sputtering. As the sputtering rate of BTFC on platinum was initially unknown, thin films were deposited for 196 minutes, the time taken to acquire 300nm BTFC thin films when depositing on silicon with ZnO interface layers using the same sputtering conditions. The XRD of BTFC deposited on platinum and annealed in ambient atmospheres for one hour at 500^{o}C, 600^{o}C, 650^{o}C, 700^{o}C and 750^{o}C are presented in figure 6.1.

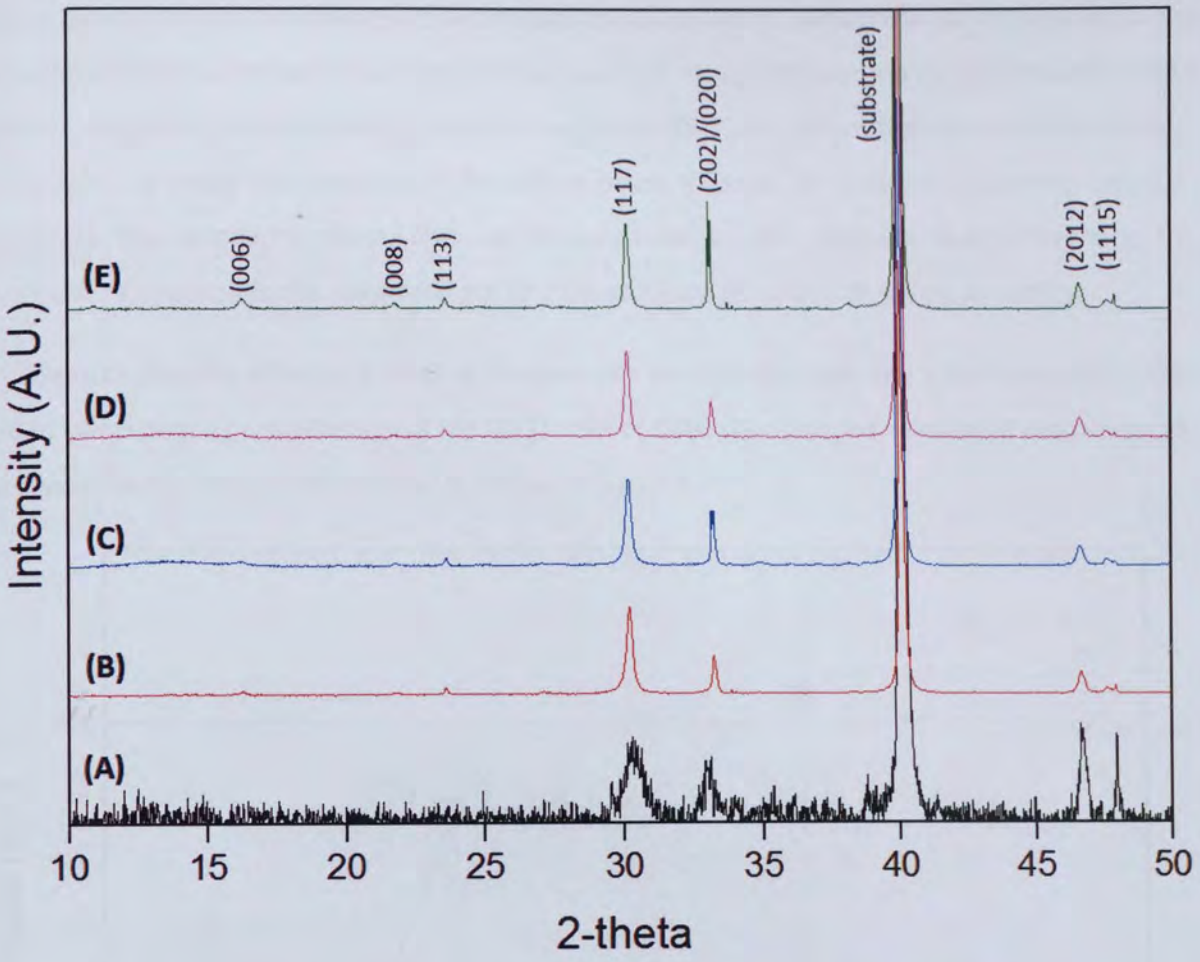

Figure 6-1 XRD of BTFC thin films deposited on platinum and annealed at different temperatures. Thin films annealed at (A) 550°C, (B) 600°C, (C) 650°C, (D) 700°C, (E) 750°C.

The intense peak seen at 2-theta = 40° can be attributed to the platinised substrate. All BTFC thin films are predominantly Aurivillius in phase, as indicated by the (006), (008), (113), (117), (2012) and (1115) orientations. BTFC thin films annealed at 550°C show significantly broader peaks than other samples, indicating that the thin film crystallinity improves significantly at 600°C or above.

Visible inspection of the films show a mirror like reflection for samples annealed at 650°C and below, were-as films annealed at above 650°C do not accurately reflect images, indicating a diffuse type reflection. The specular type reflection is evident of a smooth platinum surface through the BTFC thin film, were-as the diffuse type reflection is evidence of a rough platinum surface. The rough surface can be attributed to the migration of titanium atoms in the adhesive layer into the platinum at high temperatures(152).

We can deduce that as the BTFC thin film is transparent, the type of reflection indicates the surface state of the platinum, with the specular type indicating a smooth surface, and the diffuse type reflection indicating a rough surface. The supplier of the platinised substrates warned that platinum

surface would become roughened at temperatures above 700°C, which can be attributed to the migration of the titanium adhesive layer into the platinum at high temperatures. This provides useful guidance, suggesting the annealing temperatures below 700°C to prevent the substrate roughening. Additionally, no peaks characteristic of Pyrochlore phase BTO can be detected, indicating platinum suppresses this secondary phase. This can be explained by the platinum layer preventing the absorption of oxygen into the substrate, limiting the emission of volatile Bi during annealing.

To closer examine the effect of annealing temperature on crystallite size, the Scherrer equation was used to calculate the crystallite size of the (117) peak of BTFC thin films annealed at all temperatures. The crystallite size versus temperature is plotted in figure 6.2.

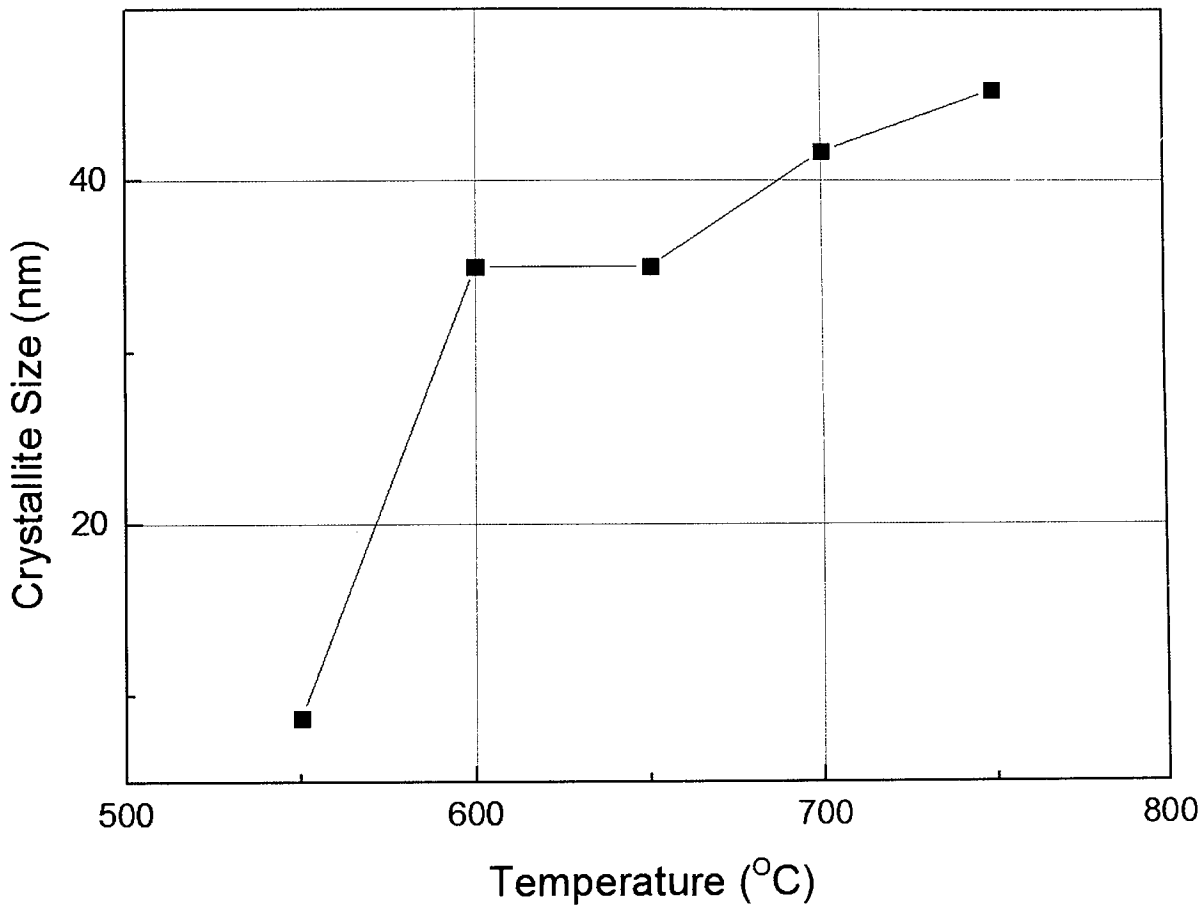

Figure 6-2 The crystallite size of the (117) plane for BTFC thin films deposited on platinised substrates and annealed at different temperatures.

The plot shows crystallite size increasing with annealing temperature for films annealed between 600°C and 750°C, with the largest crystallite size being 45nm at 750°C, and the smallest being 35nm at 600 and 650°C. The crystallite size for BTFC annealed at 550°C is significantly smaller than other temperatures. This can be explained by 550°C being the critical temperature for the formation of

Aurivillius phase BTO reported elsewhere(58). Higher temperatures or energy is needed to facilitate the crystalline growth of the BTFC thin films.

As discussed previously in section 3.3.1.1. The Scherrer equations does not take into account variation in the Bragg angle due to deviations in the inter plane spacing because of changes in internal strain. By looking at the peak location, we observe that the peak location is constantly at 30.19^{o}, indicating that there is no change in strain over the range of annealing temperatures, and no resulting error in the Scherrer equation.

These results suggest that BTFC thin films annealed at $600^{o}C$ and $650^{o}C$ are the best candidate for further investigations, based on the thermal stability of the platinum, and the crystallinity of the BTFC. Wu et al(56) investigated the effect of substrate temperature on Praseodymium doped BTO thin films deposited by rf-magnetron sputtering on platinised substrates. They found a big improvement in the ferroelectric properties when the temperature was increased from $600^{o}C$ to $650^{o}C$, which they attributed to the improved crystallinity. Whilst we are unable to determine any distinct difference in crystallinity between 600 and $650^{o}C$, we have chosen to use BTFC thin films annealed at $650^{o}C$ for future investigations, based on the Wu et al's findings.

After determining the optimal annealing temperature, the next stage of the investigation is to accurately determine the deposition rate, and to look at the effect of film thickness on the crystallinity. To achieve this, BTFC thin films were deposited on platinised substrates using the same deposition conditions, but with the deposition time varied from 240 minutes, 196 minutes, 120 minutes and 60 minutes followed by annealing at $650^{o}C$ in ambient atmosphere for 1 hour. The cross-sectional SEM of BTFC thin films is shown in figure 6.3.

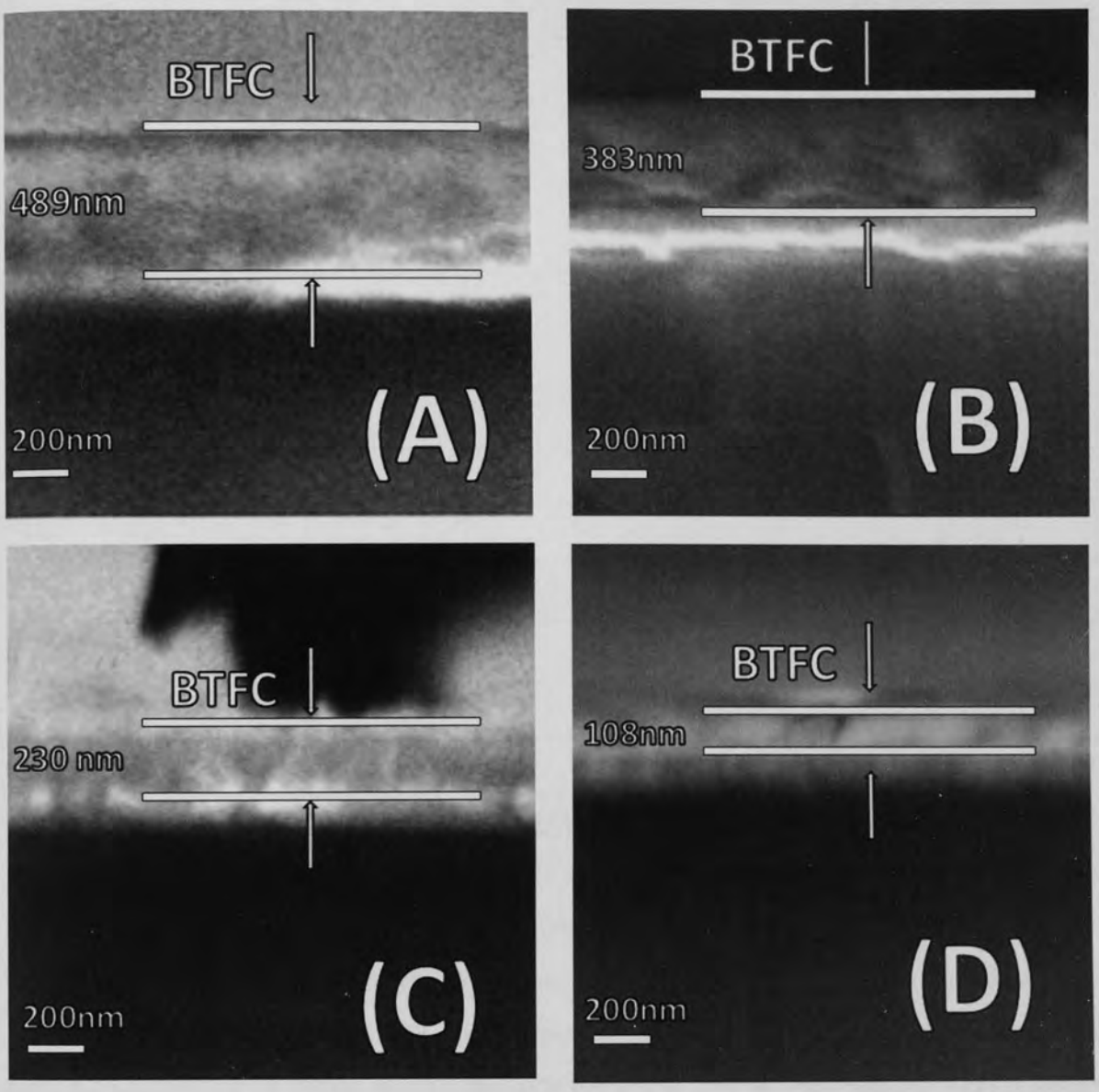

Figure 6-3 Cross sectional area of BTFC thin films deposited for (A) 240 minutes, (B) 196 minutes, (C) 120 minutes, (D) 60 minutes. All samples annealed for 1 hour in ambient atmosphere at 650^{o}C

All images are orientated such that the platinised substrate is below the ferroelectric layer. The bright region separating the thin film and substrate is the highly conductive, 150nm thick platinum layer. In Figures 6.3.A and 6.3.D a blurry region of space can be seen above the BTFC layer, this results from the SEM detecting the clamp, holding the sample upright. Additionally, Figure 6.3.C presents signs of surface debris on the BTFC surface. The cross-sectional images of BTFC deposited for 240, 196, 120 and 60 minutes' present thicknesses measured at 383nm 230nm, 108nm and 70nm respectively. The deposition time vs film thickness is plotted in figure 6.4.

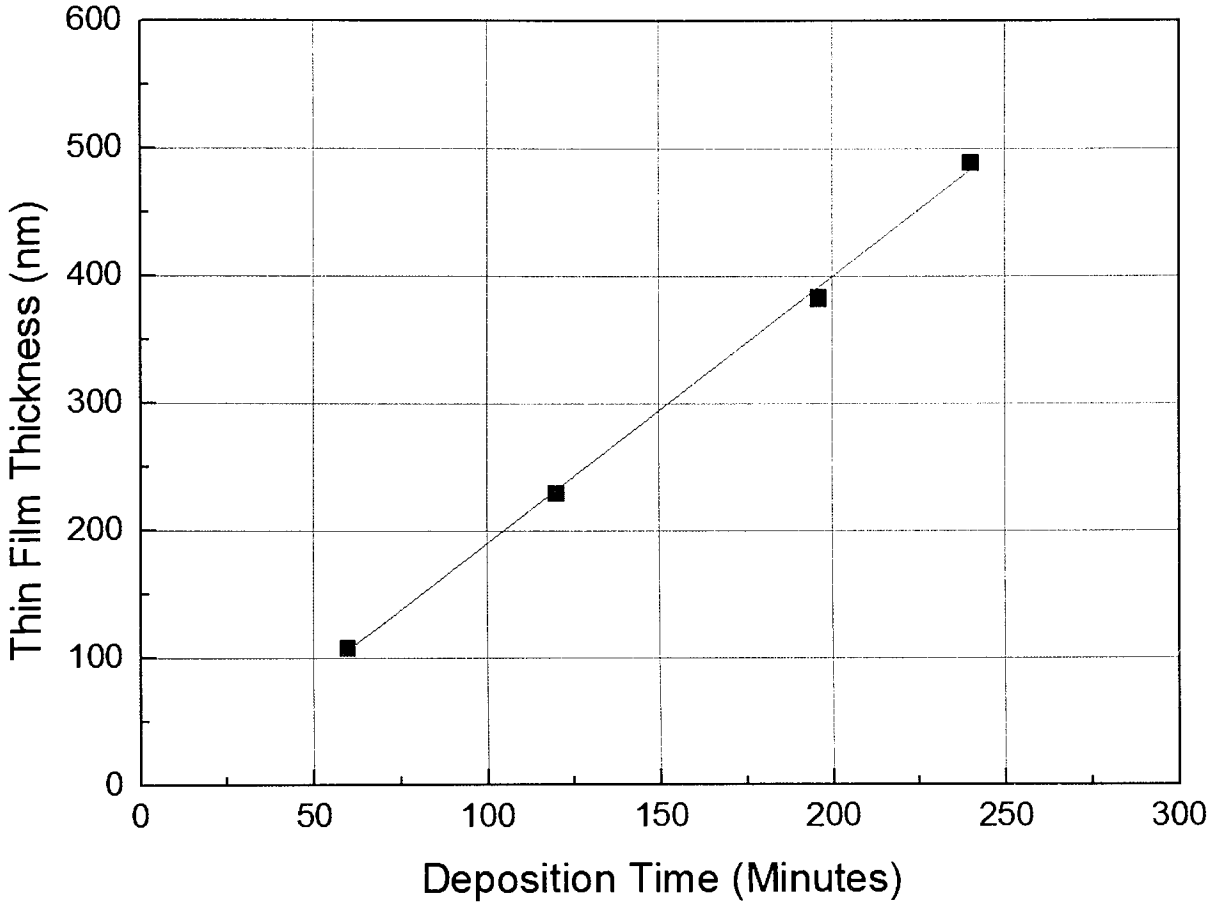

Figure 6-4 Plot of deposition time (minutes) vs Thin Film thickness (nm) for BTFC on Pt/Si Substrates

The relationship between the plots is highly linear. From the line of best fit, we can determine that the deposition rate is 2.1nm/min. This slow deposition rate is beneficial, as it allows us to produce thin films with accurate thicknesses. By extrapolating the line of best fit, the Y-axis intercept is calculated at -20nm. This indicates that the initial deposition rate after time = 0 is lower than that after 60 minutes.

To analyse the effect of deposition time on crystallinity, the samples were investigated by XRD. Figure 6.5 presents the XRD pattern of BTFC thin films deposited for 60, 120, 196 and 240 minutes.

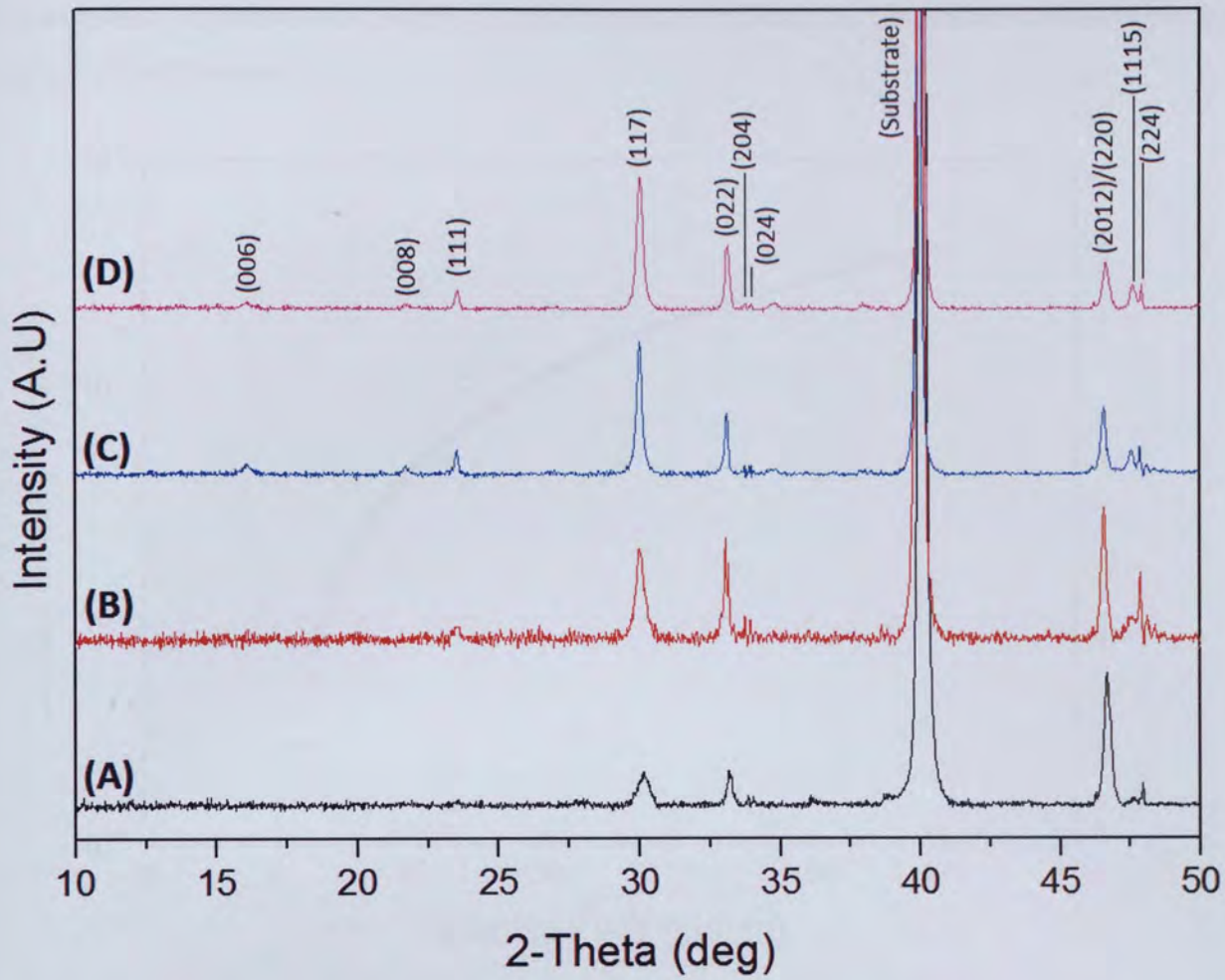

Figure 6-5 X-ray diffraction pattern of BTFC deposited for (A) 60 minutes, (B), 120 Minutes, (C) 196 Minutes and (D) 240 minutes.

The plot for BTFC deposited for 60, 120, 196 and 240 minutes is presented in figure 6.5.A, 6.5.B, 6.5.C and 6.5.D respectively. The intense peak located at 2-theta = 40^{O} can be attributed to the strong platinum substrate reflection. All films present Aurivillius diffraction patterns with Aurivillius phase (006), (008), (111), (117), (022), (204), (024),overlapping (2012)/(220), (1115) and (224) orientations present. The ratio of the XRD peak intensity between the peak (117) and (022) increases with the increase with film thickness. It is expected that the thicker the films, the better the ferroelectric properties of the non-c-axis- (117) orientation is the preferred crystal orientation to maximise the dipole switching within ferroelectric domains (49).

To investigate the electronic and ferroelectric properties of BTFC, thin films were deposited onto platinised silicon. The deposited thin film thickness was 400nm and was annealed at $650^{O}C$ for 1 hour in ambient atmosphere. Gold dots were deposited directly onto the BTFC surface to act as top contacts, and back contact was achieved by connecting the probes directly the platinum surface. The crystallinity, leakage current, capacitance-voltage (C-V) relationship and ferroelectric properties were

investigated. All measurements were performed at room temperature. The leakage current vs electric field is plotted in figure 6.6.

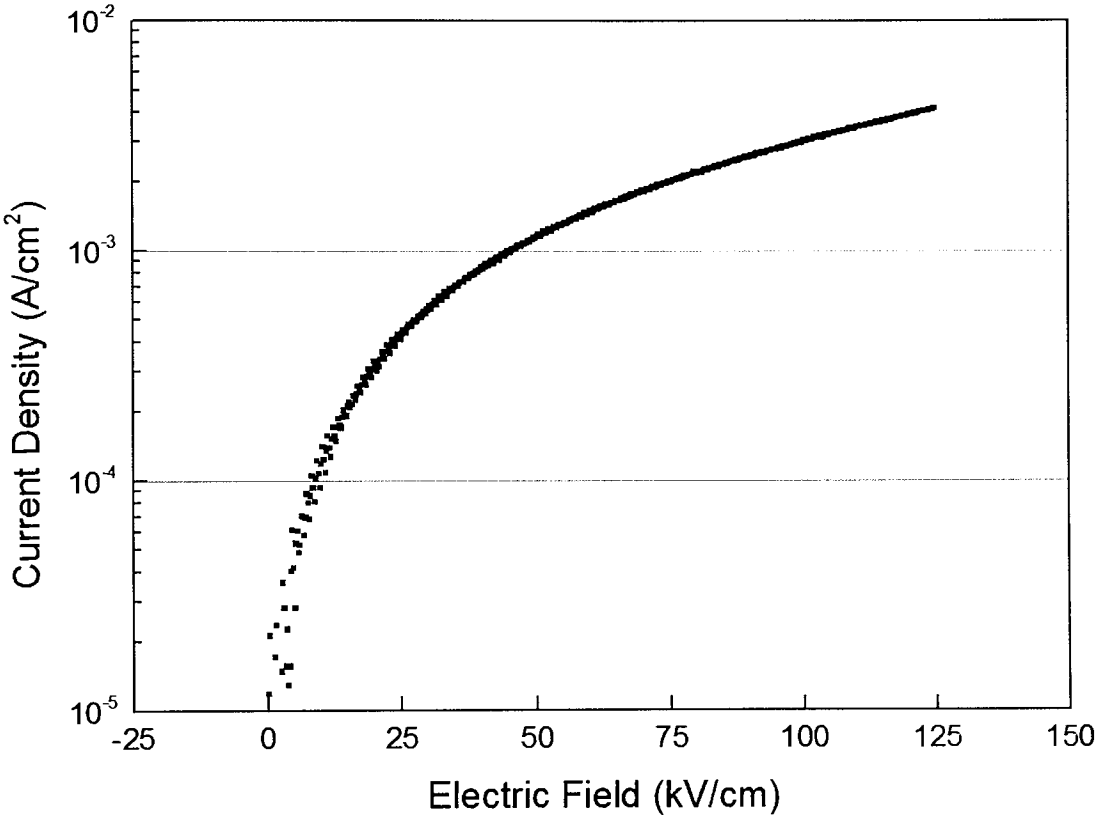

Figure 6-6 Leakage Current behaviour of BTFC thin films on platinised silicon.

Leakage current is presented by plotting the applied electric field against the current density. The maximum applied electric field of 125 kV/cm equates to an applied voltage of 5V. The leakage current at an applied electric field of 125, 100 75 and 50 kV/cm is equal to 4.19, 2.98, 2.01, 1.15mA/cm^2, respectivly.

This level of leakage current is similar to that of iron and cobalt doped BTO reported by Raghavan et al(88). The current density is, however, larger than that reported in BTO without iron and cobalt doping (112, 153). The leakage current is comparable to that of BTFC on silicon using ZnO interfaces, previously reported in Chapter 5. As our results are silmilar to that of BTO doped with iron and cobalt reported by Raghavan et al, we can speculate that the high current is most likely due to a doping effect.

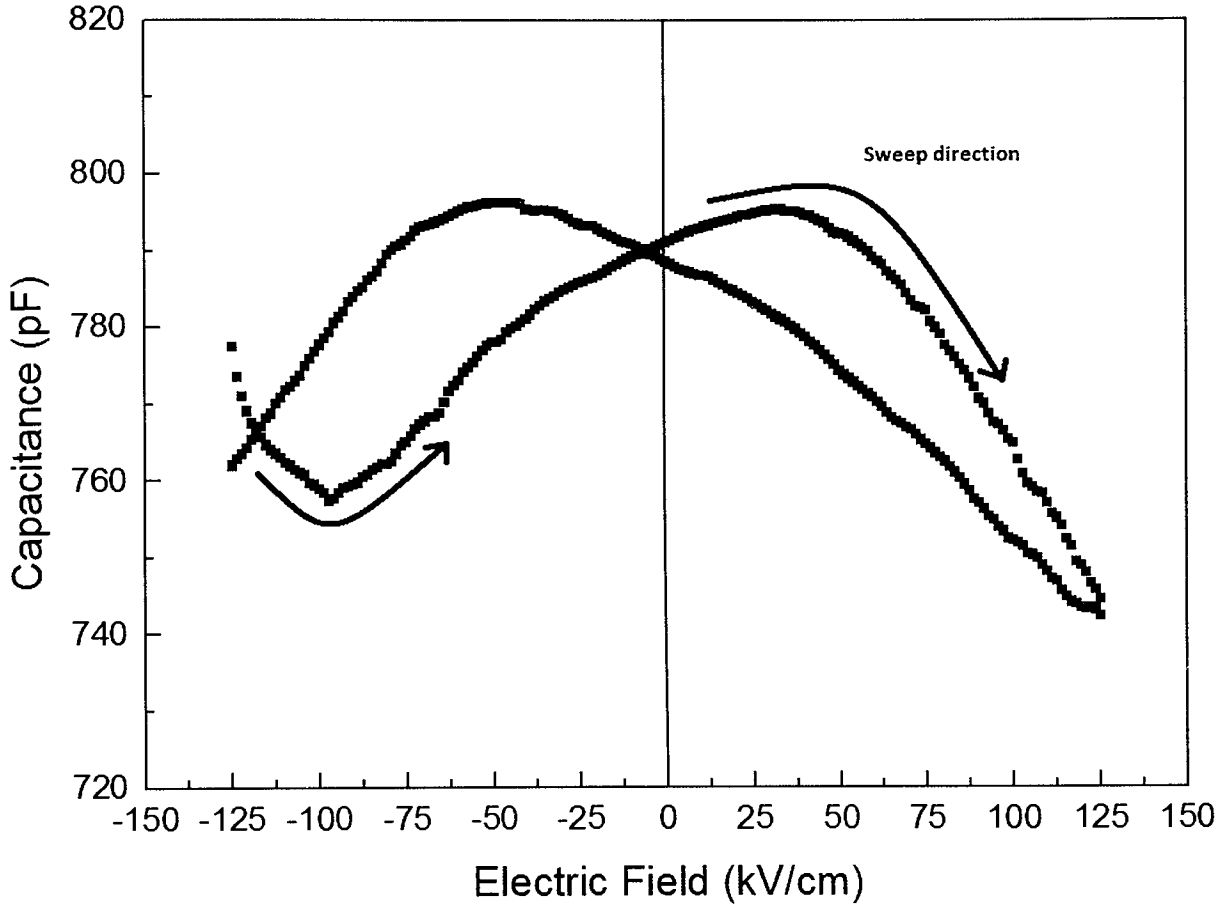

Figure 6-7 Capacitance – Voltage behaviour of BTFC thin films on platinised silicon.

Figure 6.7 presents the C-V behaviour of 400nm BTFC on platinised silicon. Measurements were performed by sweeping the DC Bias electric field from -125kV/cm to +125kV/cm and back again, whilst a measuring signal of $30mV_{rms}$ with a frequency of 1MHz is applied. The relationship shows a twin peak pattern, indicative of a metal-ferroelectric-metal structure(154). The capacitance peaks can be attributed to the ferroelectric switching occurring as the DC bias passes the coercive field(155). The dielectric constant, measured at the peak capacitance of 795pF is calculated as 246.7. This is notably higher than that of undoped BTO(50, 147) but is similar to the large dielectric constant reported in niobium and iron doped BTO elsewhere(156, 157), where the increase in dielectric constant can be attributed to the large atomic radius of niobium and iron distorting the TiO_6 octahedron, allowing for greater dipole moment within the structure.

To characterise the ferroelectric properties, the domain switching was characterised using ferroelectric testing method described in chapter 3.3.7. Measurements were performed using a triangular wave with a frequency of 100Hz, and a voltage of 35V peak to peak which was equal to an electric field of 860kV/cm peak to peak. The applied waveform voltage itself is asymmetrical, with

peak electric fields of 410 kV/cm and -437kV/cm. The effect of this error will be involved in the discussion.

The plots for the electric field versus time (E-t) and current versus time (I-t), Current versus electric field (I-E), and electric displacement versus electric field (D-E) are presented in figures 6.8.

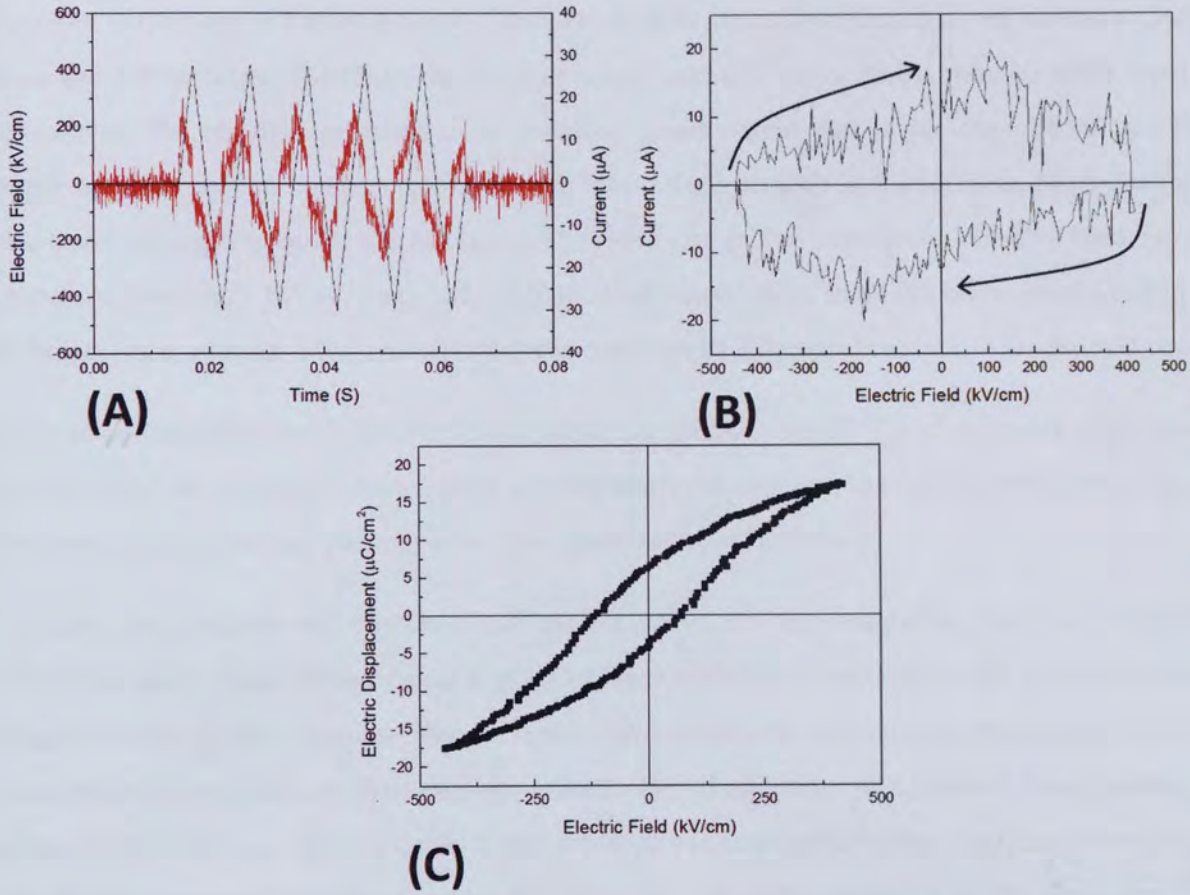

Figure 6-8 Ferroelectric characterisation of BTFC thin films measured at 35Vpeak to peak, 100Hz. (A) (E-t) Electric field versus time (black) and current versus time (red) versus time (C)(I-E) current verses electric field hysteresis loop, (C) (D-E) electric displacement vs electric field hysteresis loop.

Figure 6.8.A shows the E-t and I-t relationship. A clearly defined current peak leading the voltage peak is present, indicating ferroelectric switching. The current peak forms at 105 kV/cm in the positive switching cycle, and -168 kV/cm in the negative cycle. This difference in current peak locations is most likely due to the asymmetry AC bias voltage. However, to determine if there was any contribution from an electrode effect, the reading was repeated with the probes switched, switching the electrode contact with the measurement system. Repeated measurements found no significant change in the peak current values or location, suggesting that this is an effect of the measurement system, rather than the sample itself.

Figure 6.8.B presents the (I-E) plot, which presents current peaks located after E = 0kV/cm, indicating ferroelectric switching. The D-E plot is presented in figure 6.8.C, which shows a fully saturated hysteresis loop with 2Pr = 11.03 $\mu C/cm^2$, and 2Ec = 196.5 kV/cm^2. The displacement immediately begins to decrease when the voltage switches direction, indicating the loop has fully polarised at 430 kV/cm. Further measurements were performed with a measuring signal of 40V peak to peak, which resulted in the sample breaking down. The coercive field and polarisation are very similar to that of iron and coblat doped $Bi_5FeTi_3O_{15}$ bulk materials(68) and $Bi_6Fe_{1.5}Co_{0.5}Ti_3O_{18}$ thin films(70) reported elsewhere. The remnant polarisation is, however, smaller than that of Nb doped BTO thin films reported by Singh(61). Compared to BTFC thin films on silicon with ZnO interfaces, the polarisation has been improved from 2Pr = 6.722 $\mu C/cm^2$ to 2Pr=11.03 $\mu C/cm^2$, whilst the coercive field has also increased from 2Ec = 115 kV/cm to 196.5 kV/cm. Additionally, BTFC thin films on platinised silicon are fully saturated, whereas BTFC on ZnO interfaces could not be fully saturated before breakdown occurs.

To conclude the ferroelectric findings, the ferroelectric properties of BTFC is comparable to that found in BTO with iron and cobalt doping reported elsewhere. In addition, the ferroelectric properties are improved using platinised silicon, rather than silicon with ZnO interfaces.

To determine if multiferroic thin films have been achieved, the ferromagnetic properties of the BTFC thin films were characterised using a SQUID Magnetometer to determine the magnetisation vs magnetic field (M-H) response. The same samples used in the ferroelectric measurements were charatcerised. Samples were prepared by mechanically cutting them into 3.5mm x 3.5mm pieces small enough to fit in the sample holder. As it was impossible to separate the thin film from the substrate, the M-H response of both the thin film and substrate had to be measured at the same time. This results in the thin films magnetic response being superimposed upon the substrates response. To compensate for this, a 3.5mm x 3.5mm piece of identical substrate had its magnetic response characterised independently. Knowing the substrates M-H response, it was possible to subtract it from the measured response of the BTFC on the platinised substrate, allowing us to more accurately determine the thin film magnetic properties. For reference, a piece of the sputtering target was also investigated.

The samples were handled using plastic tweezers only, to prevent the transference of metallic particles from the metal tweezers to the sample. All measurements were performed with the magnetic field in plane to the thin film, and at temperatures of 5 kelvin.

The MvH properties of the bulk BTFC target demonstrated presented in figure 6.9, and figure 6.10 presents the same figured with the magnetic field range limited to +4KOe and -4KOe in order to better

analyse the coercive field and remnant magnetisation. Magnetisation is presented in memu/g, for better comparison with other bulk samples.

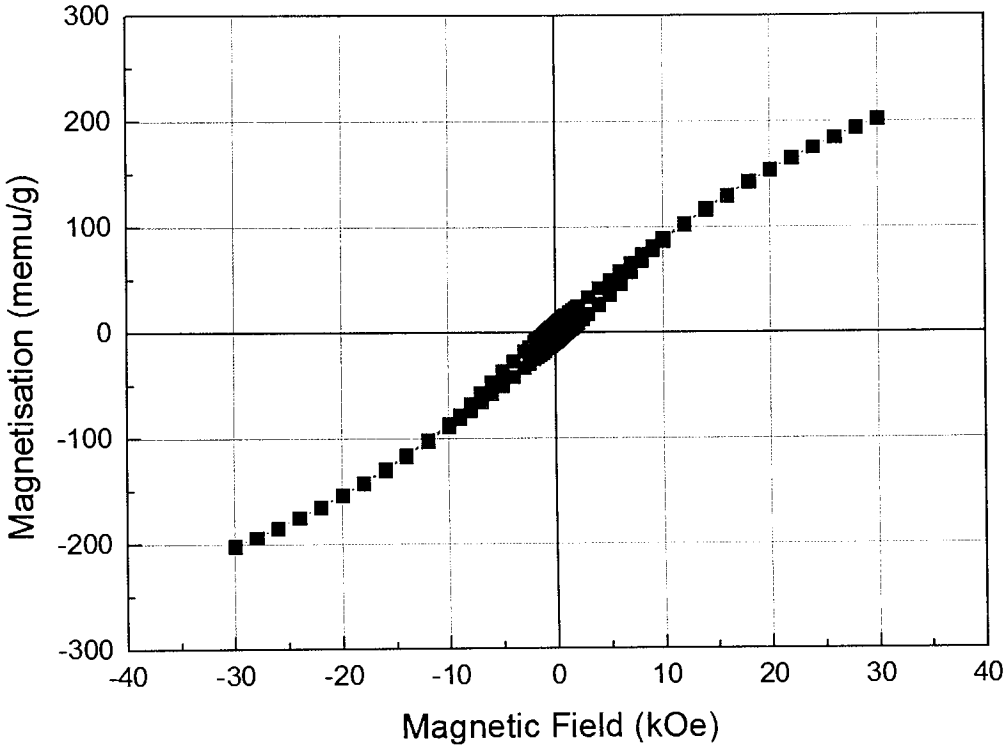

Figure 6-9 The magnetisation (M) versus magnetic field (H) response for the bulk BTFC target.

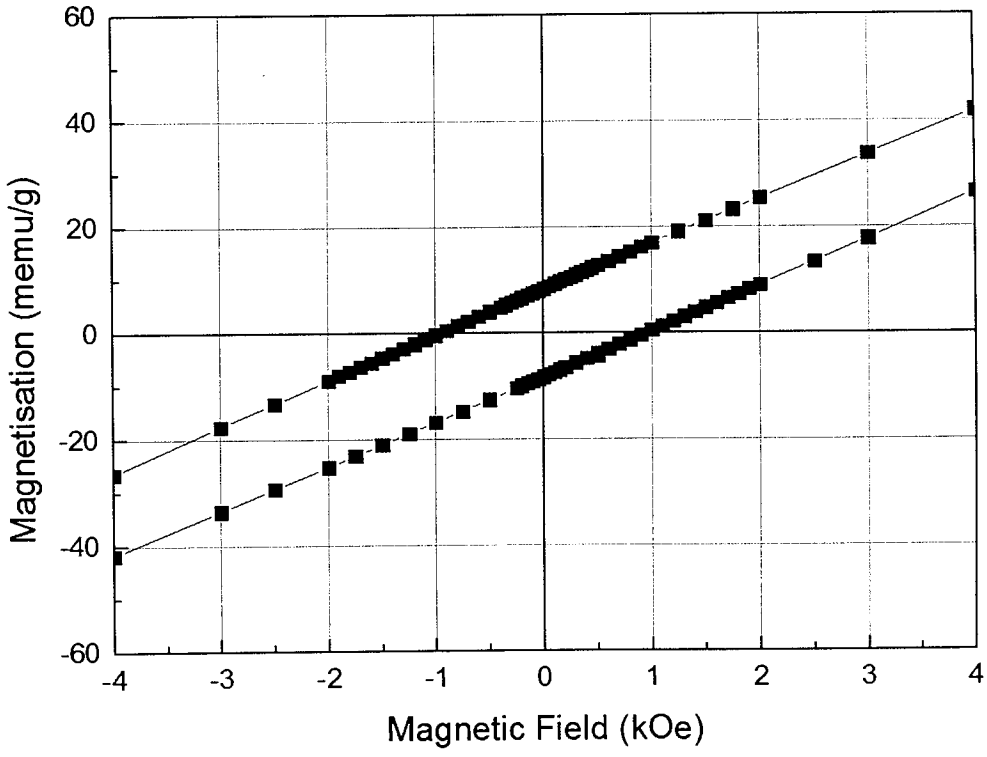

Figure 6-10 The magnetisation (M) versus magnetic field (H) response for the bulk BTFC target, zoomed in between H = -4K and 4KOe.

The curve shows a non-saturated ferromagnetic loop, with a remnant magnetisation and coercive field of 2Mr= 16.6 memu/g and 2Hc= 1.9KOe. These results are very similar to that of $Bi_5Ti_3Fe_{0.5}Co_{0.5}O_{15}$, reported by Mao et al(68), who reported a 2Mr of 7.8 memu/g and a 2Hc of 410Oe in the bulk form.

Figure 6.11 shows the MvH behaviours of the platinised silicon substrate.

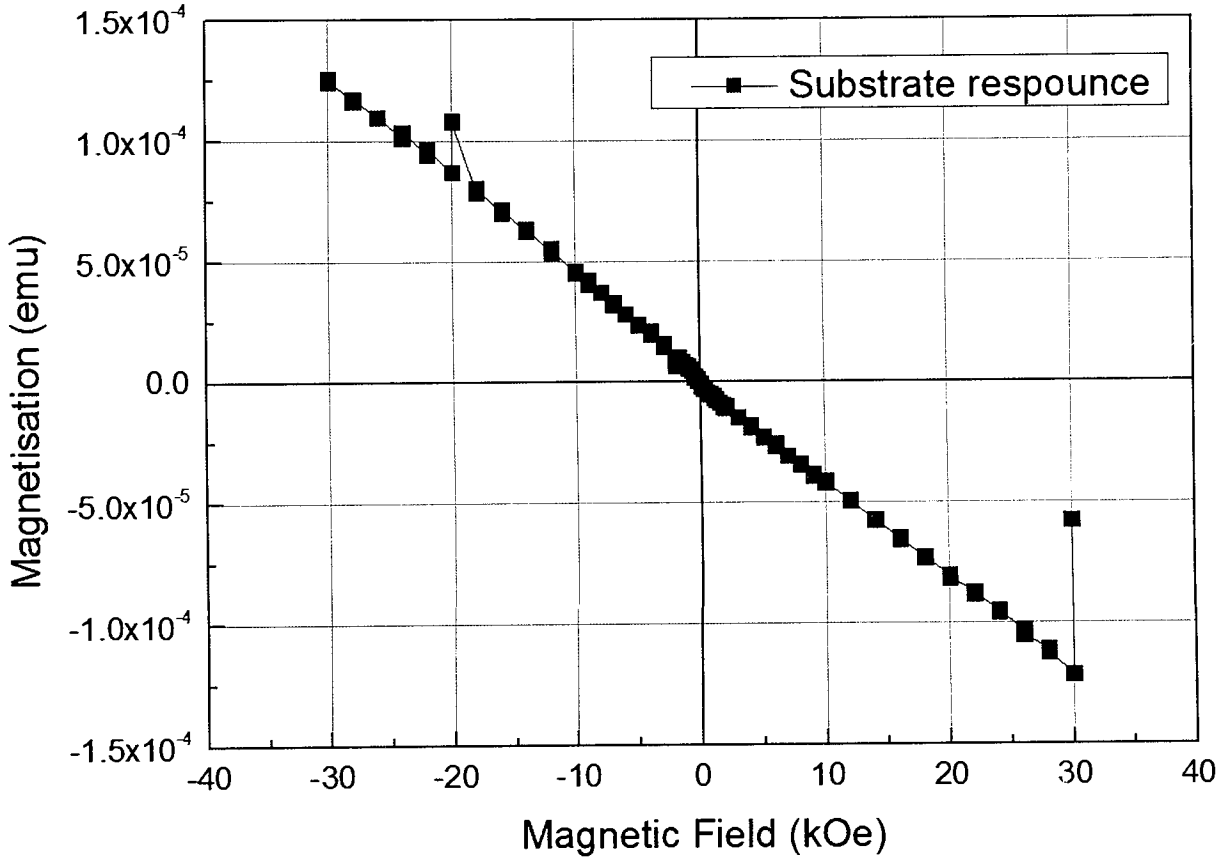

Figure 6-11 The magnetisation (M) versus magnetic field (H) response for the platinised silicon substrate.

The substrate response shows an inversely linear behaviour, characteristic of diamagnetism. This can be attributed to the bulk of the substrate being silicon, which is known to be diamagnetic(158).

Figure 6.12 shows the full MvH response of the platinum coated silicon substrate with the BTFC thin film in red, and the same reading with the substrate subtracted in black.

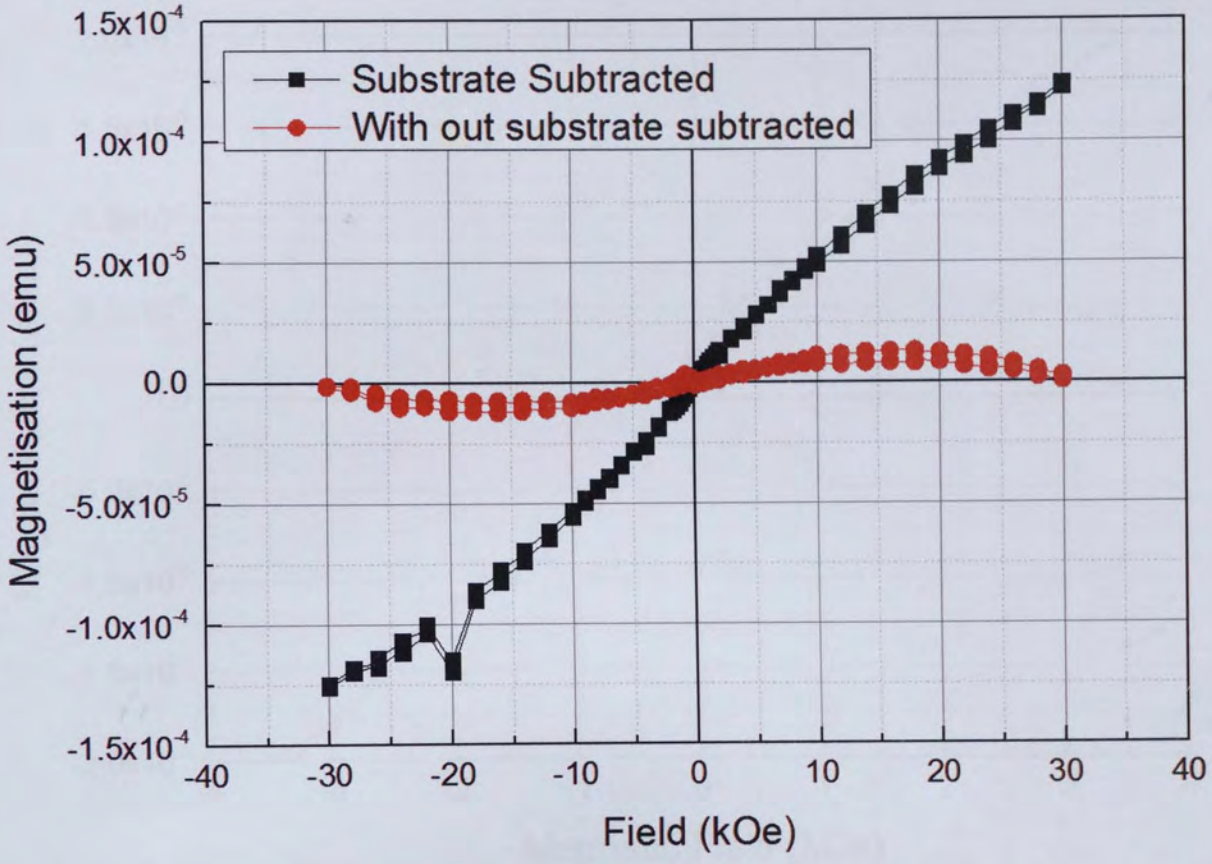

Figure 6-12 The magnetisation (M) versus magnetic field (H) response for the BTFC coated platinised silicon (Red circles) and the BTFC coated platinised silicon with the substrate subtracted (black squares).

The MvH behaviour of the sample without the substrate subtracted is that of a tilted ferromagnetic, due to the substrates diamagnetic behaviour superimposing upon the thin film ferromagnetic response. In comparison, the reading with the substrate subtracted is that of a ferromagnetic, with a curve shape like that of the bulk, as BTFC seen in figure 6.9. A zoom in of the curve with the substrate subtracted is shown in figure 6.13, to better analyse the remnant magnetisation.

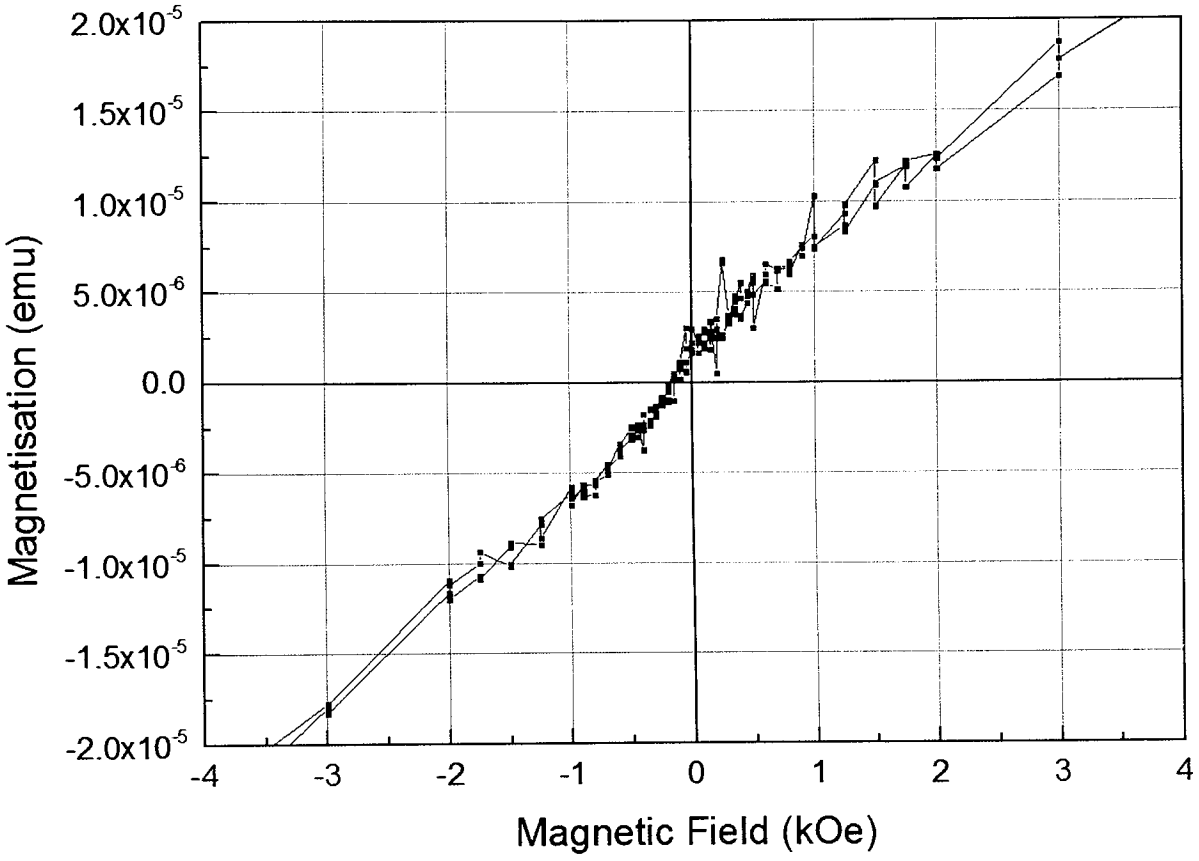

Figure 6-13 The magnetisation (M) versus magnetic field (H) response for the BTFC coated platinised silicon with the substrate subtracted , zoomed in between -4K and +4KOe.

No detectable remnant magnetisation can be seen for BTFC thin films with the substrate subtracted. This can be attributed to the noise dominating the readings at such low magnetisation values.

The bulk BTFC clearly demonstrates ferromagnetic behaviour, with a remnant polarisation similar to that of other bulk BTO samples doped with iron and cobalt reported elsewhere(68). The MvH curve of the thin film form, once the substrate has been subtracted, presents a similar shaped curve, however, the total remnant magnetisation cannot be measured, due to the small total response being out of the apparatus sensitivity range. The similarity between the ferromagnetic loops of the bulk and thin film suggests a similar magnetic behaviour indicating that the thin film form likely presents ferromagnetism, despite not being able to detect the remnant magnetisation due to the noise level signal. Further investigations are needed in which thicker BTFC thin films are utilised, as a thicker film would allow us to increase the total magnetisation of the sample to a detectable level, without adjusting the doping concentrations.

We can conclude that the insertion of iron and cobalt, in addition to lanthanum and niobium dopants into BTO thin films, produces ferromagnetic properties despite the remnant magnetisation not being measurable, due to the noise level reading. The reason for the appearance of ferromagnetism in BTO

thin films with iron and cobalt doping is still debated. BTO doped with iron alone has been reported to present weaker ferromagnetism than samples doped with both iron and cobalt (68, 88). One theory as to why this is is the insertion of Fe and Co results in the possibility of Fe-O and Co-O octahedrons being located near one another in the Perovskite slab, leading to direct Fe-O-Co Magnetic coupling which possibly favours the ferromagnetism (68, 69).

A more recent theory(70, 159), is that due to the different radius of Fe and Co ions, inserting these elements into the Perovskite cubic structure would induce structural distortion. The structural distortion would result in a canted spin state, which would promote ferromagnetism (70, 159).

It is possible that increased structural distortion of the Perovskite layer through Nb doping in BTFC is enhancing the ferromagnetism, this would occur due to its large ion size distorting the perovskite structure, increasing the tilting of the Fe and Co ions. Further investigation is needed in which the ferromagnetism of the thin film is studied as the concentration of Nb is varied and the levels of iron and cobalt are kept constant, to determine if Nb dopants has any effect on the magnetisation of the thin film.

6.4 Conclusions

BTFC thin films have been deposited on platinised coated silicon substrates. The optimal annealing temperature in ambient atmosphere was determined to be 650^{o}C, and the optimal thickness was around 400nm. Thin films showed higher leakage current than undoped BTO thin films and larger dielectric constants. A fully saturated ferroelectric loop was achieved, with a remnant polarisation and electric coercive field of 2Pr = 11.03 $\mu C/cm^2$, and Ec = 196.5 kV/cm^2. The Ferromagnetic measurements demonstrated ferromagnetism in the bulk form, with 2Mr = 16.6 memu/g and 2Hc= 1.9KOe, which is similar to that of BTO doped with iron and cobalt reported elsewhere. The investigation however was unable to confirm ferromagnetism in the thin film form. The thin film form presents a ferromagnetic curve like that of the bulk sample, however the remnant magnetisation was not above noise level, making it unmeasurable. Further investigations are needed with thicker BTFC thin films, to accurately characterise the ferromagnetism of the thin film.

Chapter 7 : General Discussions for Future Work

This work has investigated two major fields. First was the integration of BTFC thin films on P-type silicon using ZnO interface layer, and second the multiferroic properties of BTFC thin films on platinised silicon substrates. However further investigations are required in both fields.

All BTFC and ZnO thin films were deposited in a pure argon atmosphere. Typically, when oxide thin films are deposited by magnetron sputtering, Ar/O_2 mixed atmospheres are utilised, which increases the oxide content of the deposited thin film. The use of an Ar/O_2 gas however was not possible in this investigation, due to the danger of ozone forming in the cyropump that generates the working vacuum. The investigation into the BTFC deposition of platinum, and the deposition of BTFC on silicon with ZnO interface layers, would benefit from further research, in which oxygen and argon gas mixtures is utilised, to determine the effect of the Ar/O2 mix ratio on the crystallinity of deposited films.

Concerning the investigation into the multiferroic properties of iron and cobalt doped BTO thin films, BTFC thin films deposited on platinised silicon present good ferroelectric behaviours, however the ferromagnetism could not be accurately measured, due to the small sample size. The next immediate investigation needed is the confirmation of the ferromagnetic remnant magnetisation by producing a thin film with a larger magnetisation reading. This can be achieved by sputtering both a thicker film, as doubling the thickness would double to total measured remnant magnetisation, or by increasing the iron to cobalt doping concentration within the thin film. A key part of the future work, requires the investigation of BTFC thin films with higher iron and cobalt dopants. BTFC thin films showed high quality ferroelectric properties with the current level of iron and cobalt dopants, however further investigation is needed, where higher levels of iron and cobalt dopants are employed. The aim of this investigation, will be to determine if the high quality ferroelectric properties in BTFC thin films can be maintained with higher levels of iron and cobalt dopants, and if higher levels of dopants can increase the ferromagnetic remnant magnetisation. This is important, as achieving BTFC thin films with high quality ferroelectric and ferromagnetic behaviours is essential for their application in magnetoelectric applications.

Regarding the investigation of BTFC thin films deposited on silicon substrates with ZnO interface layers. Ferroelectric BTFC thin films where successfully achieved, however the ferroelectric measurements were limited by the need to use a vacuum atmosphere during BTFC annealing, to prevent the oxidation of the silicon substrate. This lead to the generation of oxygen vacancies in the BTFC thin film, which increased the leakage current, and prevented the device from reaching ferroelectric saturation. Further investigations is needed, in which both ambient or oxygen enriched atmospheres are used in order to decrease the concentrations of oxygen vacancies within the thin

film. To achieve this, and prevent oxidisation of the substrate, approaches should include masking the silicon surface during annealing, or etching away SiO_2 post annealing by a buffered hydrofluoric acid solution, whilst covering the thin film with a protective layer.

Chapter 8 : Conclusions

This thesis has demonstrated the successful investigation into the multiferroic properties of BTO thin films by the doping of Fe, Co, La and Nb dopants, and the integration of doped-BTO thin films onto silicon substrates using ZnO interface layers.

The main achievement was the characterisation of BTO thin films with La, Nb, Fe and Co dopants, which produced a thin film with simultaneous ferroelectric and ferromagnetic properties, confirming it as a multiferroic thin film. The ferroelectric properties of the thin films are similar to that of iron and cobalt doped thin films reported elsewhere, indicating good quality ferroelectricity. During ferromagnetic reading, the challenges with eliminating the substrate from there reading was overcome, however the total remnant magnetisation was too small to be accurately measured, requiring further experimentation to increase the total remnant magnetisation to a measurable level.

Other achievements relate to understanding the integration of BTFC thin films on silicon substrates by utilising ZnO interface layers. The ZnO interface layer improved the crystallinity of BTFC thin films, with the ZnO layer increasing the BTFC grain size, and reducing the amount of amorphous phase material present compared to BTFC deposited directly onto silicon with the same sputtering conditions. Annealed and as-deposited ZnO interfaces were both investigated. Both presented non c-axis orientated thin films, with the grain and crystallite size increasing with annealing temperature. Pyrochlore phase $Bi_2Ti_2O_7$ appeared at high temperatures due to the emission of volatile bismuth. This indicates that the ZnO interface layer did not stop the formation of the secondary phase. Elemental mapping demonstrated that the ZnO had limited functions as a diffusion barrier, with zinc atoms diffusing into the BTFC layer. XPS was utilised to study the surface of the sample, and confirmed bismuth, titanium and oxygen binding energies indicative of Aurivillius phase BTO. EDS was used to confirm that all dopants had been successfully inserted into the thin films by rf magnetron sputtering.

The electronic properties of BTFC thin films on silicon with ZnO interface layers were also investigated. The triangular waveform voltage method confirmed that ferroelectric BTFC had been achieved on silicon whilst utilising ZnO interface layers. This investigation was limited by the necessity to anneal the sample in a vacuum atmosphere to prevent the oxidation of the silicon substrate. This resulted in the generation of oxygen vacancies in the thin film, which increased the leakage current and reduced the break down voltage. This low breakdown voltage limited the driving field during the ferroelectric measurement, resulting in an unsaturated ferroelectric loop. The investigation into BTFC on ZnO provides insight into ZnO interface layers being utilised as a more affordable substrate and the feasibility of a BTO/ZnO MFS device.

In summary, a multiferroic $Bi_4Ti_3O_{12}$ based thin film was confirmed by Fe and Co doping. The film possessed good ferroelectric and ferromagnetic properties and provides information that assists in understanding the nature of ferromagnetism in BTO thin films. Additionally, ferroelectric BTFC thin films were confirmed on silicon substrates with ZnO interface layers. The ZnO interface layer improves the crystallinity of BTFC on silicon, opening up future research for more affordable substrates than platinised silicon and the possibility of BTO/ZnO MFS devices. Plans for future work into understanding the ferromagnetic properties of Fe and Co doped thin films have been presented, contributing towards the development of practical magnetoelectric memory devices.

References

1. Yang FL, Chen HY, Huang CC, editors. Outlook for 15nm CMOS research technologies. 2010 10th IEEE International Conference on Solid-State and Integrated Circuit Technology; 2010 1-4 Nov. 2010.
2. Chen J, Bai Y, Nie C, Zhao S. Strong magnetoelectric effect of Bi4Ti3O12/Bi5Ti3FeO15 composite films. J Alloys Compd. 2016;663:480-6.
3. Sundararaj A, Chandrasekaran G, Therese HA, Annamalai K. Room temperature magnetoelectric coupling in BaTi1-xCrxO3 multiferroic thin films. J Appl Phys. 2016;119(2):024107.
4. Chen XQ, Wei C, Xiao J, Xue Y, Zeng XB, Yang FJ, et al. Room temperature multiferroic properties and magnetocapacitance effect of modified ferroelectric Bi4Ti3O12 ceramic. J Phys D Appl Phys. 2013;46(42):425001.
5. Luo SJ, Wang CB, Zhang S, Tu R, Liu SL, Tang XF, et al. Epitaxial Integration of (100) Bi4Ti3O12 with (0001) ZnO through Long-Range Lattice Matching. Applied Physics Express. 2012;5(8):085801.
6. Bedoya-Hincapie CM, Restrepo-Parra E, Olaya-Florez JJ, Alfonso JE, Flores-Ruiz FJ, Espinoza-Beltran FJ. Ferroelectric behavior of bismuth titanate thin films grown via magnetron sputtering. Ceram Int. 2014;40(8):11831-6.
7. Yamazaki S. History and future perspective of nonvolatile memory. Sixteenth IEEE International Symposium on the Applications of Ferroelectrics, . 2007;1&2:1-3.
8. Masuoka F, Asano. M, Iwahashi. H, Komuro. T, Tanaka. S,. A new flash E2PROM cell using triple polysilicon technology. Electron Devices Meeting, 1984 International 1984:464 - 7.
9. Moore GE. Cramming more components onto integrated circuits (Reprinted from Electronics, pg 114-117, April 19, 1965). Proceedings of the Ieee. 1998;86(1):82-5.
10. Ferain I, Colinge CA, Colinge JP. Multigate transistors as the future of classical metal-oxide-semiconductor field-effect transistors. Nature. 2011;479(7373):310-6.
11. W. Arden MB, P. Cogez, M. Graef, B. Huizing, R. Mahnkopf,. More-than-Moore, International Technology Roadmap for Semiconductors,. International Technology Roadmap for Semiconductors. 2010.
12. X-Fab. What is "More than Moore"? 2016. Accesed on: 11/June/2017:[Available from: https://www.xfab.com/about-x-fab/more-than-moore/what-is-more-than-moore/.
13. ITRS. Emerging Research Device Summary 2013. Accesed on: 09/December/2015:[Available from: https://www.semiconductors.org/clientuploads/Research_Technology/ITRS/2013/2013ERD.pdf.
14. Shen JX, Cong JZ, Shang DS, Chai YS, Shen SP, Zhai K, et al. A multilevel nonvolatile magnetoelectric memory. Scientific Reports. 2016;6:34473
15. Radio-Electronics. FRAM Ferroelectric RAM Technology & Operation 2011. Accesed on: 21/August/2017:[Available from: http://www.radio-electronics.com/info/data/semicond/memory/fram-ferroelectric-random-access-memory-technology-operation-theory.php.
16. Fusil S, Garcia V, Barthelemy A, Bibes M. Magnetoelectric Devices for Spintronics. Annu Rev Mater Res. 2014;44:91-116.
17. M. Slaughter EYC, R. Whig, B.N. Engel, J. Janesky, and S. Tehrani. Magnetic Tunnel Junction Materials for Electronic Applications 2016. Accesed on: 21/November/2016:[Available from: http://www.tms.org/pubs/journals/JOM/0006/Slaughter/Slaughter-0006.html.
18. Apalkov D, Khvalkovskiy A, Watts S, Nikitin V, Tang XT, Lottis D, et al. Spin-Transfer Torque Magnetic Random Access Memory (STT-MRAM). Acm J Emerg Tech Com. 2013;9(2):13.
19. Heron JT, Bosse JL, He Q, Gao Y, Trassin M, Ye L, et al. Deterministic switching of ferromagnetism at room temperature using an electric field. Nature. 2014;516(7531):370-3.

20. Wu SM, Cybart SA, Yu P, Rossell MD, Zhang JX, Ramesh R, et al. Reversible electric control of exchange bias in a multiferroic field-effect device. Nat Mater. 2010;9(9):756-61.
21. Wei Y, Gao C, Chen Z, Xi S, Shao W, Zhang P, et al. Four-state memory based on a giant and non-volatile converse magnetoelectric effect in FeAl/PIN-PMN-PT structure. Scientific Reports. 2016;6:30002.
22. Eerenstein W, Mathur ND, Scott JF. Multiferroic and magnetoelectric materials. Nature. 2006;442(7104):759-65.
23. Valasek.J. Piezo-Electric and Allied Phenomena in Rochelle Sal. Journal of Physics review. 1921;17(4):475-81.
24. Matthias B. New Ferroelectric Crystals. Physcis review. 1949;75(11):1771.
25. Pandu R. CrFe2O4 - BiFeO3 Perovskite Multiferroic Nanocomposites – A Review. Material Science Research India. 2014;11(2):128-45.
26. Lous R. Ferroelectric Memory Devices, How to store information of the future 2011. Accesed on: 15/December/2016:[Available from: https://www.rug.nl/research/zernike/education/topmasternanoscience/ns190lous.pdf.
27. Shimada. T, Kitamura. T. Multi-Physics Properties in Ferroelectric Nanowires and Related Structures from First-Principles, Nano wires. Prete P, editor: InTech; 2010.
28. Damjanovic D. Ferroelectric, dielectric and piezoelectric properties of ferroelectric thin films and ceramics. Rep Prog Phys. 1998;61(9):1267-324.
29. Yu J, Zhang LL, Hou XB, Lin Y, Zheng WL. Novel Perovskite-type Ferroelectrics with High Curie Temperature and Piezoresponse (review). 2016 Joint Ieee International Symposium on the Applications of Ferroelectrics, European Conference on Application of Polar Dielectrics, and Piezoelectric Force Microscopy Workshop (Isaf/Ecapd/Pfm). 2016.
30. Shrout TR, Zhang SJ. Lead-free piezoelectric ceramics: Alternatives for PZT? J Electroceram. 2007;19(1):113-26.
31. Johnson RW, Evans JL, Jacobsen P, Thompson JR, Christopher M. The changing automotive environment: high-temperature electronics. IEEE Transactions on Electronics Packaging Manufacturing. 2004;27(3):164-76.
32. What-When-How. Magnetic Phenomena and Their Interpretation—Classical Approach (Magnetic Properties of Materials) Part 1: ENOM, INC. Accesed on: 17/November/2016:[Available from: http://what-when-how.com/electronic-properties-of-materials/magnetic-phenomena-and-their-interpretationclassical-approach-magnetic-properties-of-materials-part-1/.
33. NDT Resource Center. Different magnetic interaction mechanisms 2017. Accesed on: 21/August/2017:[Available from: https://www.nde-ed.org/index_flash.htm.
34. Aberystwyth-University. Collective magnetism: Ferromagnetism et al.; Accesed on: 02/January/2017:[Available from: http://users.aber.ac.uk/ruw/teach/334/ferro.php.
35. Ambati H. Magnetic materials 2015. Accesed on: 28/July/2017:[Available from: https://www.slideshare.net/harshaambati9/magnetic-materials-47590107.
36. Zimmermann AS, Meier D, Fiebig M. Ferroic nature of magnetic toroidal order. Nature Communications. 2014;5:4796.
37. Paul-Scherrer-Institute. Multiferroic Materials 2016. Accesed on: 06/January/2017:[Available from: https://www.psi.ch/lmx-interfaces/multiferroic-thin-films.
38. Kimura T, Goto T, Shintani H, Ishizaka K, Arima T, Tokura Y. Magnetic control of ferroelectric polarization. Nature. 2003;426(6962):55-8.
39. Hur N, Park S, Sharma PA, Ahn JS, Guha S, Cheong SW. Electric polarization reversal and memory in a multiferroic material induced by magnetic fields. Nature. 2004;429(6990):392-5.
40. Bichurin MI, Petrov VM, Petrov RV, Kiliba YV, Bukashev FI, Smirnov AY, et al. Magnetoelectric sensor of magnetic field. Ferroelectrics. 2002;280:365-8.
41. Dong S, Zhai J, Li JF, Viehland D, Priya S. Multimodal system for harvesting magnetic and mechanical energy. Appl Phys Lett. 2008;93(10):103511.

42. Zhang YM, Pan SF. An Electrically-Tunable Microwave Photonic Filter Based on Polarization Modulation. '2014 IEEE Mtt-S International Microwave Symposium (Ims)'2014.
43. Wang DH, Goh WC, Ning M, Ong CK. Effect of Ba doping on magnetic, ferroelectric, and magnetoelectric properties in mutiferroic BiFeO3 at room temperature. Appl Phys Lett. 2006;88(21):212907.
44. Davidson MW, Lofgren GE. Photomicrography in the Geological Sciences. Journal of Geological Education. 1991;39(5):403-18.
45. Cava.J. Perovskite Structure and Derivatives Princeton University2017. Accesed on: 20/April/2014:[Available from: http://www.princeton.edu/~cavalab/tutorials/public/structures/perovskites.html.
46. Xue KH, Fonseca LRC, Miao XS. Ferroelectric fatigue in layered perovskites from self-energy corrected density functional theory. Rsc Adv. 2017;7(35):21856-68.
47. A-Paz De Arauko C, Cuchiaro JD, McMillan LD, Scott MC, Scott JF. Fatigue-free ferroelectric capacitors with platinum electrodes. Nature. 1995;374(6523):627-9.
48. Park BH, Kang BS, Bu SD, Noh TW, Lee J, Jo W. Lanthanum-substituted bismuth titanate for use in non-volatile memories. Nature. 1999;401(6754):682-4.
49. Kim SK, Miyayama M, Yanagida H. Electrical Anisotropy and a Plausible Explanation for Dielectric Anomaly of Bi4Ti3O12 Single-Crystal. Mater Res Bull. 1996;31(1):121-31.
50. Yamaguchi M, Nagamoto T, Omoto O. Preparation of highly c-axis-oriented Bi4Ti3O12 thin films and their crystallographic, dielectric and optical properties. Thin Solid Films. 1997;300(1-2):299-304.
51. Villegas M, Caballero AC, Jardiel T, Arago C, Maudes J, Caro I. Evaluation of Piezoelectric Properties of Bi4Ti3O12Based Ceramics at High Temperature. Ferroelectrics. 2009;393:44-53.
52. Ye W, Tang, L., Lu, C., Li, H. & Zhou, Y. In situ observation of the motion of ferroelectric domain walls in Bi4Ti3O12 single crystals. J Appl Cryst. 2016;49:1645-52.
53. Irie H, Miyayama M, Kudo T. Structure dependence of ferroelectric properties of bismuth layer-structured ferroelectric single crystals. J Appl Phys. 2001;90(8):4089-94.
54. Besland MP, Aissa HDA, Barroy PRJ, Lafane S, Tessier PY, Angleraud B, et al. Comparison of lanthanum substituted bismuth titanate (BLT) thin films deposited by sputtering and pulsed laser deposition. Thin Solid Films. 2006;495(1-2):86-91.
55. Besland MP, Borderon C, Barroy PRJ, Le Tacon S, Richard-Plouet M, Averty D, et al. Improvement of dielectric properties of BLT thin films deposited by magnetron sputtering J Phys Conf Ser. 2008;94:12006.
56. Wu YY, Zhang DM, Yu J, Wang YB. The Effect of Deposition Temperature and Postanneal on the Bi3.63Pr0.3Ti3O12 thin Films Prepared by RF-Magnetron Sputtering Method. J Am Ceram Soc. 2009;92(2):501-5.
57. Yamaguchi M, Nagatomo T. Preparation and properties of Bi4Ti3O12 thin films grown at low substrate temperatures. Thin Solid Films. 1999;348(1-2):294-8.
58. Alfonso JE, Olaya JJ, Bedoya-Hincapie CM, Toudert J, Serna R. Annealing Effect on the Structural and Optical Properties of Sputter-Grown Bismuth Titanium Oxide Thin Films. Materials. 2014;7(5):3427-34.
59. Simoes AZ, Ries A, Stojanovic BD, Biasotto G, Longo E, Varela JA. Electrical properties of lanthanum doped Bi4Ti3O12 thin films annealed in different atmospheres. Ceram Int. 2007;33(8):1535-41.
60. Zhong N, Xiang PH, Zhang YY, Wu X, Tang XD, Yang PX, et al. Polarization fluctuation behavior of lanthanum substituted Bi4Ti3O12 thin films. J Appl Phys. 2015;118(10):104102.
61. Singh SK, Ishiwara H. Ferroelectric properties enhancement in niobium-substituted Bi3.25La0.75Ti3O12 thin films prepared by chemical solution route. Thin Solid Films. 2006;497(1-2):90-5.

62. Uchida H, Okada I, Matsuda H, Iijima T, Watanabe T, Funakubo H. Fabrication of Ion-Cosubstituted Bismuth Titanate Thin Films by Chemical Solution Deposition Method. Integr Ferroelectr. 2003;52(1):41-54.
63. Bao ZH, Yao YY, Zhu JS, Wang Y. Study on ferroelectric and dielectric properties of niobium doped Bi4Ti3O12 ceramics and thin films prepared by PLD method. Mater Lett. 2002;56(5):861-6.
64. Gautam P, Singh SK, Tandon RP. Mechanism for leakage current conduction in manganese doped Bi3.25La0.75Ti3O12 (BLT) ferroelectric thin films. J Alloys Compd. 2014;606(0):132-8.
65. Wang SW, Lu W, Li N, Li ZF, Wang H, Wang M, et al. Insulating properties of rapid thermally processed Bi2Ti2O7 thin films by a chemical solution decomposition technique. Mater Res Bull. 2002;37(10):1691-7.
66. Maiwa H, Iizawa N, Togawa D, Hayashi T, Sakamoto W, Yamada M, et al. Electromechanical properties of Nd-doped Bi4Ti3O12 films: A candidate for lead-free thin-film piezoelectrics. Appl Phys Lett. 2003;82(11):1760-2.
67. Mao XY, Wang W, Chen XB. Electrical and magnetic properties of Bi5FeTi3O15 compound prepared by inserting BiFeO3 into Bi4Ti3O12. Solid State Commun. 2008;147(5-6):186-9.
68. Mao XY, Sun H, Wang W, Lu YL, Chen XB. Effects of Co-substitutes on multiferroic properties of Bi5FeTi3O15 ceramics. Solid State Commun. 2012;152(6):483-7.
69. Mao XY, Wang W, Chen XB, Lu YL. Multiferroic properties of layer-structured Bi5Fe0.5Co0.5Ti3O15 ceramics. Appl Phys Lett. 2009;95(8):082901.
70. Raghavan CM, Kim JW, Choi JY, Kim JW, Kim SS. Investigation of structural, electrical and multiferroic properties of Co-doped Aurivillius Bi6Fe2Ti3O18 thin films. Ceram Int. 2015;41(2):3277-82.
71. Simoes AZ, Ramirez MA, Riccardi CS, Gonzalez AHM, Longo E, Varela JA. Synthesis and electrical characterization of CaBi2Nb2O9 thin films deposited on Pt/Ti/SiO2/Si substrates by polymeric precursor method. Mater Chem Phys. 2006;98(2-3):203-6.
72. Yamaguchi M, Yamamoto A, Masuda Y. Thermal stability of platinum bottom electrode for bismuth titanate thin films. Integr Ferroelectr. 2006;79:235-43.
73. Jo W, Cho SM, Lee HM, Kim DC, Bu JU. Effect of oxygen to argon ratio on growth of Bi4Ti3O12 thin films on Ir and IrO2 prepared by radio-frequency magnetron sputtering. Jpn J Appl Phys 1. 1999;38(5A):2827-30.
74. Jo W. Structural and ferroelectric properties of Bi4Ti3O12 thin films on IrO2 prepared by rf magnetron sputtering. Appl Phys a-Mater. 2001;72(1):81-4.
75. Rokuta E, Hotta Y, Kubota T, Tabata H, Kobayashi H, Kawai T. Effects of an ultrathin silicon oxynitride buffer layer on electrical properties of ferroelectric Bi4Ti3O12 thin films on p-Si(100) surfaces. Appl Phys Lett. 2001;79(3):403-5.
76. Sun CL, Chen SY, Chen SB, Chin A. Effect of annealing temperature on physical and electrical properties of Bi3.25La0.75Ti3O12 thin films on Al2O3-buffered Si. Appl Phys Lett. 2002;80(11):1984-6.
77. Hao LZ, Zhu J, Liu YJ, Wang SL, Zeng HZ, Liao XW, et al. Integration and electrical properties of epitaxial LiNbO3 ferroelectric film on n-type GaN semiconductor. Thin Solid Films. 2012;520(7):3035-8.
78. Posadas A, Yau JB, Ahn CH, Han J, Gariglio S, Johnston K, et al. Epitaxial growth of multiferroic YMnO3 on GaN. Appl Phys Lett. 2005;87(17).
79. Mbenkum BN, Ashkenov N, Schubert M, Lorenz M, Hochmuth H, Michel D, et al. Temperature-dependent dielectric and electro-optic properties of a ZnO-BaTiO3-ZnO heterostructure grown by pulsed-laser deposition. Appl Phys Lett. 2005;86(9):091904.
80. Bhatia D, Roy S, Nawaz S, Meena RS, Palkar VR. Observation of temperature effect on electrical properties of novel Au/Bi0.7Dy0.3FeO3/ZnO/p-Si thin film MIS capacitor for MEMS applications. Microelectron Eng. 2017;168:55-61.

81. Krishnamoorthi SR, Venkatesh KS, Ilangovan R. Structural and Electrical Characteristics of Metal-Ferroelectric Pb-1.1(Zr0.40Ti0.60)O-3-Insulator (ZnO)-Silicon Capacitors for Nonvolatile Applications. Adv Cond Matter Phys. 2013;2013:692364.
82. Technical Ceramics. Hot Pressing 2016. Accesed on: 16/December/2016:[Available from: http://www.dynacer.com/processing/hot-pressing/.
83. Tan YQ, Zhang JL, Wu YQ, Wang CL, Koval V, Shi BG, et al. Unfolding grain size effects in barium titanate ferroelectric ceramics. Scientific Reports. 2015;5:9953.
84. M. Suárez AFn, J.L. Menéndez, R. Torrecillas, H. U. Kessel, J. Hennicke, R. Kirchner and T. Kessel. Sintering Applications: InTech; 2013.
85. Direct Vacuum. Magnetron Sputtering Technology 2017. Accesed on: 21/August/2017:[Available from: http://www.directvacuum.com/sputter.asp.
86. Bosco R, Van Den Beucken J, Leeuwenburgh S, Jansen J. Surface Engineering for Bone Implants: A Trend from Passive to Active Surfaces. Coatings. 2012;2(3):95-119.
87. Pandirengan T, Arumugam M, Durairaj M, Suyambulingam GRT. Development of performance-improved global positioning system (GPS) patch antenna based on sol-gel-synthesized dual-phase (Bi4Ti3O12)(X) - (CaCu3Ti4O12)(1-X) composites. Cryst Res Technol. 2016;51(6):366-79.
88. Raghavan CM, Kim JW, Kim JW, Kim SS. Effects of La- and V-doping on structural, electrical and multiferroic properties of Bi6Fe2Ti3O18 thin films. Ceram Int. 2014;40(7):10649-55.
89. Liu. Weiliang, Wang. Xinqiang, Tian. Dong, Xiao. Chenglong, Wei. Zengjiang, Shouhua. chen. Chemical Reaction and Crystalline Procedure of Bismuth Titanate Nanoparticles Derived by Metalorganic Decomposition Technique Materials Sciences and Applications. 2010;1:91-6.
90. X. B. Liu XAM, C. Q. Huang, J. Liu. Dielectric and Ferroelectric Properties of Er2O3-doped Bi4Ti3O12 Thin Films. Key Eng Mater. 2013;537:118-21.
91. Keeney L, Zhang PFF, Groh C, Pemble ME, Whatmore RW. Piezoresponse force microscopy investigations of Aurivillius phase thin films. J Appl Phys. 2010;108(4):42004.
92. BYJU's. Bragg's Law 2017. Accesed on: 28/July/2017:[Available from: http://byjus.com/physics/braggs-law/.
93. Dutrow BL. X-ray Powder Diffraction (XRD): The Science Education Resource Center at Carleton College; 02-Sep-2016. Accesed on: 29/September/2016:[Available from: http://serc.carleton.edu/research_education/geochemsheets/techniques/XRD.html.
94. University Of Cambridge. The Scanning Electron Microscope (SEM) 2017. Accesed on: 28/July/2017:[Available from: http://www.eng-atoms.msm.cam.ac.uk/RoyalSocDemos/SEM.
95. Nanoscience Instruments. Sample-Electron Interaction: Nanoscience Instruments; 23-jun-2014. Accesed on: 29/September/2016:[Available from: http://www.nanoscience.com/technology/sem-technology/sample-electron-interaction/.
96. SoaresCarvalho F, Jauberteau I, Thomas P, Mercurio JP. Bi4Ti3O12 ferroelectric thin films: Morphology and electrical characteristics. J Phys III. 1997;7(6):1221-6.
97. AMMRF. Characteristic X-rays 2014. Accesed on: 18/March/2017:[Available from: http://www.ammrf.org.au/myscope/analysis/eds/xraygeneration/characteristic/.
98. Stojanovic BD, Paiva-Santos CO, Cilense M, Jovalekic C, Lazarevic ZZ. Structure study of Bi4Ti3O12 produced via mechanochemically assisted synthesis. Mater Res Bull. 2008;43(7):1743-53.
99. Chen Y, Liang DY, Wang QY, Zhu JG. Microstructures, dielectric, and piezoelectric properties of W/Cr co-doped Bi4Ti3O12 ceramics. J Appl Phys. 2014;116(7):074108.
100. Bernard H, Lisinska-Czekaj A, Dzik J, Osinska K, Czekaj D. Fabrication, Structural and AC Impedance Studies of Layer-Structured Bi4Ti3O12 Ceramics. Arch Metall Mater. 2011;56(4):1137-48.
101. Warwick University. Transmission Electron Microscopy (TEM) 2017. Accesed on: 13/March/2017:[Available from: https://www2.warwick.ac.uk/fac/sci/physics/current/postgraduate/regs/mpags/ex5/techniques/structural/tem/.
102. Walther-Meißner-Institute for Low Temperature Research. SQUID Magnetometry 2017. Accesed on: 22/August/2017:[Available from: https://www.wmi.badw.de/methods/squid.htm.

103. Efendiev SM, Kulieva, T. Z., Lomonov, V. A., Chiragov, M. I., Grandolfo, M. and Vecchia, P. Crystal Structure of Bismuth Titanium Oxide Bi12TiO20. phys stat sol. 1982;74:17-21.
104. Microsence. Vibrating Sample Magnetometer (VSM): Microsence; 2013. Accesed on: 05/January/2017:[Available from: http://www.microsense.net/products-vsm.htm.
105. limited' C. Vibrating Sample Magnetometer (VSM) 2016. Accesed on: 05/January/2017:[Available from: http://www.cryogenic.co.uk/products/vibrating-sample-magnetometer-vsm.
106. Quantum Design. Magnetic Property Measurement System 2012. Accesed on: 06/January/2017:[Available from: http://www.qdusa.com/products/mpms3.html.
107. IFW. X-Ray Photoelectron Spectroscopy (XPS) 2017. Accesed on: 28/July/2017:[Available from: https://www.ifw-dresden.de/institutes/ikm/research-teams-and-topics/micro-and-nanostructures/available-methods/xps/.
108. Yan HX, Inam. F, Viola. G, Ning. H, Zhang. H, Jiang. Q, et al. The contribution of electrical conductivity, Dielectric permitivity and domain switching in ferroelectrci hysterisis loops.

. Journal of Advanced Dielectrics. 2011;1(1):107-18.
109. Yang F, Guo YC, Zong ZH, Hao XH, Shi YW, Tang MH. Improving the Electrical Properties of Zr-Doped Bi3.15Nd0.85Ti3O12 Thin Films by Engineering Polarization Rotation. J Electron Mater. 2016;45(7):3540-5.
110. Sruthi S, Adarsh A, Veronica A, Saideep M, Dutta S. Thickness dependent mechanical and ferroelectric properties of Bi4Ti3O12 film. J Mater Sci-Mater El. 2016;27(4):4062-7.
111. Ding Y, Liu JS, Qin HX, Zhu JS, Wang YN. Why lanthanum-substituted bismuth titanate becomes fatigue free in a ferroelectric capacitor with platinum electrodes. Appl Phys Lett. 2001;78(26):4175-7.
112. Kao MC, Chen HZ, Young SL. The microstructure and ferroelectric properties of Sm and Ta-doped bismuth titanate ferroelectric thin films. Thin Solid Films. 2013;529:143-6.
113. Soe KKK, Khaing MA, Thein PY, Win TT, Maung YM. Microstructural and Electrical Properties of Mn Doped Bi4Ti3O12 Thin Film Devices. International Journal of Scientific & Engineering Research. 2015;6(3):406.
114. Sun H, Lu XM, Su J, Xu TT, Ju CC, Huang FZ, et al. Multiferroic behaviour and the magneto-dielectric effect in Bi5FeTi3O15 thin films. J Phys D Appl Phys. 2012;45(38):385001.
115. Atsuki T, Soyama N, Yonezawa T, Ogi K. Preparation of Bi-Based Ferroelectric Thin-Films by Sol-Gel Method. Jpn J Appl Phys 1. 1995;34(9b):5096-9.
116. Kijima T, Matsunaga H. Preparation of Bi4Ti3O12 thin film on Si(100) substrate using Bi2SiO5 buffer layer and its electric characterization. Jpn J Appl Phys 1. 1998;37(9b):5171-3.
117. Han JP, Ma TP. SrBi2Ta2O9 memory capacitor on Si with a silicon nitride buffer. Appl Phys Lett. 1998;72(10):1185-6.
118. Setter N, Damjanovic D, Eng L, Fox G, Gevorgian S, Hong S, et al. Ferroelectric thin films: Review of materials, properties, and applications. J Appl Phys. 2006;100(5):051606.
119. Singh B, Khan ZA, Khan I, Ghosha S. Highly conducting zinc oxide thin films achieved without postgrowth annealing. Appl Phys Lett. 2010;97(24):241903.
120. Sun JC, Yang TP, Du GT, Liang HW, Bian JM, Hu LZ. Influence of annealing atmosphere on ZnO thin films grown by MOCVD. Appl Surf Sci. 2006;253(4):2066-70.
121. Kidchob T, Malfatti L, Marongiu D, Enzo S, Innocenzi P. Sol-Gel Processing of Bi2Ti2O7 and Bi2Ti4O11 Films with Photocatalytic Activity. J Am Ceram Soc. 2010;93(9):2897-902.
122. Chen Y, Xie SX, Liang DY, Peng ZH, Wang QY, Zhu JG, et al. Influence of sintering temperatures on microstructures and electrical properties of Bi4Ti2.95W0.05O12.05+0.2 wt%Cr2O3 ceramics. Mater Res Bull. 2015;70:272-8.
123. McInnes A, Sagu JS, Wijayantha KGU. Fabrication and photoelectrochemical studies of Bi2Ti2O7 pyrochlore thin films by aerosol assisted chemical vapour deposition. Mater Lett. 2014;137:214-7.
124. Oropeza FE, Villar-Garcia IJ, Palgrave RG, Payne DJ. A solution chemistry approach to epitaxial growth and stabilisation of Bi2Ti2O7 films. J Mater Chem A. 2014;2(43):18241-5.

125. Zak AK, Razali R, Majid WHA, Darroudi M. Synthesis and characterization of a narrow size distribution of zinc oxide nanoparticles. Int J Nanomed. 2011;6:1399-403.
126. Wang XS, Zhai JW, Zhang LY, Yao X. Structural and optical characterization of Bi4Ti3O12 thin films prepared by metallorganic solution deposition technique. Infrared Phys Techn. 1999;40(1):55-60.
127. Takashige M, Hamazaki S, Takhashi Y, Shimizau F, Yamaguchi T, Jang MS, et al. Observation of crystallization process from amorphous Bi4Ti3O12 prepared by rapid quenching method. Jpn J Appl Phys 1. 2000;39(9b):5716-8.
128. Zhou D, Gu HS, Hu YM, Qian ZL, Hu ZL, Yang K, et al. Raman scattering, electronic, and ferroelectric properties of Nd modified Bi4Ti3O12 nanotube arrays. J Appl Phys. 2010;107(9):094105.
129. Suyal G, Bharadwaja SSN, Cantoni M, Damjanovic D, Setter N. Properties of chemical solution deposited polycrystalline neodymium-modified Bi4Ti3O12. J Electroceram. 2002;9(3):187-92.
130. Qian K, Jiang ZF, Shi H, Wei W, Zhu CZ, Xie JM. Constructing mesoporous Bi4Ti3O12 with enhanced visible light photocatalytic activity. Mater Lett. 2016;183:303-6.
131. Wang F, Wang JB, Zhong XL, Li B, Zhang Y, Lu CJ, et al. Enhanced piezoelectric response in single-crystalline Bi4Ti3O12 nanoplates. Epl-Europhys Lett. 2013;103(3):37002.
132. Noguchi Y, Soga M, Takahashi M, Miyayama M. Oxygen stability and leakage current mechanism in ferroelectric La-substituted Bi4Ti3O12 single crystals. Japanese Journal of Applied Physics Part 1-Regular Papers Brief Communications & Review Papers. 2005;44(9b):6998-7002.
133. Park BH, Hyun SJ, Bu SD, Noh TW, Lee J, Kim HD, et al. Differences in nature of defects between SrBi2Ta2O9 and Bi4Ti3O12. Appl Phys Lett. 1999;74(13):1907-9.
134. Sunding MF, Hadidi K, Diplas S, Lovvik OM, Norby TE, Gunnaes AE. XPS characterisation of in situ treated lanthanum oxide and hydroxide using tailored charge referencing and peak fitting procedures. J Electron Spectrosc Relat Phenom. 2011;184(7):399-409.
135. Chu CM, Wu JJ, Yung SW, Chin TS, Zhang T, Wu FB. Optical and structural properties of Sr-Nb-phosphate glasses. J Non-Cryst Solids. 2011;357(3):939-45.
136. Grosvenor AP, Kobe BA, Biesinger MC, McIntyre NS. Investigation of multiplet splitting of Fe 2p XPS spectra and bonding in iron compounds. Surf Interface Anal. 2004;36(12):1564-74.
137. Shi HF, Tan HQ, Zhu WB, Sun ZC, Ma YJ, Wang EB. Electrospun Cr-doped Bi4Ti3O12/Bi2Ti2O7 heterostructure fibers with enhanced visible-light photocatalytic properties. J Mater Chem A. 2015;3(12):6586-91.
138. Simoes AZ, Riccardi CS, Cavalcante LS, Gonzalez AHM, Longo E, Varela JA. Size effects of polycrystalline lanthanum modified Bi4Ti3O12 thin films. Mater Res Bull. 2008;43(1):158-67.
139. Pookmanee P, Boonphayak P, Phanichphant S. Chemical synthesis of bismuth titanate microparticles. Ceram Int. 2004;30(7):1917-9.
140. Gonzalez JA, Carreras AC, Ruiz MDC. Phase transformations in clays and kaolins produced by thermal treatment in chlorine and air atmospheres. Lat Am Appl Res. 2007;37(2):133-9.
141. Zheng LR, Lin CL, Xu HP, Zou SC. Leakage behavior and distortion of the hysteresis loop in ferroelectric thin films. Sci China Ser E. 1997;40(2):126-34.
142. Vehkamaki M, Hatanpaa T, Kemell M, Ritala M, Leskelaa M. Atomic layer deposition of ferroelectric bismuth titanate Bi4Ti3O12 thin films. Chem Mater. 2006;18(16):3883-8.
143. Kojima T, Sakai T, Watanabe T, Funakubo H, Saito K, Osada M. Large remanent polarization of (Bi,Nd)(4)Ti3O12 epitaxial thin films grown by metalorganic chemical vapor deposition. Appl Phys Lett. 2002;80(15):2746-8.
144. Qi HY, Qi YJ, Xiao M. Leakage mechanisms in rare-earth (La, Nd) doped Bi4Ti3O12 ferroelectric ceramics. J Mater Sci-Mater El. 2014;25(3):1325-30.
145. Warren WL, Dimos D, Waser RM. Degradation mechanisms in ferroelectric and high-permittivity perovskites. MRS Bull. 1996;21(7):40-5.
146. Sun H, Zhu J, Fang H, Chen XB. Large remnant polarization and excellent fatigue property of vanadium-doped SrBi4Ti4O15 thin films. J Appl Phys. 2006;100(7):074102.

147. Simoes AZ, Gonzalez AHM, Riccardi CS, Souza EC, Moura F, Zaghete MA, et al. Ferroelectric and dielectric properties of lanthanum-modified bismuth titanate thin films obtained by the polymeric precursor method. J Electroceram. 2004;13(1):65-70.
148. S. Duenas HC, H. Garcia, and L. Bailon. Electrical Characterization of High-K Dielectric Gates for Microelectronic Devices: INTECH Open Access Publisher; 2013.
149. Yang WL, Chen CY, Mao XY, Chen XB. The doping effects of BiFe1-xCoxO3 (x=0.0-0.8) in layered perovskite Bi4Ti3O12 ceramics. Chinese Phys B. 2012;21(4):047502.
150. Esat F, Comyn TP, Bell AJ. Microstructure development of BiFeO3-PbTiO3 films deposited by pulsed laser deposition on platinum substrates. Acta Mater. 2014;66:44-53.
151. Krasucki J. Advantages of Platinum as a "Barrier" Metal on Thin Film Hybrid Microelectronics Substrates 2016. Accesed on: 09/Febuary/2017:[Available from: http://www.highfrequencyelectronics.com/index.php?option=com_content&view=article&id=1513:advantages-of-platinum-as-a-barrier-metal-on-thin-film-hybrid-microelectronics-substrates&catid=142:2016-09-september-articles&Itemid=189.
152. Sreenivas K, Reaney I, Maeder T, Setter N, Jagadish C, Elliman RG. Investigation of Pt/Ti Bilayer Metallization on Silicon for Ferroelectric Thin-Film Integration. J Appl Phys. 1994;75(1):232-9.
153. Irie H, Saito H, Ohkoshi S, Hashimoto K. Enhanced ferroelectric properties of nitrogen-doped Bi4Ti3O12 thin films. Adv Mater. 2005;17(4):491-4.
154. Simoes AZ, Riccardi CS. Dielectric Spectroscopy Analyses of SrBi4Ti4O15 Films Obtained from Soft Chemical Solution. Adv Mater Sci Eng. 2009;2009:928545.
155. Pintilie L, Lisca M, Alexe M. Polarization reversal and capacitance-voltage characteristic of epitaxial Pb(Zr,Ti)O-3 layers. Appl Phys Lett. 2005;86(19):192902
156. Zhang ST, Zhang XJ, Cheng HW, Chen YF, Liu ZG, Ming NB, et al. Enhanced electrical properties of c-axis epitaxial Nd-substituted Bi4Ti3O12 thin films. Appl Phys Lett. 2003;83(21):4378-80.
157. Jo H, Kim S, Do D. Fabrication and properties of xBiFeO(3)-(1-x)Bi4Ti3O12 system by sol-gel process. J Sol-Gel Sci Technol. 2009;49(3):336-40.
158. Rumpf K, Granitzer P. Diamagnetic Behavior of Porous Silicon. In: Canham L, editor. Handbook of Porous Silicon. Cham: Springer International Publishing; 2014. p. 281-5.
159. Liu Z, Yang J, Tang XW, Yin LH, Zhu XB, Dai JM, et al. Multiferroic properties of Aurivillius phase Bi6Fe2-xCoxTi3O18 thin films prepared by a chemical solution deposition route. Appl Phys Lett. 2012;101(12):122402.